



SAPIENZA
UNIVERSITÀ DI ROMA

N°d'ordre NNT : 2017LYSEI118

THESE de DOCTORAT DE L'UNIVERSITE DE LYON

opérée au sein de

Institut National des Sciences Appliquées de Lyon

En cotutelle internationale avec

La Sapienza - Università di Roma

Ecole Doctorale N° 162

Mécanique, Energétique, Génie Civil, Acoustique (MEGA)

Spécialité: Génie Mécanique

Soutenue publiquement le 18/12/2017, par :

Giovanna Lacerra

**Friction-Induced Vibrations as a result of system
response and contact dynamics: a newer friction law for
broadband contact excitation**

Devant le jury composé de :

Fregolent, Annalisa	Professeur	La Sapienza – Università di Roma	Présidente
Hoffmann, Norbert	Professeur	Hamburg University of Technology	Rapporteur
Koc, Ilker Murat	Professeur	Istanbul Technical University	Rapporteur
Baillet, Laurent	Professeur	Université Grenoble Alpes-IsTerre	Examineur
Meziane, Anissa	Maître de Conférences	Université Bordeaux 1	Examinatrice
Fregolent, Annalisa	Professeur	La Sapienza – Università di Roma	Examinatrice
Massi, Francesco	Professeur	La Sapienza – Università di Roma	Directeur de thèse
Chatelet, Eric	Maître de Conférences	Insa de Lyon	Co-directeur de thèse
Saulot, Aurélien	Maître de Conférences, HdR	Insa de Lyon	Directeur de thèse

Département FEDORA – INSA Lyon - Ecoles Doctorales – Quinquennal 2016-2020

SIGLE	ECOLE DOCTORALE	NOM ET COORDONNEES DU RESPONSABLE
CHIMIE	<p>CHIMIE DE LYON http://www.edchimie-lyon.fr</p> <p>Sec : Renée EL MELHEM Bat Blaise Pascal 3^e étage secretariat@edchimie-lyon.fr Insa : R. GOURDON</p>	<p>M. Stéphane DANIELE Institut de Recherches sur la Catalyse et l'Environnement de Lyon IRCELYON-UMR 5256 Équipe CDFA 2 avenue Albert Einstein 69626 Villeurbanne cedex directeur@edchimie-lyon.fr</p>
E.E.A.	<p>ELECTRONIQUE, ELECTROTECHNIQUE, AUTOMATIQUE http://edeea.ec-lyon.fr</p> <p>Sec : M.C. HAVGODOUKIAN Ecole-Doctorale.eea@ec-lyon.fr</p>	<p>M. Gérard SCORLETTI Ecole Centrale de Lyon 36 avenue Guy de Collongue 69134 ECULLY Tél : 04.72.18 60.97 Fax : 04 78 43 37 17 Gerard.scorletti@ec-lyon.fr</p>
E2M2	<p>EVOLUTION, ECOSYSTEME, MICROBIOLOGIE, MODELISATION http://e2m2.universite-lyon.fr</p> <p>Sec : Sylvie ROBERJOT Bât Atrium - UCB Lyon 1 04.72.44.83.62 Insa : H. CHARLES secretariat.e2m2@univ-lyon1.fr</p>	<p>M. Fabrice CORDEY CNRS UMR 5276 Lab. de géologie de Lyon Université Claude Bernard Lyon 1 Bât Géode 2 rue Raphaël Dubois 69622 VILLEURBANNE Cédex Tél : 06.07.53.89.13 cordey@univ-lyon1.fr</p>
EDISS	<p>INTERDISCIPLINAIRE SCIENCES- SANTE http://www.ediss-lyon.fr</p> <p>Sec : Sylvie ROBERJOT Bât Atrium - UCB Lyon 1 04.72.44.83.62 Insa : M. LAGARDE secretariat.ediss@univ-lyon1.fr</p>	<p>Mme Emmanuelle CANET-SOULAS INSERM U1060, CarMeN lab, Univ. Lyon 1 Bâtiment IMBL 11 avenue Jean Capelle INSA de Lyon 696621 Villeurbanne Tél : 04.72.68.49.09 Fax : 04 72 68 49 16 Emmanuelle.canet@univ-lyon1.fr</p>
INFOMATHS	<p>INFORMATIQUE ET MATHEMATIQUES http://edinfomaths.universite-lyon.fr</p> <p>Sec : Renée EL MELHEM Bat Blaise Pascal, 3^e étage Tél : 04.72. 43. 80. 46 Fax : 04.72.43.16.87 infomaths@univ-lyon1.fr</p>	<p>M. Luca ZAMBONI Bâtiment Braconnier 43 Boulevard du 11 novembre 1918 69622 VILLEURBANNE Cedex Tél : 04 26 23 45 52 zamboni@maths.univ-lyon1.fr</p>
Matériaux	<p>MATERIAUX DE LYON http://ed34.universite-lyon.fr</p> <p>Sec : Marion COMBE Tél:04-72-43-71-70 -Fax : 87.12 Bat. Direction ed.materiaux@insa-lyon.fr</p>	<p>M. Jean-Yves BUFFIERE INSA de Lyon MATEIS Bâtiment Saint Exupéry 7 avenue Jean Capelle 69621 VILLEURBANNE Cedex Tél : 04.72.43 71.70 Fax 04 72 43 85 28 Ed.materiaux@insa-lyon.fr</p>
MEGA	<p>MECANIQUE, ENERGETIQUE, GENIE CIVIL, ACOUSTIQUE http://edmega.universite-lyon.fr/</p> <p>Sec : Marion COMBE Tél:04-72-43-71-70 -Fax : 87.12 Bat. Direction mega@insa-lyon.fr</p>	<p>M. Philippe BOISSE INSA de Lyon Laboratoire LAMCOS Bâtiment Jacquard 25 bis avenue Jean Capelle 69621 VILLEURBANNE Cedex Tél : 04.72 .43.71.70 Fax : 04 72 43 72 37 Philippe.boisse@insa-lyon.fr</p>
ScSo	<p>ScSo* http://ed483.univ-lyon2.fr/</p> <p>Sec : Viviane POLSINELLI Brigitte DUBOIS Insa : J.Y. TOUSSAINT Tél : 04 78 69 72 76 viviane.polsinelli@univ-lyon2.fr</p>	<p>M. Christian MONTES Université Lyon 2 86 rue Pasteur 69365 LYON Cedex 07 Christian.montes@univ-lyon2.fr</p>

*ScSo : Histoire, Géographie, Aménagement, Urbanisme, Archéologie, Science politique, Sociologie, Anthropologie

Acknowledgements

This thesis has been developed in the framework of the collaboration between the INSA of Lyon and La Sapienza-University of Rome; my first thanks goes then to the institutions which have supported this research and made it possible: the doctoral school MEGA (Mécanique, Energetique, Génie Civil, Acoustique) of the INSA of Lyon and the doctoral school of Theoretical and Applied Mechanics of the University of Rome "La Sapienza".

I would like to continue by thanking my Italian and French supervisors and co-supervisors of thesis: Professors Francesco Massi, Eric Chatelet and Aurélien Saulot for their professional guidance during the development of this research work. A special thanks to Francesco Massi for his constant help and to Eric Chatelet, who welcomed me in the French laboratories, guided and encouraged me during these years.

I would like to express my gratitude to the Professors Laurent Baillet, Mariano Di Bartolomeo, Antonio Culla and Dr Silvia Milana for their collaboration and contribution to the research work.

Sincere thanks go also to the reviewers, Professor Norbert Hoffmann and Professor Ilker Murat Koc for their comments, suggestions and questions that allowed for improving this work.

I would like to finish extending my greeting to all friends, colleagues, professors, people that I had the opportunity and pleasure to meet during these years, at the LaMCoS as well as at the DIMA. Among them, Clément Jarroux, Clément Grenat, Guillaume, Aroua, Sophie, Ilyes, Wenfeng, Li-Han, Marc-Andrè, Sayed, Maria, Lina, Marine, Dario, Leandro, Elena, Ilaria, Gianluca, David.

Special thanks go to my family in French: Cécile, Mika, Josè, Jacopo, Davide, Francesca, Gabriele, with them I felt like home in a foreign country.

Concluding, a last but certainly not least thanks to my family: Titta, Caterina, Marco, Manuel, Gianni, Fiorenzo and the giant Calabrian family, without them I wouldn't be able of doing a single step during these years, they always support me and they never gave up in front of my continuous complaining. I dedicate this work to them.

Cotutele agreements

ACCORD DE COOPERATION POUR LA MISE EN ŒUVRE D'UNE COTUTELLE DE THESE

L'Université de Rome "La Sapienza" ayant son siège à Rome (Italie), Piazzale Aldo Moro 5, représentée par son Recteur Professeur Luigi FRATI agissant en-qualité et en vertu des pouvoirs qui lui sont conférés d'une part

ET

L'INSA de LYON, représenté par Monsieur Eric MAURINCOMME, Directeur de l'établissement, agissant en-qualités et en vertu des pouvoirs qui lui sont conférés, d'autre part

Pour la partie italienne :

- Vue la Loi n. 210 du 3 juillet 1998 art. 4 – doctorat de recherche ;
- Vu le D.M. 224/99 relatif aux normes en matière de doctorat de recherche ;
- Vu le D.M. 509/99 relatif aux normes en matière d'autonomie didactique des Universités ;
- Vu le Règlement de l'Université en matière de doctorat de recherche ;
- Vue la délibération du Sénat Académique du 2 octobre 2003 ;

ET

Vu pour la part française :

- L'arrêté du 6 janvier 2005 relatif à la procédure de cotutelle internationale de thèse (France);
- L'arrêté du 7 août 2006 relatif aux études doctorales (France);
- La convention cadre franco-italienne entre la Conférence des Présidents d'Université (CPU) et la Conferenza dei Rettori delle Università Italiane (CRUI) sur la reconnaissance des diplômes et validation des titres universitaires signée en date 18 janvier 1996;
- La convention cadre franco-italienne entre la Conférence des Présidents d'Université (CPU) e la Conferenza dei Rettori delle Università Italiane (CRUI) sur la co-tutelle de thèse signée le 13 février 1998;

désireux (désireuses) de contribuer à l'instauration et/ou au développement de la coopération scientifique entre équipes de recherche italiennes et étrangères en favorisant la mobilité des doctorants

sont convenu(e)s des dispositions suivantes

Titre I – Modalités administratives

Art. 1 – L'Université de Rome "La Sapienza" et L'INSA de Lyon désignées ci-après "les établissements", décident dans le respect des lois et des règlements en vigueur dans chacun des pays et/ou établissements, d'organiser conjointement une cotutelle de thèse au bénéfice de l'étudiante désigné ci-après:

Prénom et nom : Giovanna LACERRA

spécialité : Ingénieur Mécanique – Doctorat en Meccanica Teorica ed Applicata

sujet de thèse : **Analyse énergétique et phénoménologique des vibrations induites par contact frottant: transfert d'énergie entre les champs acoustiques par les non-linéarités du frottement**

Les systèmes mécaniques ayant des contacts glissants sont soumises à des vibrations provenant de l'interface de contact et se propageant dans les solides. Bien qu'une partie de l'énergie est dissipée au niveau du contact, une partie non négligeable de l'énergie est restituée au système sous la forme d'ondes à l'interface de contact et dans la masse, donnant origine aux " vibrations induites par frottement".

L'objectif de cette thèse est de combiner la caractérisation locale tribologique du contact et la caractérisation dynamique non linéaire du système. L'objectif est d'avoir une approche plus complémentaire à la compréhension des vibrations induites par frottement, représentant à la fois le comportement de contact local et la réponse dynamique du système. Les flux d'énergie entre la surface et le volume (et par conséquent le système), et vice versa, seront ainsi chiffré à caractériser les vibrations de friction induite par un point de vue énergétique.

On peut citer plusieurs applications, dans différents domaines: amortissement du contact (dissipation d'énergie) étudié en dynamique des structures non-linéaires (blade dampers, ...); transfert d'énergie entre les champs acoustiques par les non-linéarités de frottement (surveillance passive de santé structurale, récupération d'énergie, ...); stick-slip et instabilités modales du contact (tremblements de terre, crissement des freins, grincements de l'endoprothèse de la hanche, vibrations d'usinage, ...); l'usure due aux vibrations (usure de contact, faux Brinelling, ...).

D'un côté, les campagnes expérimentales dédiées seront adressées à caractériser les vibrations induites par frottement, dans un contexte général, en fonction des paramètres de surface et le système, afin de comprendre les facteurs clés et à définir les lois de contact appropriées à mettre en œuvre dans les codes numériques; contributions perturbatives à le frottement seront en mesure de reproduire l'excitation de contact de frottement mesuré expérimentalement, avec des efforts numériques abordables. L'originalité de l'approche proposée est la prise en compte du couplage de la réponse du système et l'excitation au contact grâce à la conception d'un banc d'essai qui ne cherche pas à les dissocier; la volonté de simplifier la dynamique du système permet de corrélérer les résultats obtenus.

De l'autre côté une analyse expérimentale sera développé afin de quantifier les transferts d'énergie entre les champs acoustiques, obtenue grâce à l'excitation à large bande provenant du contact de frottement, en fonction de paramètres comme les spectres d'excitation, le charge de contact, la rugosité de surface, etc.

Une analyse numérique avec le modèle à paramètres concentrés et un modèle aux éléments finis sera réalisée en parallèle aux tests expérimentaux pour la reproduction des phénomènes physiques et des enquêtes sur le comportement local du contact. L'analyse numérique a le double objectif de permettre la compréhension du comportement locale de contact (impossible d'enquêter expérimentalement) et définir des algorithmes de contact innovantes et des lois de frottement capables de reproduire les vibrations induites par frottement avec des modèles éléments finis classiques sans raffinements du contact. Ce dernier objectif permettra de rendre compte des phénomènes étudiés sans introduire de temps de calcul inabordables.

Les principes et les modalités administratives et pédagogiques de cette cotutelle sont définis par le présent accord.

Art. 2 - La durée prévue pour la préparation de la thèse en cotutelle est de 3 ans, à partir de l'année scolaire 2014/2015

Art. 3 - La préparation de la thèse s'effectue par périodes alternées, à peu près équivalentes, dans chacun des deux établissements partenaires. La durée de ces périodes sera déterminée de commun accord par les deux directeurs de thèse.

Art. 4 – L'étudiante Giovanna LACERRA est tenue à s'inscrire régulièrement dans les deux établissements. L'étudiante paiera les droits d'inscriptions à l'INSA de Lyon et en sera dispensée à l'Università La Sapienza di Roma, auprès de laquelle l'étudiante paiera annuellement uniquement les charges de secrétariat.

Art. 5 – Pour les périodes d'études effectuées en France et pour la soutenance, la doctorante bénéficie de l'ensemble des dispositions de l'arrêté du 7 août 2006 susvisé, et de la charte des thèses de l'INSA de Lyon.

Art.6 – Lors de son inscription, la doctorante devra fournir les justificatifs relatifs à ses ressources, à sa couverture sociale ainsi qu'à son assurance relative aux accidents du travail, dans chacun des pays.

Titre II – Modalités pédagogiques

Art. 1 – Le travail de thèse de l'étudiante sera réalisé sous la supervision commune de deux directeurs de thèse :

- Francesco MASSI (Professeur au Dipartimento di Ingegneria Meccanica e Aerospaziale), directeur de thèse à l'Université "La Sapienza" ;
- Aurélien SAULOT (Maitre de Conférences HDR au Laboratoire de Mécanique des Contacts et des Structures), directeur de thèse à l' INSA de Lyon ;

qui s'engagent à exercer pleinement la fonction de tuteurs de la candidate ainsi qu'à formuler chacun un avis écrit sur la thèse de Doctorat.

L'avis favorable des deux Directeurs de Thèse est une condition nécessaire à l'admission à l'examen final.

Art. 2- La thèse donnera lieu à une soutenance unique, reconnue par les deux établissements concernés. La soutenance aura lieu à l'INSA de Lyon. Le jury de soutenance est composé sur la base d'une proportion équilibrée de membres de chaque établissement désignés conjointement par les établissements contractants et comprend, en outre, des personnalités extérieures à ces établissements.

Il comprendra au moins quatre membres et au maximum huit membres, dont, sauf dérogation, les deux directeurs de thèse.

Art. 3-La thèse sera rédigée et discutée en Anglais. Elle comportera un résumé substantiel rédigé en français et en italien.

Art. 4 – En cas de rapport favorable du Jury, chacun des deux établissements s'engage à conférer le titre de docteur de recherche pour la même thèse.

L'Université de Rome "La Sapienza" s'engage à conférer le grade de docteur de recherche en Meccanica Teorica e Applicata.

L'INSA de Lyon s'engage à conférer le grade de docteur de recherche en Mécanique.

Art. 5-Lorsque la doctorante doit valider des formations complémentaires (scientifiques ou visant à son insertion professionnelle), les établissements (l'Ecole Doctorale MEGA pour l'INSA) préciseront les modalités de reconnaissance mutuelle de ces formations, en accord avec les directeurs de thèse et la doctorante.

Titre III – Conclusions

Art. 1 – L'étudiante est tenue de respecter les règlements et les usages de l'établissement d'accueil.

Art. 2 – Par l'intermédiaire de leurs directeurs de thèses respectifs, les établissements signataires s'engagent à se communiquer toutes les informations et la documentation utiles à l'organisation de la cotutelle de thèse faisant l'objet du présent accord.

Art. 3 – Les modalités de présentation, de dépôt et de reproduction de la thèse seront établies dans chaque pays dans le respect de la réglementation en vigueur.

La protection du sujet de thèse, ainsi que la publication, l'exploitation et la protection des résultats issus des travaux de recherche du doctorant dans les deux établissements signataires seront assujetties à la réglementation en vigueur et assurées conformément aux procédures spécifiques à chacun des pays impliqués dans la cotutelle.

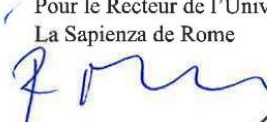
Sur demande, les dispositions concernant la protection des droits de propriété intellectuelle pourront faire l'objet de protocoles ou de documents spécifiques.

Art. 4 – Le présent accord entre en vigueur à partir de la date de signature du représentant légal de chaque établissement signataire et le reste jusqu'à la fin de l'année universitaire au cours de laquelle la thèse ou les travaux seront soutenus. Dans le cas où l'étudiante ne serait pas inscrite dans l'un et/ou l'autre des établissements signataires, ou bien renoncerait par écrit à poursuivre, ou bien n'est pas autorisée à poursuivre la préparation de sa thèse en vertu de la décision de l'un au moins des deux directeurs de thèse, les deux établissements signataires mettront fin conjointement et sans délai, aux dispositions du présent accord.

Art. 5 – Le présent accord est rédigé en quatre exemplaires originaux, dont deux en italien et deux en française, faisant également foi.

Roma, li 11 NOV. 2014

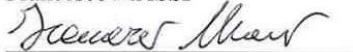
Pour le Recteur de l'Université
La Sapienza de Rome



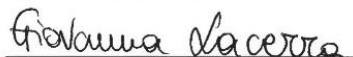

Il Coordinatore del Dottorato di Ricerca
Carlo Massimo CASCIOLA



Il Co-direttore di tesi
Francesco MASSI



La Doctorante
Giovanna LACERRA

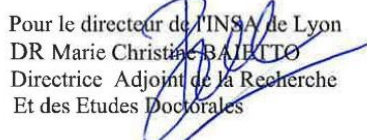




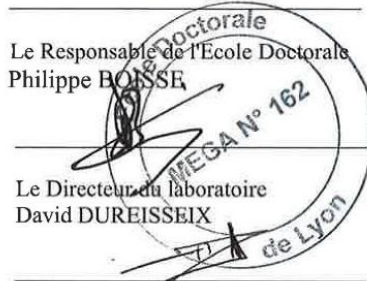
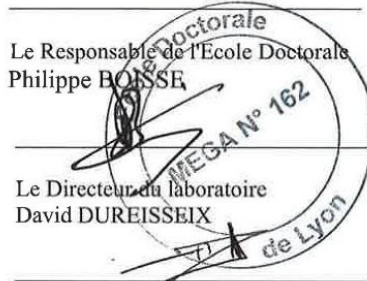


Villeurbanne, li 15 OCT. 2014

Pour le directeur de l'INSA de Lyon
DR Marie Christine BAUTTO
Directrice Adjointe de la Recherche
Et des Etudes Doctorales



Le Responsable de l'Ecole Doctorale
Philippe BOISSE

Le Directeur du laboratoire
David DUREISSEIX



Co-directeur (s) de thèse
Aurélien SAULOT



CONVENZIONE PER UNA CO-TUTELA DI TESI DI DOTTORATO DI RICERCA

L'Università degli Studi di Roma "La Sapienza" con sede in Roma (Italia), Piazzale Aldo Moro, 5 rappresentata dal Rettore Prof. Luigi FRATI, che opera in virtù dei poteri che gli sono conferiti, da una parte

e

L'INSA di Lione rappresentata dal Direttore Eric MAURINCOMME, direttore dello stabilimento, che opera in virtù dei poteri che gli sono conferiti, dall'altra parte

Per la parte italiana:

- VISTA la Legge 210 del 3 luglio 1998 art. 4 – dottorato di ricerca;
- VISTO il D.M. 224/99 recante norme in materia di dottorato di ricerca
- VISTO il D.M. 509/99 recante norme concernenti l'autonomia didattica degli Atenei;
- VISTO il Regolamento di Ateneo in materia di dottorato di ricerca;
- VISTA la delibera del Senato Accademico del 2 ottobre 2003;

e

Visti, per la parte francese,

- La delibera del 6 gennaio 2005 relativo alla procedura internazionale per la cotutela di tesi (Francia);
- La delibera del 7 agosto 2006 relativo al dottorato (Francia);
- La convenzione franco-italiana tra la Conférence des Présidents d'Université (CPU) e la Conferenza dei Rettori delle Università Italiane (CRUI) sul riconoscimento dei diplomi e della validità dei titoli universitari siglata in data 18 gennaio 1996;
- La convenzione franco-italiana tra la Conférence des Présidents d'Université (CPU) e la Conferenza dei Rettori delle Università Italiane (CRUI) sulla cotutela di tesi siglata li 13 febbraio 1998;

nell'intento di contribuire ad instaurare e/o sviluppare la cooperazione scientifica tra équipes di ricerca italiana e straniera attraverso la mobilità dei dottorandi

convengono e stipulano quanto segue

Parte prima – Modalità amministrative

Art. 1 – L'Università degli Studi di Roma "La Sapienza" e L'INSA di Lione denominati qui di seguito "Istituzioni" concordano, nel rispetto delle leggi e dei regolamenti in vigore in ciascun Paese e/o Istituzione, di organizzare congiuntamente una co-tutela di tesi di dottorato a beneficio del dottorando sottoindicato:

nome e cognome: Giovanna LACERRA

iscritto al corso di Dottorato di Ricerca in Meccanica Teorica e Applicata presso l'Università La Sapienza di Roma e in "Mecanique" presso l' "école doctorale MEGA".

Soggetto di tesi: **Energia ed analisi fenomenologica delle vibrazioni indotte per attrito: trasferimento d'energia tra campi acustici attraverso le non-linearità dell'attrito.**

I sistemi meccanici con contatti striscianti sono soggetti a vibrazioni che vengono generate nell'interfaccia di contatto e che successivamente propagano nei solidi. Una parte d'energia è dissipata al contatto mentre una parte non trascurabile viene restituita al sistema sotto forma di onde propaganti all'interfaccia di contatto e nel volume, dando origine alle cosiddette "vibrazioni indotte dall'attrito".

Lo scopo di questa tesi è quello di combinare la caratterizzazione locale del contatto, dal punto di vista tribologico, e la caratterizzazione della dinamica non lineare del sistema. La tesi si pone l'obiettivo di avere un approccio alla comprensione delle vibrazioni indotte dall'attrito, prendendo in considerazione sia il comportamento del contatto locale che la risposta dinamica del sistema. L'energia che scambiata tra la superficie e il volume (e quindi il sistema) e viceversa, verrà quantificata per caratterizzare le vibrazioni indotte dall'attrito da un punto di vista energetico. Possono essere citate numerose applicazioni, in domini differenti: smorzamento dovuto al contatto (dissipazione d'energia) studiato nella dinamica non lineare delle strutture (blade dampers); trasferimenti d'energia tra campi acustici dovuti alle non linearità di contatto (monitoraggio passivo dello stato di salute di una struttura, recupero d'energia, ...); stick-slip e instabilità modali al contatto (terremoti, brake squeal, cigolio dell'enprotesi per l'anca, vibrazioni dei macchinari, ...); usura dovuta alle vibrazioni (fretting, falso effetto Brinelling, ...).

Da un lato, delle campagne sperimentali saranno dedicate alla caratterizzazione delle vibrazioni indotte d'attrito, studiate in un contesto generale come funzione della superficie e dei parametri del sistema, per capire i fattori chiave e definire delle leggi di contatto appropriate da implementare nei codici numerici; una legge numerica di tipo perturbativo dell'attrito sarà ricercata per riprodurre l'eccitazione dovuta al contatto, misurata sperimentalmente, con risorse numeriche ragionevoli. L'originalità dell'approccio proposto si deve al fatto di aver preso in considerazione l'accoppiamento della risposta del sistema con l'eccitazione al contatto grazie alla progettazione di un banco di prova che non cerchi di disaccoppiarli; semplificando la dinamica del sistema sarà possibile correlarla con i risultati ottenuti.

Dall'altro lato sarà sviluppata un'analisi sperimentale per quantificare il trasferimento d'energia tra campi acustici, ottenuto grazie all'eccitazione a banda larga generata dal contatto d'attrito, come funzione dei parametri, quali lo spettro d'eccitazione, la forza di contatto, la rugosità superficiale, etc.

Sarà portata avanti un'analisi numerica con modelli a parametri concentrati e agli elementi finiti, parallelamente a test sperimentali per la riproduzione del fenomeno fisico e lo studio del comportamento del contatto locale. L'analisi numerica ha il doppio obiettivo di comprendere il comportamento del locale (impossibile da studiare sperimentalmente) e definire algoritmi innovativi per il contatto e leggi d'attrito capaci di riprodurre realistiche vibrazioni indotte d'attrito in classici modelli agli elementi finiti senza infittire la mesh al contatto. Quest'ultimo obiettivo permetterà di tener conto dei fenomeni studiati senza introdurre tempi computazionali troppo dispendiosi.

I principi e le modalità amministrative e didattiche di tale co-tutela sono definiti dalla presente convenzione.

Art.2 - La durata per la preparazione della tesi è di 3 anni, a partire dall'anno accademico 2014/2015.

Art.3 - La preparazione della tesi si effettuerà in periodi alterni, pressoché equivalenti, in ciascuna delle due Istituzioni. La durata di tali periodi sarà fissata in comune accordo dai due Direttori di tesi.

Art.4 – Il dott. Giovanna Lacerra sarà iscritto in entrambe le Istituzioni. Corrisponderà i regolari diritti di iscrizione all’INSA di Lione e sarà esonerato dal pagamento delle tasse presso l’Università “La Sapienza” di Roma, presso cui corrisponderà annualmente solo i diritti di segreteria.

Art.5 - Per tutto il periodo di preparazione della tesi il dott. Giovanna Lacerra beneficerà di quanto disposto dalla delibera del 7 Agosto 2006 e della carta dei tesisti de l’INSA de Lyon.

Art.6 - Per la durata della sua iscrizione, il dott. Giovanna Lacerra dovrà fornire giustificazione relativamente alle sue risorse, alla sua copertura sanitaria così come alla sua assicurazione sugli incidenti di lavoro, in ognuno dei paesi.

Parte seconda – Modalità didattiche

Art.1 – Il dott. preparerà la tesi sotto la direzione comune dei professori:

- Aurélien SAULOT (Docente presso il Laboratorio di Meccanica dei Contatti e delle Strutture), direttore di tesi all’INSA di Lione
- Francesco MASSI (Docente presso il Dipartimento di Ingegneria Meccanica e Aerospaziale), direttore di tesi a l’Università di Roma “La Sapienza”)

che si impegnano ad esercitare pienamente la funzione di tutori del dottorando e si impegnano a valutarne, ciascuno con propria relazione scritta, la tesi di Dottorato.

Il giudizio positivo di entrambi i Direttori di Tesi è condizione necessaria per l’ammissione all’esame finale.

Art. 2 - La discussione della tesi, unica e riconosciuta dalle due istituzioni, avrà luogo presso l’INSA di Lione. La Commissione giudicatrice, nominata dai Rettori delle due Università, sarà composta da un numero pari di studiosi appartenenti alle due Istituzioni e designati congiuntamente da esse, oltre a membri esterni alle due Istituzioni. Essa dovrà essere composta da un minimo di quattro membri ed un massimo di otto, appartenenti ai settori scientifico-disciplinari del Dottorato, tra cui, a meno di derogazioni, i due direttori di tesi.

Art. 3 – La tesi sarà redatta e discussa in inglese; un riassunto sostanziale sarà redatto in lingua francese ed in lingua italiana.

Art. 4 – Ognuna delle due Istituzioni si impegna a conferire il titolo di dottore di ricerca per la stessa tesi, in seguito ad una relazione favorevole della Commissione giudicatrice.

L’Università degli Studi di Roma “La Sapienza” conferirà il titolo di dottore di ricerca in Meccanica Teorica e Applicata.

L’INSA di Lione conferirà il titolo di dottore di ricerca in Meccanica.

Art. 5- In caso il dottorando dovesse convalidare le formazioni complementari (scientifiche o mirate alla sua inserzione professionale), le Istituzioni (l’Ecole Doctorale MEGA pour l’INSA) specificeranno le modalità di riconoscimento reciproco di queste formazioni, in accordo con i direttori di tesi ed il dottorando.

Parte terza – Conclusioni

Art. 1 – Il dottorando dovrà rispettare i regolamenti e le consuetudini dell’Istituzione ospitante.

Art. 2 – Le Istituzioni contraenti, attraverso l’intermediazione dei rispettivi direttori di tesi, si impegnano a comunicarsi rispettivamente tutte le informazioni e la documentazione utile per l’organizzazione della co-tutela di tesi oggetto della presente convenzione.

Art. 3 – Le modalità di presentazione, di deposito e riproduzione della tesi saranno effettuati in ogni paese secondo i regolamenti in vigore.

La protezione dell’oggetto della tesi, così come la pubblicazione, lo sfruttamento e la protezione dei risultati ottenuti con lo studio di ricerca del dottorando nelle Istituzioni contraenti saranno assoggettati alla normativa in vigore e assicurati conformemente alle procedure specifiche di ciascun Paese coinvolto nella co-tutela.

Qualora richiesto, le disposizioni relative alla protezione dei diritti di proprietà intellettuale potranno costituire oggetto di protocolli o documenti specifici.

Art. 4 – La presente convenzione entra in vigore dalla data di firma del rappresentante legale di ciascuna Istituzione contraente e sarà valida fino alla fine dell’anno accademico nel corso del quale la tesi o lo studio saranno discussi. Nel caso in cui il dottorando non fosse iscritto in una e/o l’altra delle Istituzioni contraenti, oppure rinunciasse per iscritto a proseguire, oppure, in virtù della decisione di almeno uno dei due direttori di tesi, non fosse autorizzato a proseguire la preparazione della tesi in co-tutela, le Istituzioni contraenti potranno fine, congiuntamente e senza ritardo, alle disposizioni del presente accordo.

Art. 5 – La presente convenzione è redatta in quattro esemplari originali, di cui due in lingua italiana e due in lingua francese, aventi valore legale.

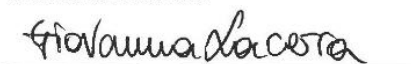
Roma, li 11 NOV. 2014

Per il Rettore dell’Università
di Roma “La Sapienza”


Il Responsabile del Dottorato di Ricerca
Carlo Massimo CASCIOLA

Co-direttore di tesi
Francesco MASSI


Il Dottorando
Giovanna Lacerra



Villeurbanne, li 15 OCT. 2014

Per il Direttore dell’INSA de Lyon
DR Marie Christine BALETTO
Addetta alla Direzione della Ricerca
E degli Studi di Dottorato


Il Responsable del Dottorato di Ricerca
Philippe BOISSE


Il Direttore del laboratorio
David DUREISSEIX

Co-direttore di tesi
Aurélien SAULOT



Friction-Induced Vibrations as a result of system response and contact dynamics: a newer friction law for broadband contact excitation.

Résumé substantiel

Ce travail s'inscrit dans le cadre de recherches autour des vibrations induites par frottement(sec), domaine à cheval entre l'étude du contact, la tribologie et la dynamique des structures. Il concerne l'étude des vibrations émises entre deux corps en contact glissant. En présence de deux corps en contact présentant un mouvement relatif de glissement, un transfert d'énergie survient : une partie de l'énergie cinétique des solides est transférée à l'interface du contact sous forme de phénomènes locaux, (impulsions, contacts, détachements et déformations des aspérités entre les deux corps..). Ces phénomènes engendrent des ondes qui se propagent via les surfaces en contact jusqu'aux solides en mouvement. A leur tour, ces solides répondent à cette voie d'excitation en vibrant selon leurs fréquences et modes naturels, produisant ainsi les vibrations dites induites par frottement.

Le frottement, à l'origine des vibrations entre deux solides en contact, est étudié depuis de nombreux siècles. Leonardo da Vinci [1] a été en effet le premier scientifique à mener des essais afin de comprendre l'origine et la dynamique de ce phénomène. Il réussit à découvrir les deux hypothèses à la base des lois de frottement d'Amontons-Coulomb. Et cela deux siècles avant qu'Amontons [2] ne puisse les formuler. Il découvrit que le frottement est proportionnel à la charge normale imposée et qu'il est indépendant de la zone de contact. Après Amontons se succédèrent Eulero, Coulomb [3] et Hertz [4]. Ces chercheurs firent la distinction entre frottement statique et dynamique à partir d'analyses quantitatives du frottement sec et des efforts de contact agissant à l'interface.

Ce n'est qu'au cours du vingtième siècle que les recherches de Bowden et Tabor [5, 6, 7] permirent de passer de l'étude de surfaces lisses à l'étude de surfaces rugueuses, introduisant la distinction entre zone de contact réelle et zone de contact apparente. Grâce à leur travail naquit une nouvelle approche dans l'étude de la tribologie à laquelle firent suite de nombreux travaux de recherches (Archard [8], Greenwood et Williamson [9], Bush [10], ...) et ce, jusqu'à nos jours avec la théorie récente de Persson [11].

Ce bref et non exhaustif excursus de la littérature permet de souligner comment l'analyse du frottement en tant que cause de la force résistante au mouvement a été amplement étudiée au cours des siècles. En revanche, l'approche de type énergétique, qui considère les forces agissant au cœur du contact comme sources

d'énergie vibratoire, à l'origine de nombreuses applications au sein de la mécanique (structural health monitoring, blade dampers, brake squeal), n'a pas été encore suffisamment approfondie.

Dans ce contexte, le travail engagé se concentre sur l'analyse des Vibrations Induites par Frottement, en anglais FIV pour Friction-Induced Vibrations.

Après la reproduction et l'analyse des vibrations induites sur deux bancs d'essais dédiés, une nouvelle approche numérique a été introduite, à même de reproduire l'excitation au contact dans la réponse du système dynamique. Le système dynamique choisi pour cette analyse est composé de deux solides, 2 poutres en acier en condition de contact glissant, Figure 1b. Le système choisi est caractérisé par une dynamique simple, de façon à pouvoir distinguer dans la réponse totale du système l'excitation à large bande provenant de la dynamique du contact de la dynamique du système même.

Le travail se structure de la manière suivante: le premier chapitre présente une synthèse des recherches les plus importantes dans le cadre des vibrations induites par frottement; une attention spéciale étant portée sur des problématiques complexes comme les instabilités dynamiques et l'émission acoustique. En outre une description des modèles de contact proposés dans la littérature permettant d'étudier le contact entre surfaces rugueuses est présentée. Enfin, dans le même chapitre, le travail réalisé se positionne au regard de cet état de l'art.

Le deuxième chapitre décrit l'approche choisie pour étudier les vibrations induites par frottement. La première partie concerne l'approche expérimentale. En particulier les deux bancs d'essais utilisés pendant les campagnes expérimentales sont présentés. Ces bancs dédiés, respectivement dénommés TriboTouch et TriboAir (Figure 1 et Figure 2) sont capables de reproduire un mouvement relatif entre deux éléments en contact sans introduire de bruits parasites dans les mesures. Par ailleurs le procédé de polissage auquel les poutres sont soumises avant chaque mesure est décrit. Un tel polissage, permet d'obtenir des propriétés superficielles de surfaces spécifiques en terme de rugosité.

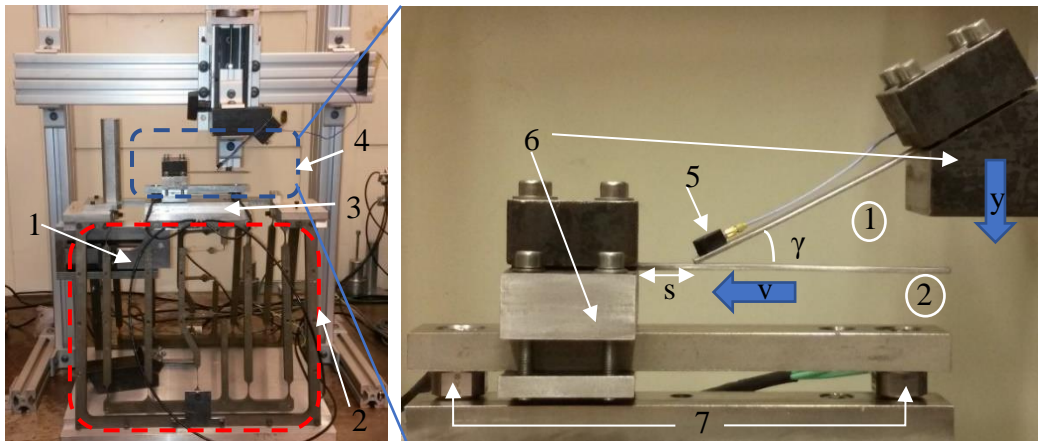


Figure 1 : a) Banc d'essai TriboTouch, (1) couple bobine-aimant, (2) dispositif compliant, (3) base supérieure, (4) système de blocage ; b) Agrandissement du banc d'essai sur le système de blocage des poutres, (5) accéléromètre, (6) masses de blocage, (7) capteurs de force

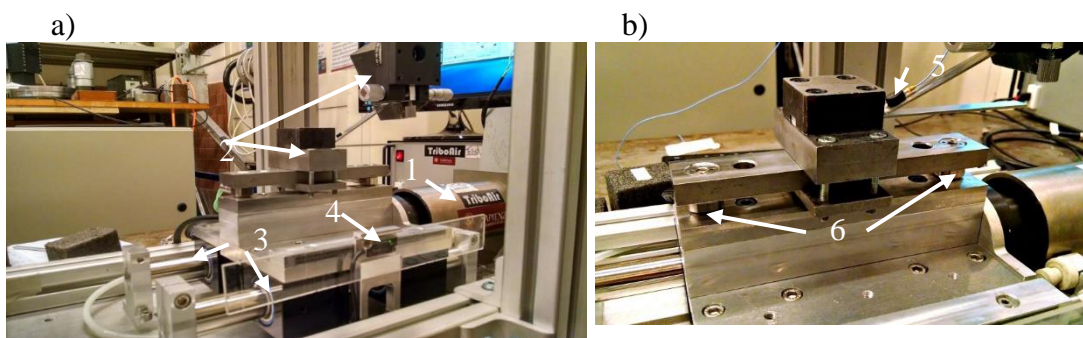


Figure 2: Banc d'essai TriboAir; (1) couple aimant-bobine, (2) masses de blocage, (3) guide avec paliers à coussin d'air, (4) encodeur linéaire optique; b) agrandissement des poutres en contact glissant, (5) accéléromètre, (6) capteurs de force

La deuxième partie du second chapitre présente les outils d'analyse du modèle numérique développé dans l'objectif de simuler les mêmes phénoménologies que celles observées expérimentalement (Figure 3). Pour étudier la réponse vibratoire du système, une analyse aux valeurs propres (eigenvalues) complexes a été conduite. Cette analyse détermine le cas échéant les éventuelles instabilités dynamiques et est poursuivie par une analyse dynamique transitoire. Finalement, la dernière partie du chapitre détaille la loi de frottement introduite pour simuler l'excitation à bande large engendrée par les phénomènes au contact.

Le troisième chapitre décrit la campagne expérimentale effectuée pour caractériser la réponse dynamique du système. La première partie porte sur la caractérisation du système par identification de ses fréquences naturelles et les coefficients modaux d'amortissement associés. La deuxième partie décrit le

protocole suivi pour les mesures du système mécanique en présence d'éléments frottants au contact. Les réponses du système dans les domaines temporel et spectral sont illustrées en Figure 4 et Figure 5. La troisième partie présente les résultats de la campagne expérimentale paramétrique menée pour quantifier l'influence de trois paramètres au contact que sont la charge normale, la vitesse de glissement et la rugosité superficielle. De cette manière, il a été possible de caractériser la réponse du système dynamique et, plus particulièrement, les vibrations induites par frottement, estimées à partir de l'évolution spectrale des réponses dynamiques et de la valeur RMS (Root Mean Square) moyenne de l'accélération mesurée dans le temps.

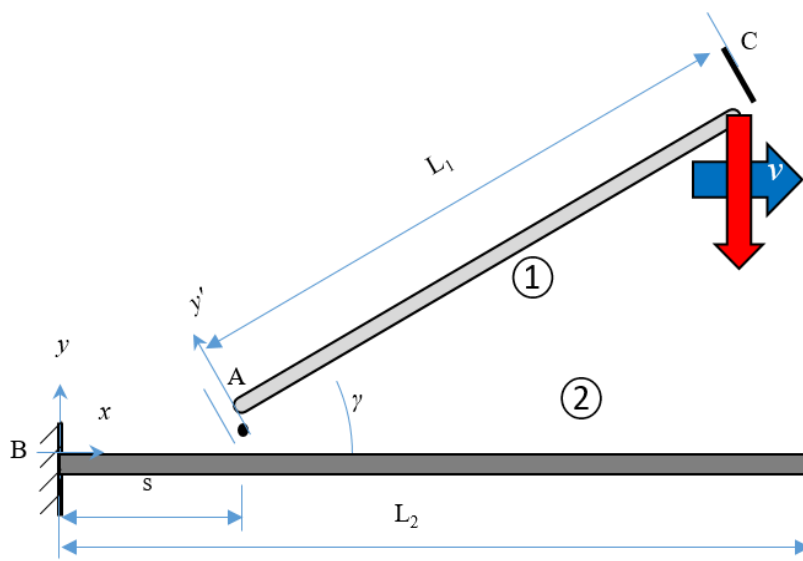


Figure 3: Modèle numérique 2D des poutres en contact glissant

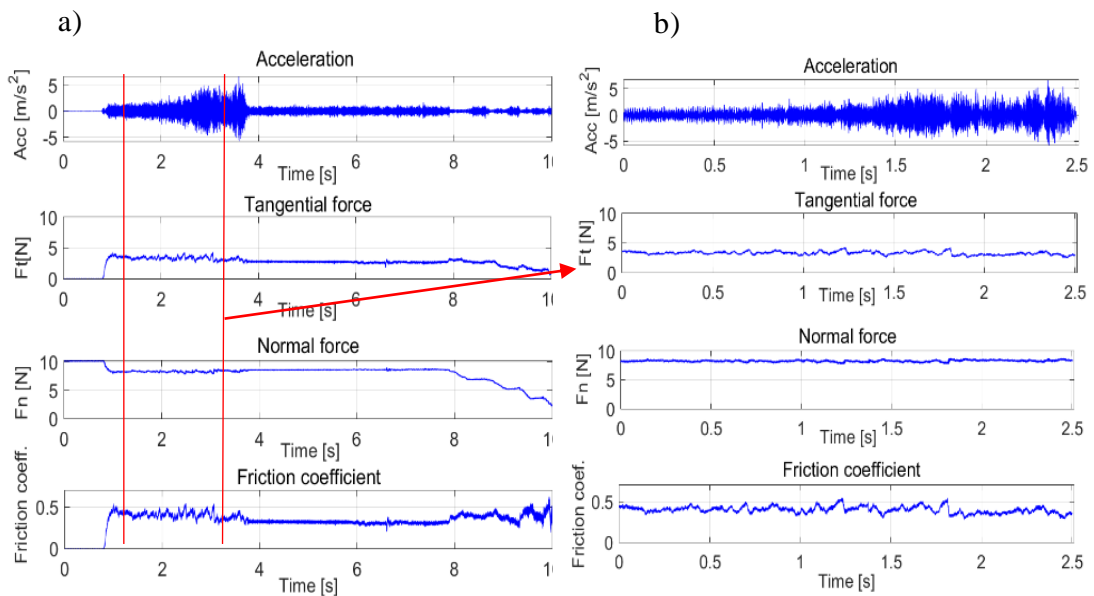


Figure 4 : a) Réponse du système expérimentale en terme d'accélération de la poutre supérieure, force normale (F_n), force tangentielle (F_t) et coefficient de frottement; b) Sélection de la phase de glissement stable

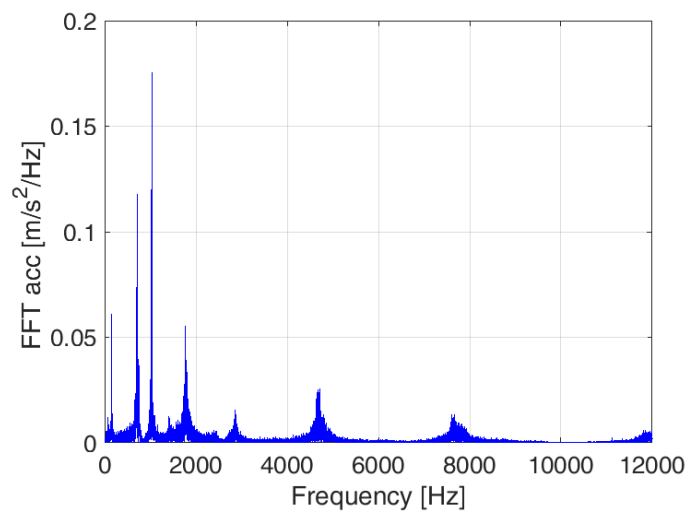


Figure 5 : FFT du système couplé (poutres en contact), charge normale 8N, vitesse de glissement 8 mm/s.

L'étude expérimentale a permis de mettre en évidence trois évolutions caractéristiques:

- L'augmentation de la charge normale imposée au contact détermine une évolution de l'amplitude des vibrations qui se subdivise en quatre zones: la première zone correspond à une zone de contact dite faible (weak contact

condition). Elle se caractérise par de grandes amplitudes de vibrations, les 2 poutres constituant un système quasi découplé; la deuxième zone présente une évolution plus chaotique, dû à la transition du système passant d'une condition de contact faible à une condition de contact dit "fort" (strong contact condition); la troisième zone entre définitivement dans la zone de contact fort, les poutres peuvent être considérées comme un système couplé et l'augmentation de la charge normale correspond à une augmentation de l'amplitude des vibrations; la dernière zone traduit la plastification des aspérités due à une charge excessive. Dans cette phase, l'augmentation de la charge normale induit une diminution des niveaux de réponse vibratoire (Figure 6);

- L'augmentation de la vitesse de glissement a montré une augmentation de l'amplitude des vibrations induites par frottement. Elle est due à l'augmentation de la puissance échangée au contact entre les surfaces qui, à son tour, provoque une augmentation de l'amplitude de l'énergie vibratoire réinjectée dans le système (Figure 7);
- Le changement de la rugosité superficielle des éprouvettes a mis en évidence une augmentation du contenu énergétique des vibrations induites. Ce comportement est dû à une augmentation du contenu énergétique relâché par l'interaction d'aspérités plus importantes, en introduisant impacts et ruptures avec plus d'énergie, et donc de plus grandes amplitudes de vibrations induites, Figure 8.

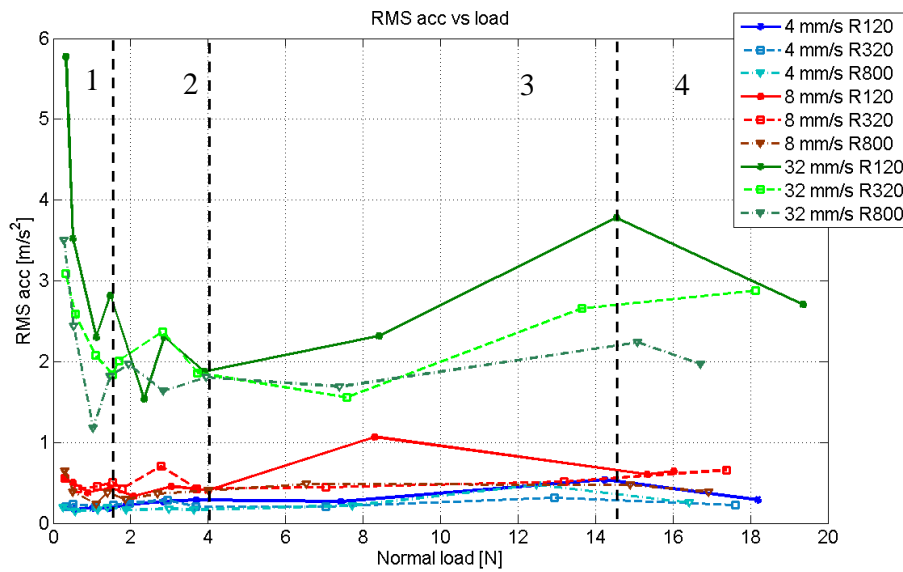


Figure 6: Valeur quadratique RMS moyenne de l'accélération vs la charge normale; superposition de l'évolution des trois rugosités et trois vitesses de glissement : courbes vertes pour 32 mm/s, rouges 8 mm/s, bleu 4 mm/s

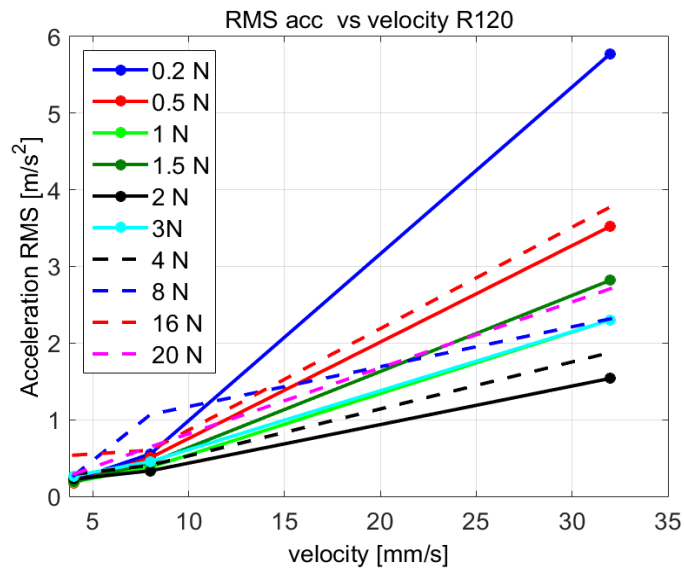


Figure 7: Valeur quadratique moyen (RMS) de l'accélération des vibrations induites vs vitesse de glissement

La campagne expérimentale a finalement servi à identifier les caractéristiques dynamiques du système et à évaluer les vibrations induites par frottement. Les

quatrième et cinquième chapitres s'attachent à décrire et à étudier le modèle numérique développé pour simuler les vibrations induites, et notamment retranscrire l'excitation à bande large du contact.

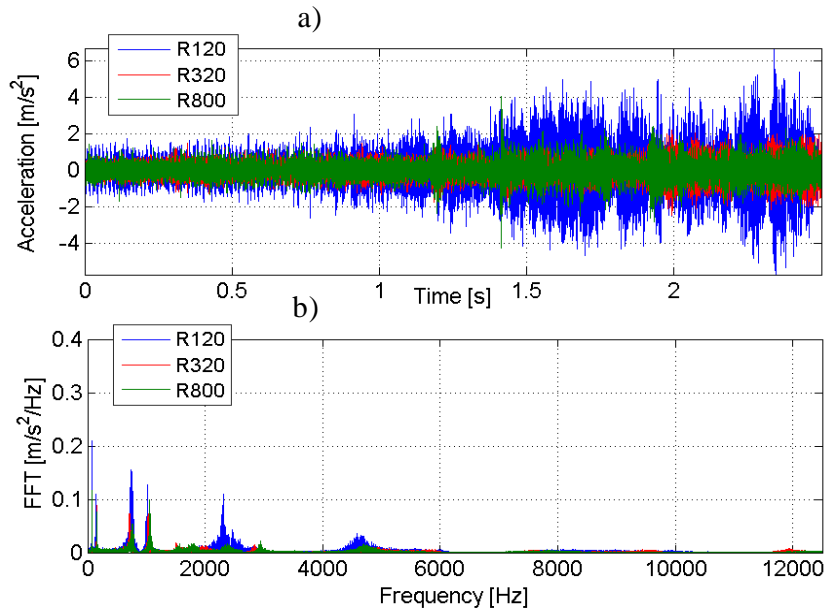


Figure 8 : a) Superposition entre l'évolution temporelle de l'accélération pour les trois rugosités; b) Superposition de la FFT de l'accélération, charge normale 8N, vitesse de glissement 8 mm/S

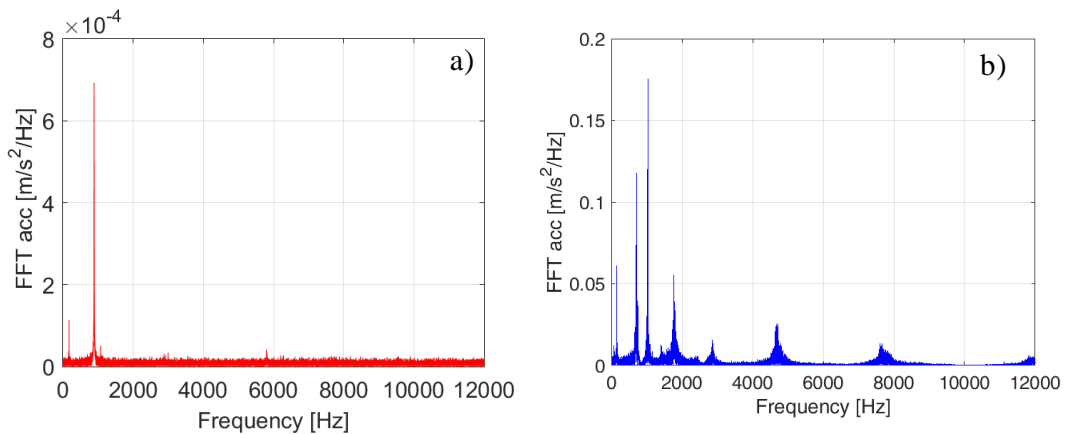


Figure 9 : Comparaison entre l'évolution spectrale de la FFT pour l'accélération numérique (a) et expérimentale (b)

Un modèle numérique bidimensionnel a donc été développé à partir de la méthode aux éléments finis (MEF) Une analyse préliminaire aux valeurs propres complexes a été développée afin de déterminer les dimensions géométriques des poutres évitant l'apparition d'instabilités dynamiques causées par le couplage modal des 2 sous-systèmes. Par la suite, une première analyse paramétrique a été effectuée sans considérer la présence de l'excitation dynamique au contact. C'est-à-dire en utilisant la loi classique de frottement de Coulomb avec un coefficient de frottement considéré constant.

En comparant les résultats numériques et expérimentaux fournis, Figure 9, la nécessité d'introduire une excitation large bande dans le modèle de contact afin de reproduire correctement les vibrations induites lors du glissement relatif des 2 poutres s'est avérée indispensable.

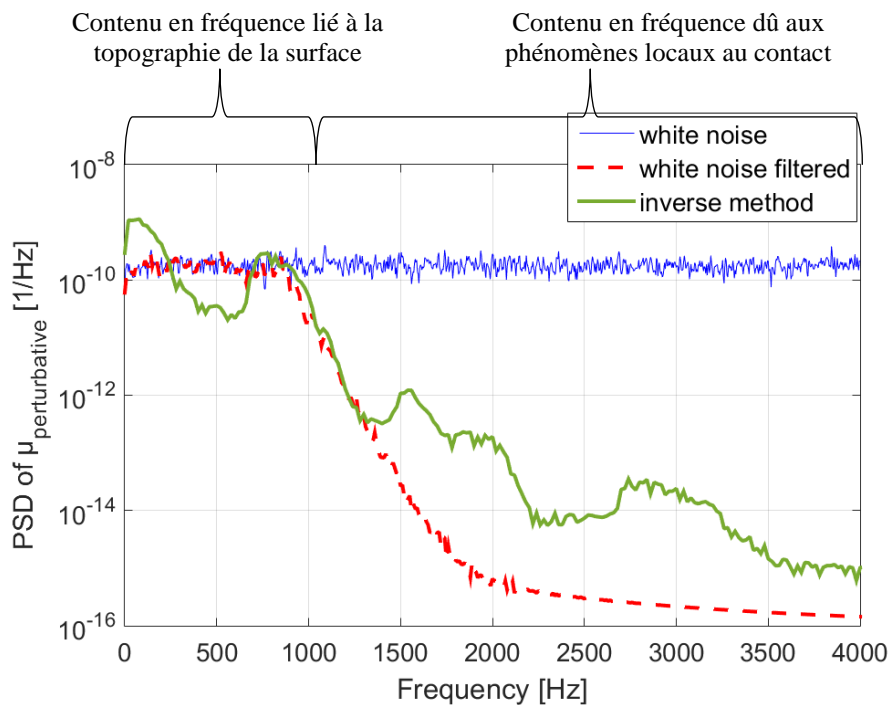


Figure 10 : Superposition de l'évolution spectrale pour les trois signaux testés pour le terme $R(x)$: bruit blanc (bleu), bruit blanc filtré avec un filtre Butterworth (rouge hachuré), de la méthode inversée (verte).

La nouvelle loi de frottement introduite dans le modèle numérique utilise un coefficient de frottement composé par deux termes : un terme constant comme défini par la loi de Coulomb et un terme dit de perturbation, à même de retranscrire

l'excitation large bande générée par le contact en présence de frottement entre les deux surfaces des solides, Eq.I.

$$\mu(x) = \mu_{const} + \mu_{perturbative} \quad \text{Eq. I}$$

Afin de reproduire correctement les vibrations induites par le frottement mesurées pendant la campagne expérimentale, trois distributions spectrales différentes ont été analysées et sont illustrées, Figure 10. Elles correspondent respectivement à un bruit blanc, à un bruit blanc filtré par un filtre Butterworth et à une distribution calculée par méthode inverse à partir de l'accélération mesurée proche du contact. L'influence de chaque distribution spectrale sur la réponse dynamique du système a été étudiée par l'intermédiaire du terme de perturbation de la loi de frottement. Il a été constaté que le signal qui réussit à reproduire le plus fidèlement l'excitation au contact est celui provenant de la méthode inverse. En effet il est le seul apte à reproduire les deux contributions de l'excitation de contact :

- La première contribution est liée à la topographie même de la surface qui excite le système dans la bande des basses fréquences ;
- La seconde contribution est relative à la nature impulsive de l'excitation locale au contact engendrée par phénomènes tels ruptures, impacts entre les aspérités et qui excite le système dans une large bande.

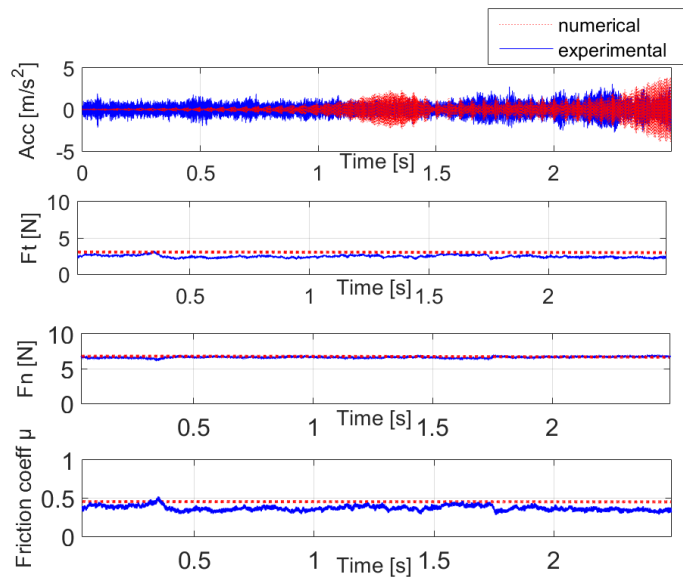


Figure 11: évolution dans le temps numérique (rouge) et expérimentale (bleu) de l'accélération de la poutre supérieur. Le signal choisi pour le terme $R(x)$ est récupéré par méthode inversée. Rugosité superficiel R320

La loi de frottement proposée a été validée par corrélation entre résultats numériques et expérimentaux. En effet, ces derniers présentent une évolution de l'accélération numérique en accord avec celle mesurée expérimentalement comme observé en Figure 11 et Figure 12.

La nouvelle loi de frottement a été évaluée pour deux rugosités superficielles différentes et deux vitesses de glissement différentes. Encore une fois, les résultats numériques sont en accord avec ceux mesurés expérimentalement.

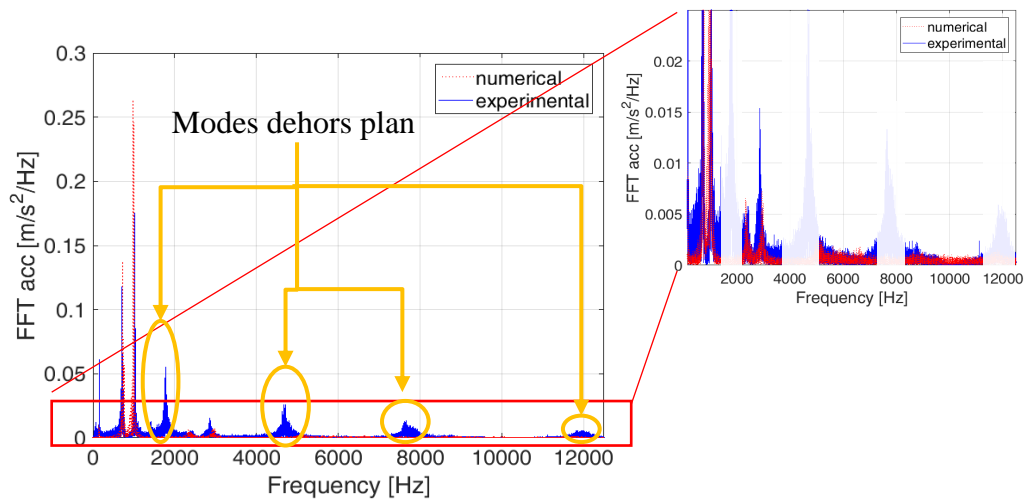


Figure 12 : Superposition entre l'évolution numérique (rouge) et expérimental (bleu) de la FFT de l'accélération; le signal choisi pour $R(x)$ celui récupéré par la méthode inversée avec agrandissement de la FFT. Rugosité superficiel R320.

En conclusion, la loi de frottement proposée est apte à reproduire correctement les vibrations induites par frottement sans introduire une représentation de la topographie réelle de la surface qui demanderait un nombre très élevé d'éléments au contact. L'introduction des effets dynamiques des phénomènes de contact dans le terme de perturbation du coefficient de frottement a ainsi permis de reproduire les vibrations induites par frottement sans augmenter les coûts de calculs numériques, contrairement aux méthodes prenant en compte la géométrie réelle ou estimée de la rugosité.

Friction-Induced Vibrations as a result of system response and contact dynamics: a newer friction law for broadband contact excitation

Riassunto sostanziale

Questo lavoro è stato sviluppato nel contesto di ricerca sulle vibrazioni indotte dall'attrito, a cavallo fra la meccanica del contatto, la tribologia e la dinamica. Ogni qualvolta due corpi sono posti in contatto strisciante, avviene un trasferimento d'energia: una parte dell'energia cinetica dei solidi viene trasferita all'interfaccia di contatto sotto forma di fenomeni locali (impulsi, contatto, distacco, deformazione delle asperità, ...). Tali fenomeni generano delle onde che si propagano dalle superfici a contatto fino ai solidi in movimento, che, a loro volta, rispondono all'eccitazione vibrando secondo la loro dinamica, producendo così le cosiddette vibrazioni indotte dall'attrito.

L'attrito, all'origine delle vibrazioni fra due solidi in contatto, viene studiato sin dai tempi di Leonardo da Vinci [1], che per primo ha condotto esperimenti per comprendere l'origine e le caratteristiche di questo fenomeno. Egli scoprì le due assunzioni alla base della legge d'attrito di Amontons-Coulomb, due secoli prima che Amontons [2] potesse affermarle: l'attrito è proporzionale al carico normale imposto ed è indipendente dall'area di contatto. Dopo Amontons si susseguirono Eulero, Coulomb [3] e Hertz [4], analizzando la differenza fra attrito statico e dinamico, introducendo analisi quantitative per l'attrito secco e valutando infine le forze di contatto che agiscono all'interfaccia.

Solo nel ventesimo secolo, con Bowden e Tabor [5, 6, 7], si passò dallo studio di superfici lisce allo studio di superfici rugose, introducendo la distinzione tra area di contatto reale ed apparente. Grazie al loro lavoro nacque un nuovo approccio nello studio della tribologia, a cui fece seguito il lavoro di Archard [8], Greenwood e Williamson [9], Bush [10], fino ai nostri giorni con la teoria di Persson [11].

Questo breve excursus nella letteratura permette di evidenziare come l'analisi dell'attrito in quanto causa della forza resistente al movimento sia stato negli anni ampiamente studiato; contrariamente, l'approccio di tipo energetico, che consideri le forze agenti al contatto come sorgenti d'energia vibrazionale, di interesse per numerose applicazioni in ambito meccanico (structural health monitoring, blade dampers, brake squeal...), non è stato ancora del tutto approfondito.

In questo poliedrico contesto, il lavoro svolto si concentra sull'analisi delle vibrazioni indotte dall'attrito (in inglese FIV: Friction-Induced Vibrations). Dopo la riproduzione e l'analisi delle vibrazioni indotte su set-up dedicati, è stato introdotto un nuovo approccio numerico atto ad introdurre l'effetto dell'eccitazione dinamica al contatto nella risposta del sistema dinamico. Il sistema dinamico scelto per questa analisi è composto da due solidi, travi in acciaio, in condizioni di contatto strisciante (Figura 1b). È stato volutamente scelto un sistema caratterizzato da una dinamica semplice, in modo da poter distinguere l'eccitazione a banda larga proveniente dal contatto dalla dinamica del sistema stesso.

Entrando nel dettaglio della struttura del lavoro, il primo capitolo presenta una sintesi sulle ricerche più importanti nell'ambito delle vibrazioni indotte, con particolare attenzione alle relative problematiche, quali le instabilità dinamiche e l'emissione acustica; viene inoltre presentata una descrizione dei modelli di contatto proposti nella letteratura per studiare il contatto fra superfici rugose. Infine, nello stesso capitolo, il lavoro svolto viene inquadrato rispetto la letteratura analizzata.

Il secondo capitolo descrive l'approccio scelto per studiare le vibrazioni indotte dall'attrito. La prima parte riguarda l'approccio sperimentale, dove vengono in particolare presentati i due set-up utilizzati durante la campagna sperimentale, il TriboTouch (Figura 1) ed il TriboAir (Figura 2), capaci di riprodurre un movimento relativo fra i due elementi in contatto senza introdurre rumore parassita nelle misure; infine, il protocollo seguito per i test sperimentali è descritto.

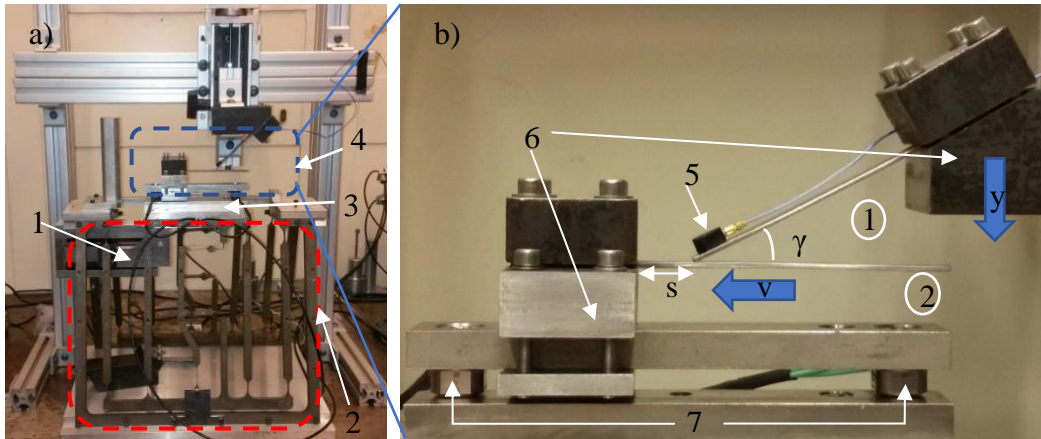


Figura 1: a) set.up Tribotouch, (1) coppia bobina-magnete, (2) dispositivo compliant, (3) base superiore, (4) sistema di bloccaggio delle travi; b) ingrandimento del set-up sul sistema di bloccaggio delle travi, (5) accelerometro, (6) masse di bloccaggio, (7) trasduttori di forza.

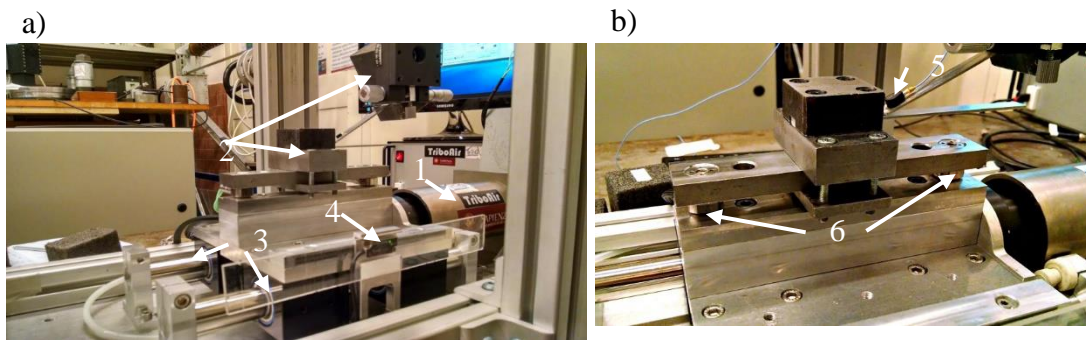


Figura 2: a) il set-up Tribotouch: (1) coppia magnete-bobina, (2) masse di bloccaggio (3) guide con cuscinetti ad aria (4) encoder lineare ottico; b) ingrandimento delle travi in contatto strisciante (5) accelerometro (6) trasduttori di forza

La seconda parte del secondo capitolo descrive gli strumenti utilizzati per lo sviluppo del modello numerico, sviluppato al fine di simulare gli stessi fenomeni osservati sperimentalmente (Figura 3). Per studiare la dinamica del sistema sono state condotte analisi agli autovalori complessi, per individuare eventuali instabilità dinamiche; per riprodurre il contatto strisciante sono state condotte analisi transitorie. L'ultima parte del capitolo descrive infine la legge d'attrito che è stata introdotta per simulare l'eccitazione a banda larga generata dai fenomeni locali all'interfaccia di contatto.

Il terzo capitolo descrive la campagna sperimentale svolta per caratterizzare la risposta vibrazionale del sistema in contatto. La prima parte caratterizza il sistema

identificando le sue frequenze naturali ed i coefficienti di smorzamento modale. La seconda parte descrive le misure effettuate, mostrando la risposta del sistema nel dominio temporale e spettrale (Figura 4 e Figura 5). La terza parte presenta i risultati della campagna parametrica sperimentale, portata avanti per analizzare l'influenza di tre parametri al contatto: carico normale, velocità di strisciamento e rugosità superficiale. In questo modo è stato possibile caratterizzare la risposta del sistema dinamico ed in particolare le vibrazioni indotte dall'attrito, mostrando l'evoluzione spettrale ed il valor quadratico medio (RMS) dell'accelerazione misurata nel tempo.

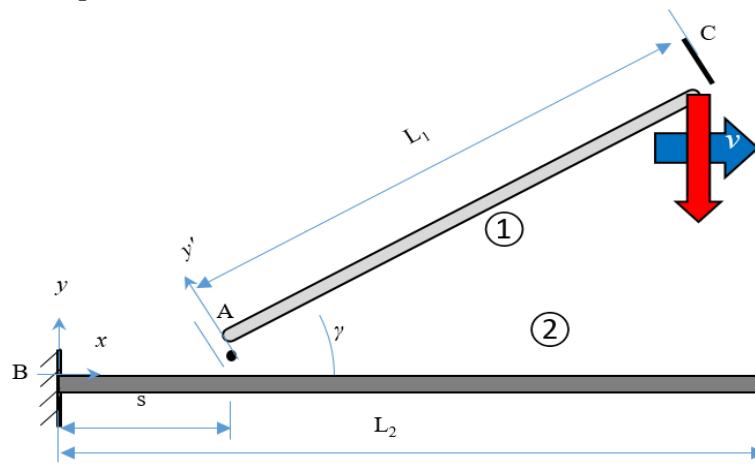


Figura 3: modello numerico 2D delle travi in contatto strisciante

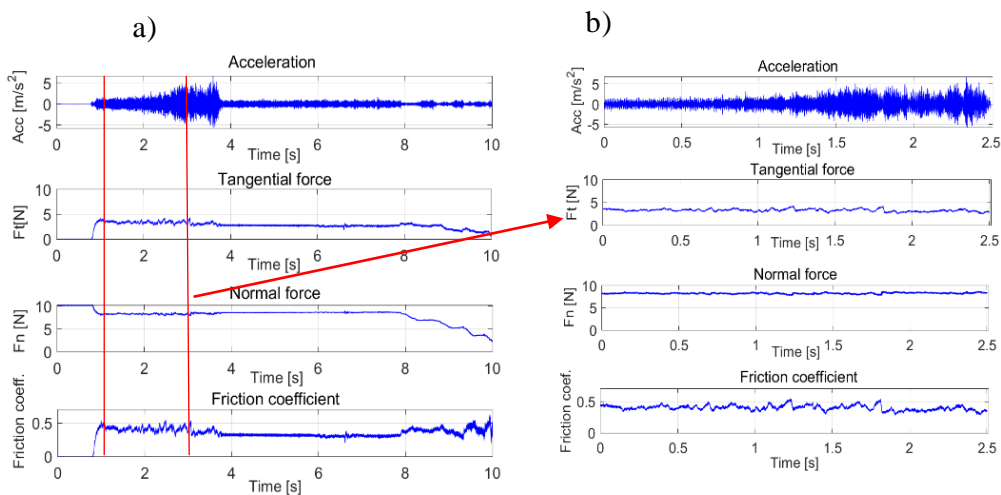


Figura 4: a): risposta del sistema sperimentale in termini di accelerazione, forza normale (F_n), forza tangenziale (F_t) e coefficiente d'attrito; b) selezione della fase di strisciamento stabile

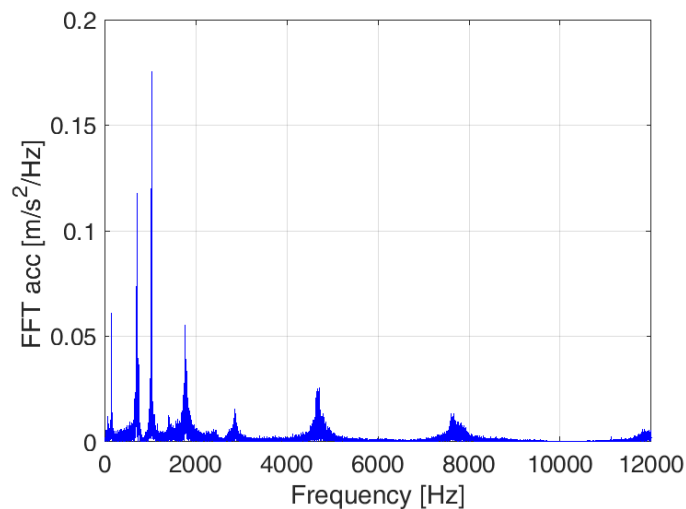


Figura 5: FFT dell'accelerazione; carico normale 8N, velocità di strisciamento 8 mm/s.

Tre evoluzioni caratteristiche sono state individuate dall'analisi sperimentale:

- Un aumento del carico normale imposto al contatto determina un'evoluzione dell'ampiezza delle vibrazioni che si articola in quattro zone: inizia con una zona di *contatto debole*, caratterizzata da una grande ampiezza delle vibrazioni, e dalle due sottostrutture che risultano debolmente accoppiate; la seconda zona ha un trend caotico, dovuto alla transizione del sistema da condizioni di *contatto debole* ad un *contatto forte*; la terza zona entra definitivamente nella condizione di *contatto forte*, le travi possono essere considerate come un sistema accoppiato e l'incremento del carico normale corrisponde ad un incremento dell'ampiezza delle vibrazioni; l'ultima zona è caratterizzata dalla presenza della plastificazione delle asperità, dovuta ad un carico eccessivo; in questa ultima fase una crescita del carico normale determina una diminuzione della risposta vibrazionale (Figura 6);
- Un incremento della velocità ha mostrato un aumento nell'ampiezza delle vibrazioni indotte dall'attrito, dovuto all'aumento della potenza scambiata al contatto fra le superfici, che determina una crescita nell'ampiezza dell'energia vibrazionale reimmessa nel sistema (Figura 7);
- Un aumento della rugosità superficiale ha evidenziato un incremento del contenuto energetico delle vibrazioni indotte, dovuto ad un incremento dell'energia rilasciata dall'interazione di asperità più importanti,

inducendo impatti e rotture più energetici, e quindi inducendo un'ampiezza maggiore delle vibrazioni indotte (Figura 8).

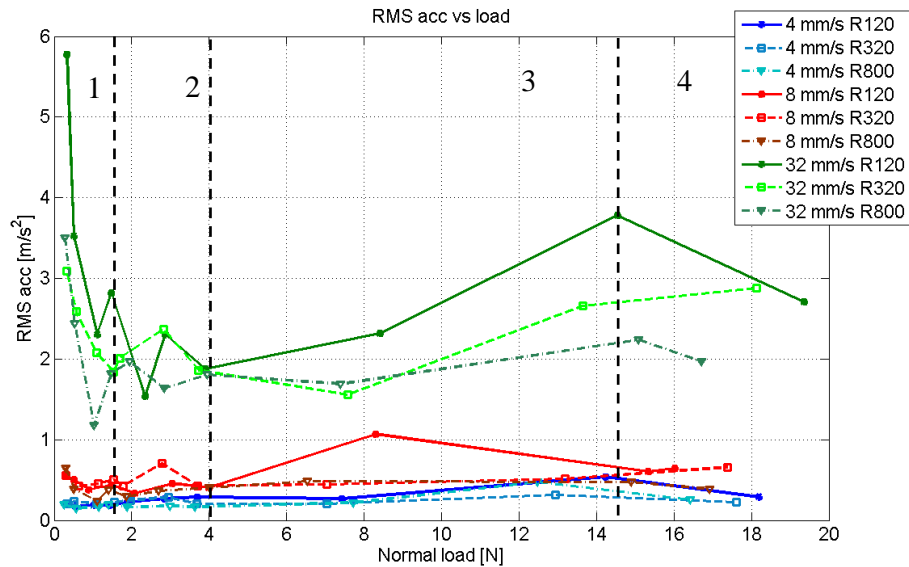


Figura 6: valor quadratico medio (RMS) dell'accelerazione vs carico normale, sovrapposizione dell'evoluzione delle tre rugosità e tre velocità di strisciamento: curve verdi relative a 32mm/s, rosse per 8mm/s, blu per 4mm/s

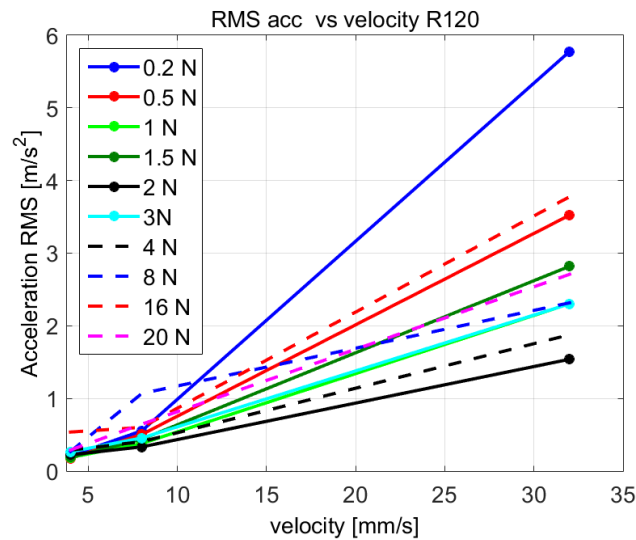


Figura 7: Valor quadratico medio (RMS) dell'accelerazione delle vibrazioni indotte vs velocità di strisciamento

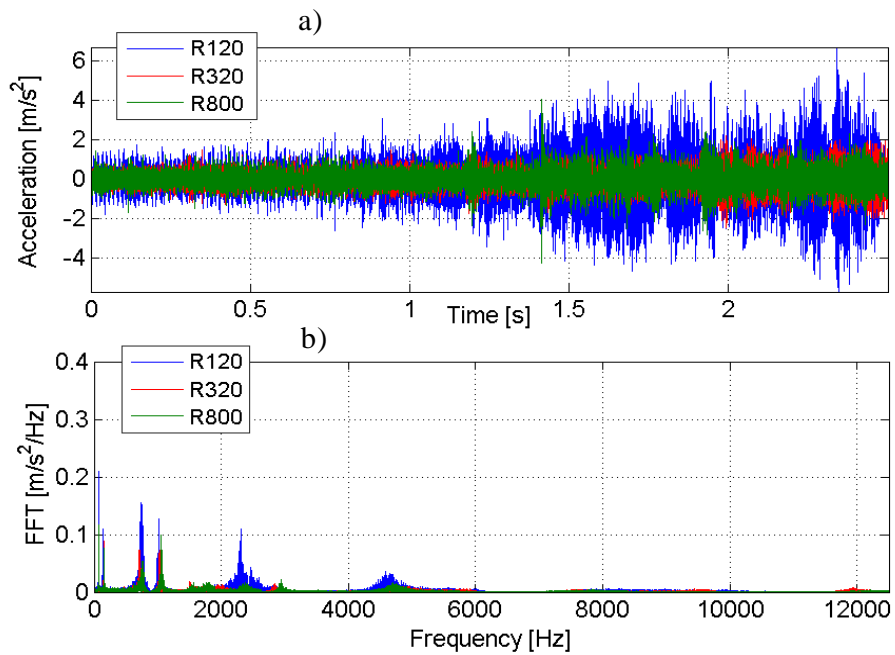


Figura 8: a) Sovrapposizione dell'evoluzione temporale dell'accelerazione per le tre rugosità; b) sovrapposizione della FFT dell'accelerazione, carico normale 8N, velocità di strisciamento 8 mm/s

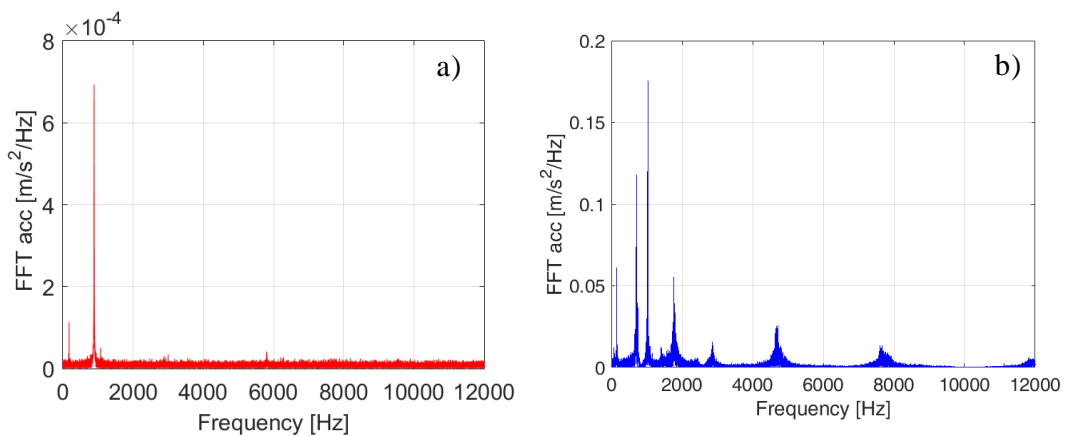


Figura 9: paragone fra l'evoluzione spettrale della FFT per l'accelerazione numerica (a) e sperimentale (b)

Analizzate le caratteristiche del sistema dinamico e delle vibrazioni indotte grazie alla campagna sperimentale, nel quarto e quinto capitolo viene descritto il modello numerico sviluppato per simulare le vibrazioni indotte ed in particolare l'eccitazione a larga banda del contatto.

È stato sviluppato un modello numerico bidimensionale, analizzato tramite il metodo agli elementi finiti (FEM); un'analisi preliminare agli autovalori

complessi è stata sviluppata per scegliere le dimensioni delle travi che evitassero l'insorgenza di instabilità dinamiche causate dall'accoppiamento modale. Definite le caratteristiche del modello numerico una prima analisi parametrica è stata svolta senza considerare la presenza dell'eccitazione dinamica al contatto, utilizzando la classica legge d'attrito di Coulomb, con un coefficiente d'attrito costante.

Paragonando i risultati numerici con quelli sperimentali, Figura 9, è emersa la necessità di introdurre la presenza dell'eccitazione a banda larga nel modello di contatto, per riprodurre correttamente le vibrazioni indotte durante lo strisciamento relativo.

La nuova legge d'attrito, introdotta nel modello numerico, usa un coefficiente d'attrito composto da due termini: un termine costante, come nella legge di Coulomb, ed un termine perturbativo, che vuole riprodurre l'eccitazione a banda larga generata dal contatto in presenza di attrito fra le due superfici (Eq.I).

$$\mu(x) = \mu_{const} + \mu_{perturbative} \quad \text{Eq. I}$$

Tre diverse distribuzioni spettrali sono state analizzate per riprodurre le vibrazioni indotte dall'attrito misurate durante la campagna sperimentale (Figura 10): un rumore bianco, un rumore bianco filtrato da un filtro Butterworth, ed una distribuzione calcolata dall'applicazione di un metodo inverso.

È stata studiata l'influenza delle differenti distribuzioni spettrali, introdotte nel termine perturbativo, sulla risposta dinamica del sistema; il segnale che riesce a riprodurre correttamente l'eccitazione al contatto è quello proveniente dal metodo inverso, evidenziando due contributi principali nello spettro dell'eccitazione:

- un primo contributo legato alla topografia della superficie, che si ritrova nella banda delle basse frequenze;
- un secondo contributo relativo alla natura impulsiva dell'eccitazione locale al contatto, generato da fenomeni quali rotture, impatti fra le asperità..., che determinano il contributo ad alta frequenza nell'eccitazione al contatto

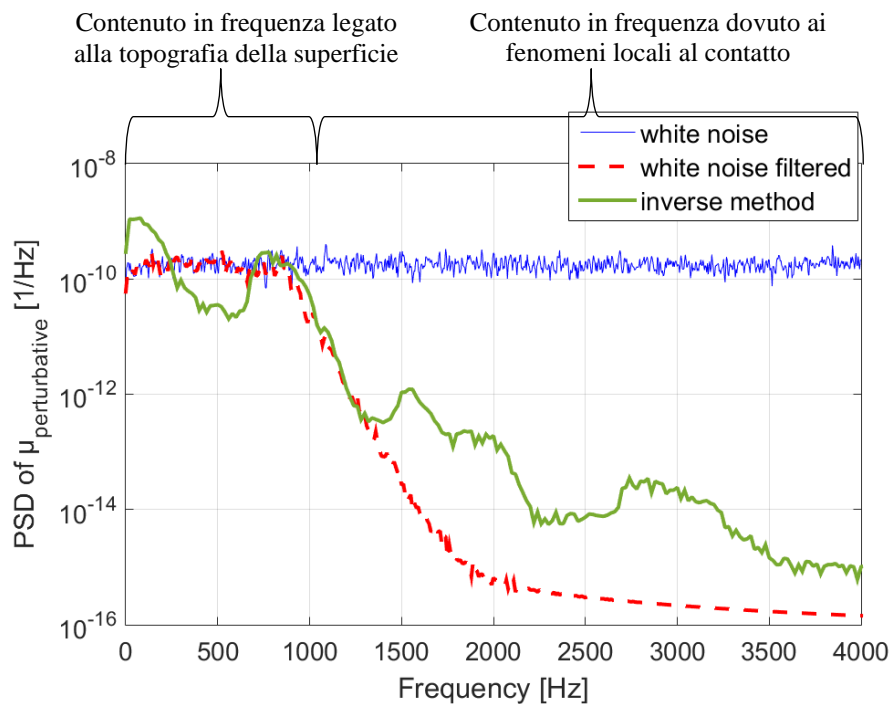


Figura 10: Sovrapposizione dell'evoluzione spettrale per i tre segnali testati per il termine $R(x)$: rumore bianco (blu), rumore bianco filtrato con filtro Butterworth (rosso tratteggiato), dal metodo inverso (verde)

La legge d'attrito proposta è stata quindi validata dal paragone fra i risultati numerici e sperimentali, presentando un'evoluzione dell'accelerazione numerica in accordo con quella misurata sperimentalmente (Figura 11 e Figura 12).

La nuova legge d'attrito è stata inoltre testata con due diverse rugosità superficiali e due diverse velocità di strisciamento, mostrando ancora una volta risultati numerici in accordo con gli andamenti sperimentali.

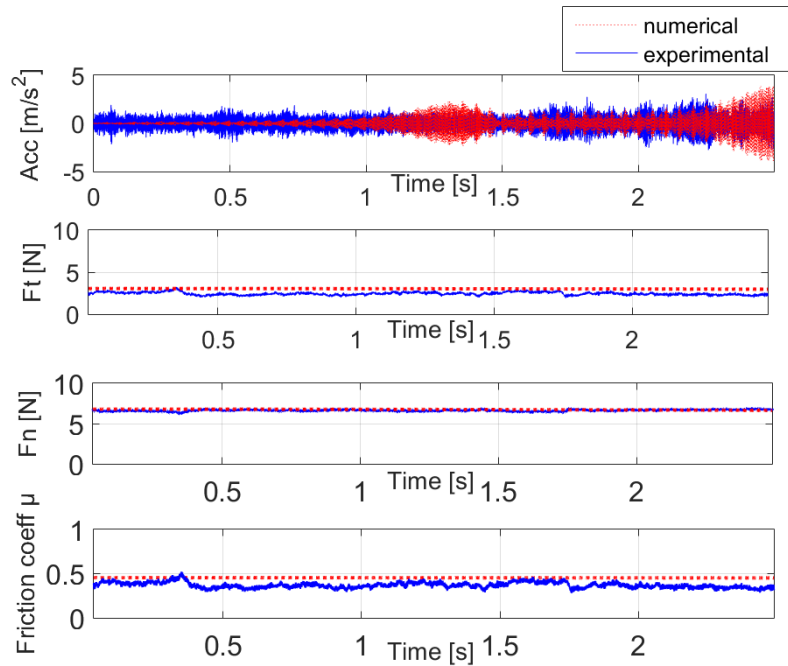


Figura 11: Evoluzione nel tempo numerica (rossa) e sperimentale (blu) dell'accelerazione e delle forze di contatto. Il segnale scelto per il termine $R(x)$ è calcolato tramite metodo inverso. Rugosità superficiale R320.

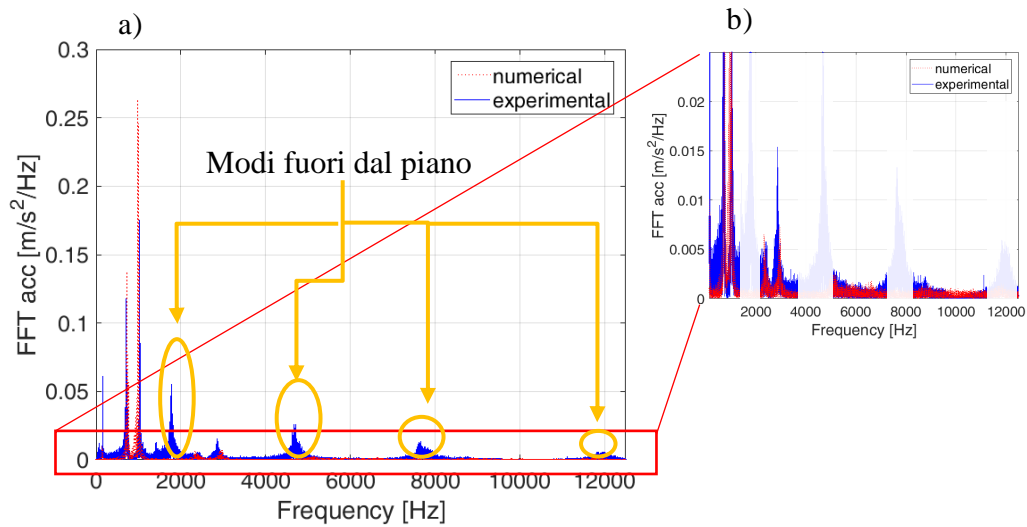


Figura 12: a) Sovrapposizione fra l'evoluzione numerica (rosso) e sperimentale (blu) della FFT dell'accelerazione; il segnale scelto per $R(x)$ è quello calcolato tramite metodo inverso; b) ingrandimento della FFT. Rugosità superficiale R320.

Concludendo, la legge d'attrito proposta è in grado di riprodurre correttamente le vibrazioni indotte dall'attrito senza introdurre una rappresentazione geometrica della reale topografia della superficie, che richiederebbe un numero elevato di elementi. L'introduzione dell'eccitazione dinamica, dovuta ai fenomeni locali al contatto, direttamente nel termine di perturbazione del coefficiente d'attrito ha permesso così di riprodurre le vibrazioni indotte dall'attrito senza aumentare i costi computazionali.

Abstract

Friction-Induced Vibrations (FIV) are a complex phenomenon which arises each time two surfaces undergo relative sliding. During the last decades, a significant amount of experimental and numerical works dealt with Friction-Induced Vibrations, while the simulation of the dynamic excitation from frictional contacts has always been a real challenge to face in many industrial research areas.

In this research framework, this work is addressed to the investigation of the Friction-Induced Vibrations, carrying on at the same time experimental and numerical analyses; a new numerical approach is proposed to reproduce the local dynamic excitation from the contact and its effect on the vibrational response of the system, without significant increase of the computational time costs.

The mechanical system, object of the investigation, is composed by two steel beams in frictional contact during relative motion; the simple dynamics of the system allows for distinguishing between the dynamics response of the system and the broadband excitation coming from the contact.

A parametrical experimental campaign has been conducted to analyse the effects of three main contact parameters (the relative sliding velocity, the normal load and the surface roughness) on the system vibrational response, i.e. on the induced vibrations. In parallel, a numerical model has been implemented to reproduce the local dynamic excitation from the contact and its effect on the vibrational response of the system. A new friction law has been introduced in the model, proposing the use of a perturbative term in the friction coefficient in order to simulate the effects of the contact excitation.

The inclusions of the local dynamic excitation, due to the contact phenomena, by the perturbation term of the friction coefficient allows to correctly reproduce the Friction-Induced Vibrations without introducing a representation of the real surface topography, which usually needs a large number of elements, saving then computational time.

Different signals for the perturbative term have been tested to simulate correctly the measured vibrations. The evolution of the perturbative term recovered by an inverse method allowed for highlighting the different spectral contributions of the local excitation coming from the contact.

The comparison between the measured Friction-Induced Vibrations and the ones simulated numerically showed good correlation, validating the proposed friction law. Finally, the effect in a change of the sliding velocity and surface roughness have been simulated numerically too and correlated with experimental results.

Keywords: Friction-Induced Vibrations, dry friction, friction law, contact dynamic

Summary

INTRODUCTION	1
I STATE OF ART ON FRICTION-INDUCED VIBRATIONS	3
I-1. Friction-Induced Vibrations (FIV)	5
I-2. Strong and weak contacts	9
I-2.1 Dynamic instabilities in strong contacts	10
I-2.2 Roughness noise in weak contacts	14
I-3. Dry contact mechanics with rough surfaces	16
I-3.1 Analytical models	16
I-3.2 Numerical models	19
I-4. Focus and positioning of the thesis	23
II MATERIALS AND METHODS.....	25
II-1. Analysis methodology	26
II-2. Experimental tools	27
II-2.1 TriboTouch test bench	27
II-2.2 TriboAir test bench	29
II-3. System and contact definition	31
II-4. Numerical tools	38
II-4.1 FEM modelling for system dynamic analysis (CEA)	38
II-4.2 FEM model for transient simulations (DTA)	42
II-4.3 Modified friction law	47
III EXPERIMENTAL ANALYSIS	51
III-1. Dynamics of the system	52
III-2. Reproduction of FIV	58
III-3. Parametrical analysis	62
III-3.1 Acceleration Root Mean Square (RMS)vs sliding velocity	62
III-3.2 Acceleration RMS vs normal load	63
III-3.3 Acceleration RMS and spectra vs surface roughness	67
III-4. Conclusions	70
IV NUMERICAL ANALYSIS	73
IV-1. System dynamics by eigenvalue analysis	74
IV-1.1 Complex eigenvalue analysis for system stability	75
IV-1.2 Updating of the clamping conditions.....	77
IV-2. Simulations without contact dynamic excitation	79
IV-2.1 Transient simulation of the sliding contact	79
IV-2.2 Parametrical analysis: comparison with the experimental results	83
IV-3. Conclusions	86
V NUMERICAL ANALYSIS WITH PERTURBATIVE FRICTION LAW	89
V-1. Determination of the perturbative term	90
V-2. Numerical results and experimental validation of the friction law	95
V-2.1 White noise	95
V-2.2 Butterworth filtered white noise	98
V-2.3 Signal retrieved from experiments by inverse method	100
V-3. Effect of contact and system parameters	104
V-3.1 Influence of surface roughness	104
V-3.2 Influence of sliding velocity	108
V-4. Effect of the boundary conditions and system dynamics	113

V-4.1	Stiffer boundary conditions and frequency shifting of the perturbative term	113
V-5.	Conclusions.....	119
VI	GENERAL CONCLUSIONS	121
VI-1.	Original contributions	122
VI-1.1	Experimental analysis	122
VI-1.2	Numerical analysis.....	124
VI-2.	Suggestions for future developments	126
	<u>BIBLIOGRAPHY</u>	129

Introduction

This work is placed in a research context at the bridge between dynamics and tribology. The term tribology derives from the composition of two Greek terms: the root “tribo” from the verb τριβω, with the meaning “I rub”, and the suffix λογία, which means “study of”. The term tribology was invented by Peter Jost in 1966 to indicate the research subject concerning contact, friction and wear. In the framework of the present work, it should be noted that friction means as well vibrations, which are generated at the contacting interface.

Friction and induced vibrations are phenomena that arise each time two bodies are put in contact and a motion is imposed. A force, opposite to the motion direction, rises and determines an action of resistance in either sticking or sliding conditions; at the same time, local phenomena at the interface (e.g. impacts and ruptures between asperities) induce wave propagations that result in vibrations. These phenomena happen in numerous and different contexts: from the everyday life (e.g. the simple action of walking is assured by the friction between the shoes and the ground), to mechanical applications (e.g. the case of brakes or blade dampers in turbomachinery). For this reason, friction and its consequences have been studied since hundreds of years; nevertheless, a general understanding of such phenomena is still missing and they are object of a countless amount of studies.

Considering the past and recent literature, while the analysis of friction as a source of resistant force has been deeply investigated, the friction interface as a source of vibrational energy, which is at the origin of several industrial and social issues, is becoming one of the emerging fields of investigation.

One of the main issues, concerning the analysis of the vibrations induced by the contact, is the multi-scale and multi-physics nature of the problem: faster time scale and smaller space scale are related to the contact interface, while slower and larger scales are related to the bodies and system dynamic response. Today, with the impressive rate of growth of technology, new possibilities for experimental investigation and numerical simulation are arisen, opening the path to new research works, which can deep into the multiscale nature of the contact problem. These works are developed in the framework of different disciplines, ranging from the molecular dynamics scale, to the scale of the mechanical systems (brakes, bearings, ...), up to the “scale of the Earth” for the study, for example, of earthquakes.

Into this manifold framework, this work focuses on the analysis of Friction-Induced Vibrations (FIVs). After the reproduction and analysis of FIVs on a

dedicated system, a new numerical approach enables to introduce the effect of the local dynamic excitation, coming from the contact interface, into the dynamic response of a frictional system has been proposed and validated.

First, to detail the subject of the work, Chapter 1 presents a review on the major works on friction and Friction-Induced Vibrations, as well as the connected general issues (dynamic instabilities and acoustic of friction). The contact models, proposed in the course of the time to describe the contact between rough surfaces, are then reported. In the same Chapter, the thesis work is positioned with respect to the literature.

Then, Chapter II describes how the problem has been approached. Then, the test-benches, employed during the experimental campaigns, are presented and the numerical model, developed to simulate the same phenomena observed in the measurements, is detailed. The new frictional law, with a perturbative term introduced for the simulation of the broadband contact excitation, is finally presented.

Chapter III describes the experimental campaigns carried on to characterize the response of the system under analysis. The results from the parametric experimental are presented, with focus on the effects of the different contact parameters on the Friction-Induced Vibrations.

Chapter IV illustrates the numerical simulations carried on to reproduce the frictional behaviour and the vibrational response of the frictional system in relative sliding. The classical modelling of the contact is adopted and a parametrical analysis is developed for comparing the results on Friction-Induced Vibrations with the experimental ones.

Chapter V presents the results of the simulations developed with the new friction law. The perturbative term of the friction law has been first object of the analysis. Then, the comparison between simulated and measured Friction-Induced Vibrations has been performed in order to validate the approach. Finally, the effects of some main parameters, such as sliding velocity and surface roughness, have been introduced by the proposed law.

Finally, Chapter VI outlines the main achieved results, presenting the concluding remarks and the future perspectives.

I State of Art on Friction-Induced Vibrations

Introduction

Leonardo da Vinci was the first scientist to report experiments about the friction phenomenon [1], carrying on experiences on axles' resistance and on the mechanics of screw threads. He discovered the two assumptions at the basis of Amontons-Coulomb friction theory, two centuries before Amontons: he stated that the frictional force is proportional to the normal imposed load and that it is independent from the contact area.

These fundamental concepts were discussed and reconsidered only in 1699 by Amontons [2], knowing today the law of friction force proportionality with the normal load as "Amontons law". After him, in 1750, Euler analyzed the difference between static and kinetic friction coefficients, proposing the "interlocking asperity theory" with the idea that the friction is caused by the interaction of surface asperities, schematized as triangular elements. Almost contemporary to Euler, Coulomb [3] carried on the first quantitative analysis of dry friction, discovering its dependence to materials, surface composition and temperature; he proposed also the law for which, in first approximation, the sliding friction is independent from the sliding velocity, concept deeply investigated steel nowadays, and criticized by Coulomb himself.

A century later, in 1882, Hertz [4] dealt with the evaluation of contact forces finding the solution, in term of contact stresses, for curved bodies in contact and his law is still adopted for approaching many contact problems.

The transition from the study of contact between smooth surfaces to the analysis of surface roughness happened in the middle of the twentieth century, when Bowden and Tabor [5, 6, 7] studied the importance of the presence of the surface roughness. They introduced a new approach for the triggering of the sliding friction, assuming that the friction between two metals is due to the touch and shearing of cold weld junctions. They also were able to distinguish the real contact area, made by the area of the asperities in contact, from the apparent contact area. Thanks to their work, a new current born into the field of tribology and other researches exploited their approach: Archard [8] demonstrated that the Amontons' law of proportionality between friction force and normal load is still reliable for highly elastic materials with contact between "many small protuberances". After him, several works focused on surface roughness, starting from Greenwood and Williamson [9], Bush [10] and nowadays with Persson [11].

It should be noticed that the recent theories on frictional contact assume the local interaction between asperities and local contact zones. It is clear that such local interaction will be at the origin of local phenomena, such as micro-impacts

between asperities [1] or local ruptures between local surface junctions, which are necessarily the source of wave generation and propagation [12, 13, 14] that will result in the so called Friction-Induced Vibrations

I-1. Friction-Induced Vibrations (FIV)

The mechanical systems subjected to friction are dissipative open systems [1]. Consequently, to introduce the phenomenon of Friction-Induced Vibrations, it is interesting to start with the different types of energy associated with friction.

In the literature, four main energy terms are often identified [12]: i) the first one is the energy used to deform or brake the boundary films placed at the contact interface; ii) the second one is the energy dissipated to deform elastically and plastically the contact asperities, causing fracture and wear; iii) the third one results in the interaction between the sliding bodies, allowing the generation of vibrational waves from the contact interface, propagating then to the surrounding elastic continuum; iv) the fourth term is due to the response of the continuum to the vibrational waves, generating a mutual influence between the local contact dynamics and the global system dynamics. Even if a more detailed energy description of the contact interfaces would include several other terms [13], already from this simplified description of the different energy terms, it can be argued that each time a frictional contact between two bodies occurs, vibrations occur too. In fact, the acoustic waves, generated at the contact interface, propagate into the bodies and induce the vibrational response of the bodies in contact, producing the so-called Friction-Induced Vibrations [14].

In this framework, the work carried on by Di Bartolomeo et al [14] reveals the presence of a mutual coupling between the local dynamics at the contact and the dynamics of the system. The acoustic waves, which arise at the local contact scale (from local ruptures and impacts at the interface), results in the vibrational response at the scale of the system dynamics. Waves of relevant magnitude propagate until the boundaries of the mechanical system components, generating the so called Friction-Induced Vibrations.

Because friction and FIV are strictly related each other, before focusing the attention on works dealing with FIV, some main works dealing with friction are reported in the following.

The work from Ibrahim [15] depicts the manifold nature of friction, describing the contact mechanics and the influence of contact parameters on friction: material, sliding velocity, normal load, time of contact and temperature are taken

as contact parameters and their effect into the friction force(s) are described. Starting to analyse the effects of the chosen material, two main groups have been identified: the first group is composed by the antifriction materials with a low coefficient of friction and high wear resistance; the second group is characterized by materials with a high coefficient of friction. From this division, he distinguished the mechanics of contact in two classes: the metal-metal contact (high friction coefficient) and the contact between soft elastomers (antifriction materials such as rubber) and hard surfaces (metals). In his work, for the metal-metal case, the friction force is considered to be composed by two terms: the first one, due to the stress that is needed to shear the metallic junctions between the asperities; the second one, which concerns the ploughing force required to displace the softer metal from the path of the harder one [16]. For the metal-elastomer, instead, the friction contact force is generated by the sum of the adhesive force (due to the molecular bonding) and the so-called *hysteresis force*, which allows the elastomer to recover its deformation after the contact. Moreover, at low sliding speeds, for metal-elastomer contact, a stationary state is established and in this condition friction is the result of two opposite phenomena: infinitesimal adhesive dragging and a continuous relaxation process. Considering his observations, it is clear that the local phenomena such as “dragging, adhesion or relaxation processes” must be necessarily followed by wave propagation, due to the local release of energy.

Another main contact parameter is the relative sliding velocity. Considering lubricated contacts, several studies focus on the relation between friction and sliding speed, starting from the three classical friction-speed models proposed by Armstrong-Hélouvy [17], which identify three different behaviours.

The three models propose an evolution of the friction force that increases with the increase in the sliding velocity (Fig. I-1). Another model showing the dependence of friction force from the sliding velocity for lubricated contacts is the Stribeck model [17] (Fig. I-2).

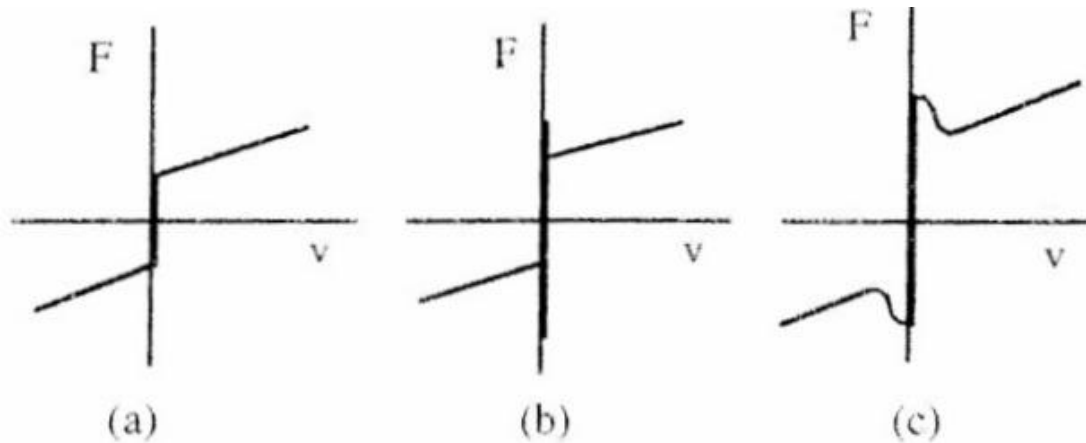


Fig. I-1: Armstrong-Hélouvy friction-speed models: a) kinetic+viscous; b) static+kinetic+viscous; c) negative viscous+kinetic+viscous [17]

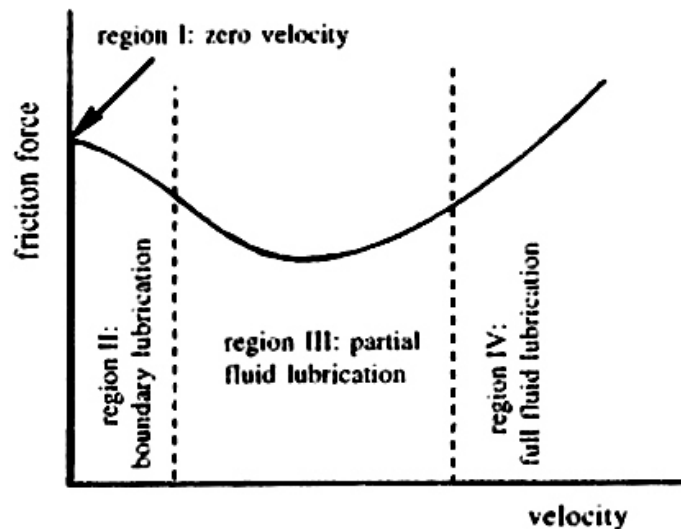


Fig. I-2: Stribeck curve for the evolution of friction with speed in lubricated contacts [17]

In Fig. I-2, increasing the velocity, four regimes are shown: i) the first one is the static-friction state, which obviously doesn't depend on velocity (region I at zero velocity); ii) the second region is the boundary lubrication zone, which is still not affected by the lubricant pressure to separate the surfaces and the load is mainly carried by the contact between asperities; iii) the third regime is characterized by the partial fluid lubrication; iv) the last region is the full fluid lubrication zone, where finally the contact surfaces are completely separated.

Considering FIV in lubricated contacts, it is clear that the more the contact between asperities occurs, the more acoustic waves are generated at the interface.

Consequently, mechanical systems working in full fluid lubrication regime are less affected by the FIV and the issues relative to Friction-Induced Vibrations become relevant when dealing with dry friction. Nevertheless, under specific conditions, the dynamic response of the fluid-structure system can bring to severe vibrational instabilities too.

Focusing on dry friction, Sampson [18] determined a multi-valued friction, which increases with sliding velocity within a small velocity range. Again, the cause of the initial increasing evolution is, in his opinion, due to the creep deformation of the interface asperities. On the contrary, several works [19, 20, 21, 22] showed the aptitude of different material to decrease the overall frictional force with respect to the sliding speed. Moreover, such trend is at the basis of several contact models used in nonlinear system dynamics to reproduce unstable contact-induced vibrations. Nevertheless, it should be kept in mind that such models wish to give a lumped (macroscopic) representation of the mechanical system, neglecting the local phenomena at the interface on the FIV and the system dynamic response.

Another main contact parameter is the normal load. Numerous studies [6, 23, 24] showed that the friction coefficient decreases as the normal load increases if all the other contact parameters are maintained constant. A study conducted in 1990 by Dweib and D'Souza [25] proposed a peculiar evolution of the friction force with the normal load (Fig. I-3). The study was conducted carrying on experimental tests with a pin-on-disk apparatus, maintaining constant the sliding speed. Four regimes can be distinguished, starting from the initial linear phase, passing through the nonlinear region and the transient region, until the last region, characterized by self-excited vibrations for high loads. In this last region a drop in the friction force value is registered and high-amplitude periodic self-excited oscillations arise. The same works showed that, in the region of self-excited vibrations, an increasing in the level of the normal load caused the transition from stable to unstable sliding motion, due to the coupling between the degrees of freedom, as it will be better explained in the following sections.

The work from Dweib and D'Souza is an example of the strong coupling between friction and vibrations induced by friction. In their work, they started to characterize a “friction regime” by the appearance of unstable friction-induced vibrations.

In fact, as a function of the contact parameters, the quota part of frictional energy converted in induced vibrations can give rise to either stable or unstable dynamic response of the mechanical system, resulting in either friction noise or self-excited vibrations.

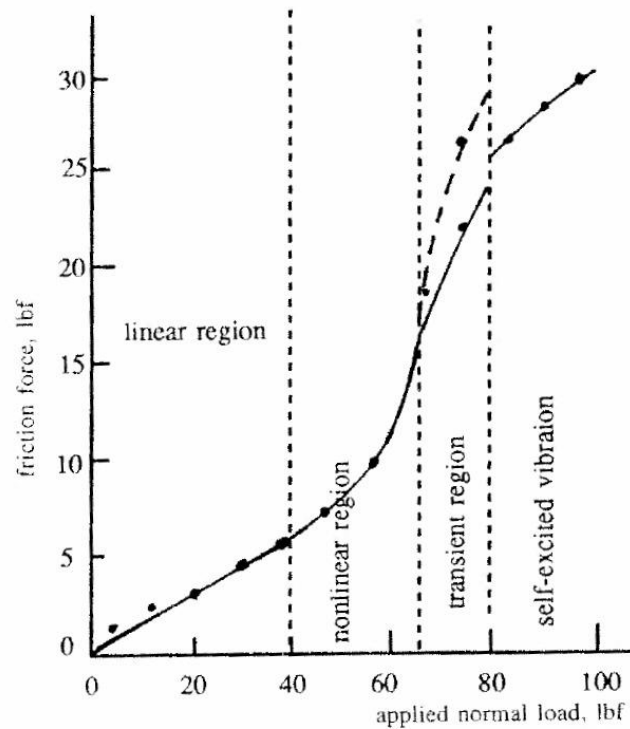


Fig. I-3. Evolution of mean friction force with the increasing of the applied normal load [25]

Considering the contact load, the next section focuses on these different “vibrational behaviors” of the frictional system, starting from the differentiation between strong and weak contacts proposed into the literature.

I-2. Strong and weak contacts

When dealing with Friction-Induced Vibrations and the vibrational response of two bodies in contact, several classifications and names have been proposed to discriminate between dissimilar behaviours. Classifications have been proposed as a function of the stability of the dynamic response (stable or auto-excited vibrations) [26], as a function of the frequency range (groan, squeal, ...) [27], or as a function of the macroscopic frictional behavior (stable sliding, stick-slip, harmonic oscillations) [28]. Nevertheless, because of the wideness of the concerned issues and the complex behaviour of FIV as a function of several parameters, a general classification is difficult to be defined.

The most general classification that can be found in literature [26, 27] has been proposed with respect to the “degree of coupling” between the two substructures

in frictional contact. With respect to such classification, two bodies in sliding contact can be characterized by two different conditions: either *weak contact* or *strong contact*.

The *weak contact* condition allows to consider the two subsystems as independent, treating the interface as an external boundary to each one; in this case the impacts between the surface asperities generate the vibration waves, which propagate in each body exciting their own eigenfrequencies, nearly independent from each other. The interaction of the surface roughness, under weak contact conditions, produces the so-called roughness noise or surface noise [27], which has been identified as a random sound with low power and a spectrum within a broadband frequency range, characterized by the presence of peaks at the body eigenfrequencies.

The *strong contact* condition rises instead when the contact force between the bodies is higher and they cannot be considered independent anymore [27]; the bodies become a coupled system and the sliding interface has to be considered as an internal boundary condition. In this condition, dynamic instabilities can develop and specific vibrational states can be generated, such as the mode lock-in instability or the macroscopic stick-slip instability [29].

However, this definition is not absolute and, for a system with given sliding velocity and contact surface geometry, the weak contact can module into strong contact if the normal contact load is increased.

Even if the literature dealing with friction-induced vibrations, and mainly with contact instabilities, cannot be completely reported in this context, in the following sub-paragraphs the main works dealing with both strong and weak contact conditions are summarized. First, a summary of the literature dealing with instabilities during strong contact conditions is reported; then the main works dealing with the roughness noise are presented.

I-2.1 Dynamic instabilities in strong contacts

As stated before, a change of the contact conditions between two bodies in relative sliding motion can bring to peculiar dynamic states, called dynamic instabilities, during which strong oscillations or abrupt motions can appear [30], coupled with characteristic noises and severe wear. This condition can be annoying (noise) and dangerous (wear and vibrations) for the mechanical components and a relevant amount of works have dealt with the analysis of such dynamic contact instabilities. Here a simple path between the main works is traced.

Actually, dynamic instabilities can be grouped in three main families, with respect of the macroscopic dynamic response of the system: stick-slip, sprag-slip and modal coupling.

Starting with stick-slip, Ibrahim asserted that this phenomenon is characterized by two phases [28]: the first one is elastic, when the two contact surfaces stick and the asperities deform elastically; the second one is plastic, when sliding motion occurs and the asperities deform plastically. These two consecutive phases cause a macroscopic intermittent motion that has been called stick-slip. Its rising, in the course of the time, has been attributed to different causes: difference between static and kinetic friction coefficients [31], decrease of kinetic friction coefficient with sliding velocity [32] or variation of friction coefficient along the sliding surfaces, wave generation and propagation at the contact interface [33, 34].

The first observation of the stick-slip phenomenon was reported by Wells [35]. He noticed a discontinuous motion during the measurement of the kinetic friction coefficient. After him, Den Hartog [36] proposed an exact solution for steady state stick-slip motion for a single-degree-of-freedom with two intervals of lockup per cycle. Following this work, ten years later, Blok [37] stated that the essential condition for the rising of stick-slip condition is the decrease of frictional force with the increasing sliding speed. He showed as well that an increasing in the damping can cause the elimination of the phenomenon. Continuing to study the dependence of stick-slip from the sliding speed, Derjagin [38] found a mathematical expression for the critical speed at which stick-slip occurs. Several studies during the 20th century demonstrated that the stick-slip motion arises also for cases with a speed-independent friction coefficient and the cause of instability is the presence of interfacial stick-slip waves. Adams [39] demonstrated that contact waves can propagate at the interface and generate local sliding conditions different from the global observed ones; besides, the apparent coefficient of friction (macroscopic) can be lower than the local friction coefficient. Moreover, the apparent friction coefficient can decrease with increasing speed, even if the interface friction coefficient is speed-independent. Di Bartolomeo et al [14] showed how the local dynamics at the contact, i.e. the contact wave generation and propagation, drive the macroscopic stick-slip unstable vibrations.

This brief overview highlights that the stick-slip phenomenon has a complex nature, influenced by several parameters, and the causes of its occurrence are still nowadays object of investigations.

When the elastic deformation of the mechanical system affects largely the contact loading, the sprag-slip condition can occur. Spurr studied the sprag-slip

phenomenon [40], associating it with brake-squeal. The unstable vibrations are caused by the interactions between the different degrees-of-freedom of two subsystems in relative sliding (the system analysed was composed by a moving plate on which a rigid rod slides). The coupling between the degrees-of-freedom (caused by a geometrical deformation of the system for the case analysed by Spurr [40]) determines a variation on the normal contact force, and then a variation on the friction force.

One of the first works on brake squeal was carried on by Mills [41] in 1938. Brake squeal is one of the most evident problems of dynamic instabilities into mechanical applications. Squeal is the noise that can be produced when a braking system comes into operation. North [42] studied the friction instabilities caused by the coalescence of two eigenvalues; due to a change in the system parameter, the initially separated eigenvalues have an approaching evolution until the point of *lock-in* [43]. The mode coupling instability rises when there is the coalescence of two system modes. The eigenvalues assume the same imaginary part and the real parts diverge. A positive sign in the real part produces the flutter instability, which is in this case called mode coupling instability [43].

Several unstable vibrations recovered in applicative issues, such as brake [42, 44, 45] or hip endoprosthesis squeaking [46, 47], can be attributed to the mode coupling instabilities. The deep interest into this issue, from an industrial point of view, generated an important amount of works dealing with mode coupling instability, with both experimental and numerical analyses. Among them, the work of Hoffmann [48] investigates from a qualitative and quantitative point of view the mode-coupling instability. A two-degrees-of-freedom model is analyzed and a complex eigenvalue analysis is carried on. His work showed that an increase in structural damping can provoke a transition of the system response from unstable to stable.

Also the work of Sinou and Jèzèquel [49] deals with the effects of damping on mode-coupling instabilities. They proposed a two-degrees-of-freedom system and they studied the evolution of the Hopf bifurcation point as function of structural damping and other system parameters. They showed that an optimal structural damping ratio exists, which determines the transition between stable and unstable modes.

Among numerous works [50, 51, 52], Massi et al [53, 54] and Brunetti et al [55] investigated squeal instabilities on a simplified disc-brake system, both experimentally [54] and numerically [53]. The lock-in instability is reproduced by a parametrical analysis, showing that the system changes condition from stable to unstable. In [56], a balance of the energy flux between the contact interface and

the system has been developed to quantify the energy absorbed by the unstable vibrations and define indexes able to predict the system instabilities. Considering noises coming from contact dynamic instabilities, the acoustic waves, which result from the unstable vibrations during stick-slip or mode coupling instabilities, can often determine a radiation of sound to the surrounding media [27]. For instance, the sound of brake squeal is only one of the numerous sounds which belong to the so-called *brake noise*. While the braking action converts most of the kinetic energy of a vehicle into thermal energy, there is also a quota part of energy that results in sound radiation. The different brake sound noises have different names according to their spectral content (Fig. I-4).

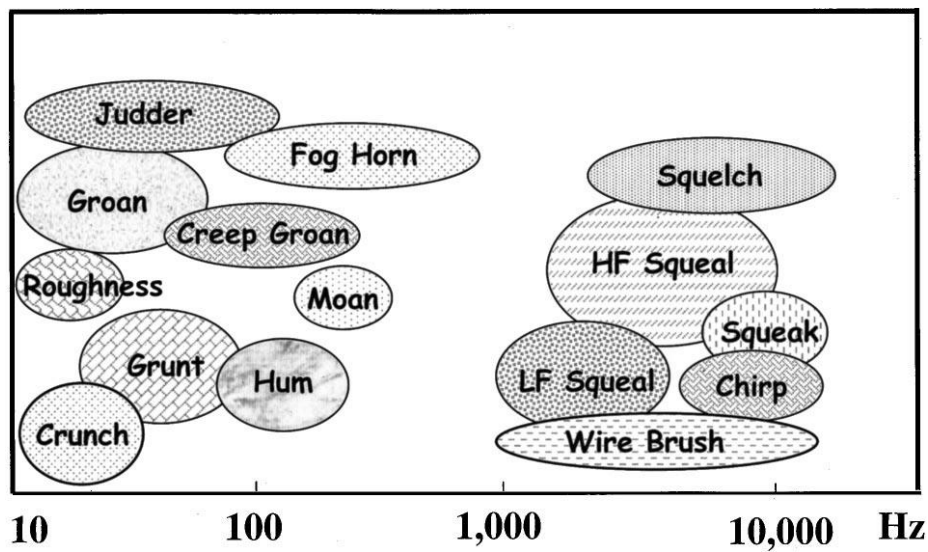


Fig. I-4: Brake noises and their spectral content [27]

A recent work on dynamic instabilities [57] analysed both stick-slip and mode coupling phenomena, focusing on the effects of material damping. In this work, a variation in the damping coefficients is analysed and the macroscopic frictional behaviour in term of tangential and normal contact forces is studied. Testing low damping values, the forces present a discontinuous behaviour characterizing a stick-slip instability; increasing the damping, instead, a stable condition of sliding is reached, passing by another unstable state characterized by harmonic mode coupling vibrations. Related works [58] showed, experimentally and numerically, how any frictional system can pass from a stable vibrational response to an unstable one, characterized by either a macroscopic stick-slip or mode coupling dynamic unstable behaviour.

As mentioned above, the works dealing with contact vibrational instabilities are uncountable. For a more deep look on the different works, the reader can refer to the several review papers on the subject [15, 22, 27, 30, 44].

I-2.2 Roughness noise in weak contacts

While strong contacts result often in contact instabilities and the following system unstable vibrations, a stable vibrational response of the mechanical system can be excited by either strong and weak contacts. Abdelounis et al [59] conducted several studies focusing on the parameters that influence and change the noise produced by a frictional interface. The studies are carried on under *weak contact* conditions. He affirms that for sliding rough surfaces under light load the fundamental mechanism of noise radiation, called *roughness noise*, is due to the impacts between asperities of the sliding surfaces.

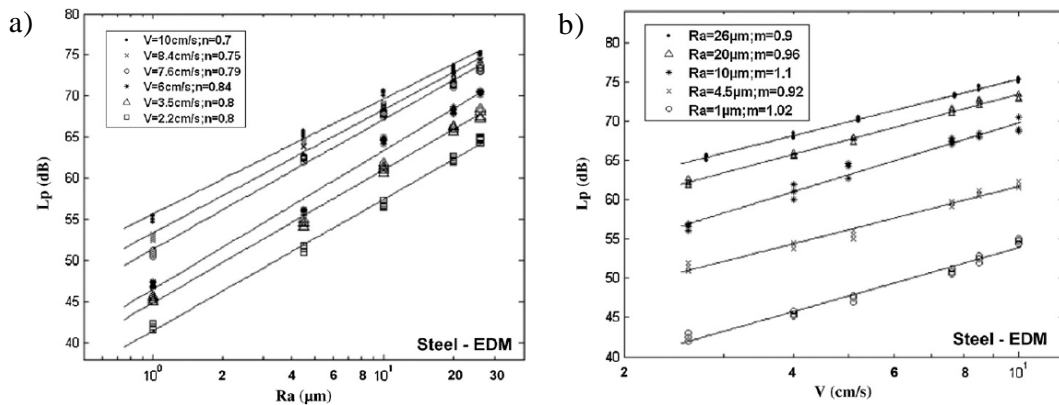


Fig. I-5: a) Evolution of the sound pressure level L_p (dB) with the surface roughness for various sliding speeds; b) Evolution of the sound pressure level L_p (dB) with the sliding speed for various surface roughness [60]

He showed, thanks to an experimental set-up made of two sliding samples with rough surfaces, an anechoic chamber and an accelerometer, that the sound pressure level L_p (dB) is proportional to the roughness and to the sliding velocity. Fig. I-5 shows the evolution of the radiated acoustic power with respect to the increasing of surface roughness (left figure) and sliding velocity (right figure). An increasing in surface roughness or sliding velocity causes an increasing in sound emission; thus, a sample that slides with high velocity and a rough contact surface showed more vibrational energy than a sample with smooth surface and low sliding velocity.

Another work from Le Bot and Bou-Chakra [60] values the dynamic and acoustic response of a specimen rubbing on a plate. During the tests, the surface roughness is changed, while normal load and sliding velocity are maintained constant. The work highlighted that there are two regimes in the dynamic response: one with the vibrational energy proportional to the effective contact area; the other one with a constant level of the vibrational energy. The two regimes are determined by the internal damping of the samples: a reverberant resonator tends to a regime with constant vibrational level; a damped resonator behaves in a regime with a vibrational energy proportional to the number of sliders. The vibrational energy is evaluated in their work by means of the radiated acoustic power, measured with the RMS vibrational velocity. It should be remarked then, that the measure overlaps the noise directly coming from the surface with the vibrational response of the solids in contact.

Continuing to analyse the effects of contact conditions on the sound radiated from two sliding surfaces, a work carried on by Otham, Elkholy and Seireg [61] presents an experimental study with a stylus sliding over a frictional surface, when testing different materials. The relation between the sound pressure level and the surface roughness has been established with different normal loads. This experience showed the presence of a frequency, called “dominant frequency”, in the SPL (sound pressure level) that was linked by the authors to the specimen material and it is proportional to the sonic speed in the material.

It should be noticed that the amount of literature dealing directly with stable contact vibrations and roughness noise is exiguous with respect to contact instabilities. In fact, when dealing with Friction-Induced Vibrations, the interest in specific industrial problems drove the focus of the researches on unstable vibrations. Nevertheless, the renewed general interest on the vibrational response of mechanical systems with frictional contact, and the need to model and simulate the frictional contacts in a more and more precise way, brings now the attention to the analysis and modelling of the roughness noise and the stable vibrational response of the frictional system. In this direction, a main issue is represented by the modelling of the surface roughness, in order to account for the local interactions between asperities.

In this context, the following section presents a review of the contact models, proposed in the course of the time, that try to introduce the modelling of the surface roughness between two surfaces in contact.

I-3. Dry contact mechanics with rough surfaces

A general view on the different approaches developed to simulate numerically dry frictional contacts is given by the work of Renouf et al [62], where three main groups of different approaches have been distinguished: analytical, semi-analytical and numerical approaches.

When dealing with vibrations induced by a frictional interface, the surface roughness is one of the most important parameter, whose effects on the system vibrational response are difficult to be evaluated. Its definition is indeed fundamental to simulate with accuracy the dynamic response of frictional systems. This section has the objective to trace a path in the evolution of the contact models, starting from the first analytical attempt to simulate a contact between two asperities, until the more recent numerical models with geometrical representation of the surface topography. In this context the challenge is to reach an accurate simulation of the effect of the contact interface, maintaining at the same time reasonable computational costs. The leitmotiv of the proposed models has then been always the balance between an accurate description of the contact and sustainable computational costs. Considering that such models are often restricted to static simulations, it should be kept in mind that the computational costs for executing transient simulations, needed for reproducing FIVs, are unacceptable in most of the cases.

The section is divided in two parts: the first one deals with the analytical models, while the second part concerns the numerical models, widespread with the improvement of numerical codes and computational power.

I-3.1 Analytical models

One of the main effect to take into account when introducing the surface roughness in contact models is the real contact area. In fact, in presence of rough surface, the *real contact area* has to be distinguished from the *apparent contact area* [63]. The contact indeed happens between the peaks of the roughness asperities. It occurs then at localized contact zones, called *junctions*. The real contact area is composed by the sum of the areas of the contact junctions and it is a small fraction of the apparent contact area. Fig. I-6 shows two bodies in contact with the difference between the apparent contact area A_a and the real one A_r .

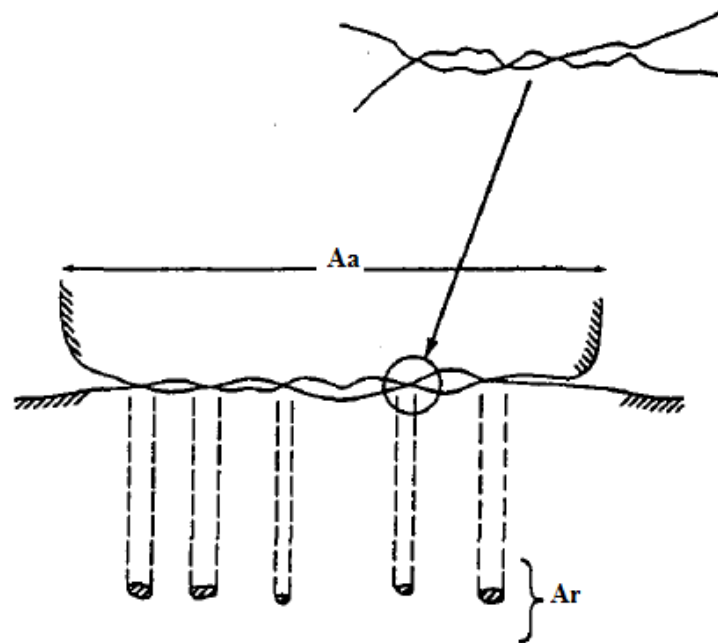


Fig. I-6: Representation of two bodies in contact with a rough surface. A_r indicates the real contact area, A_a the apparent contact area [63].

The real area of contact is of great interest for its influence in the phenomena of friction, wear and induced vibrations. The first study on surface roughness and real contact area date back to 1950, with Bowden and Tabor [5]. Few years later Archard [64] proposed a contact model composed by a flat surface in contact with a flat surface covered with spherical protuberances to pass from the apparent contact area (singular contact) to multiple areas of contact (real area). The same author [8] stated that the Hertzian theory is not able to predict the proportionality between the contact area and the load, which had been instead observed experimentally. He introduced also a fundamental issue into the contact model: an increase in load creates new contact areas or increase the size of the existing ones?

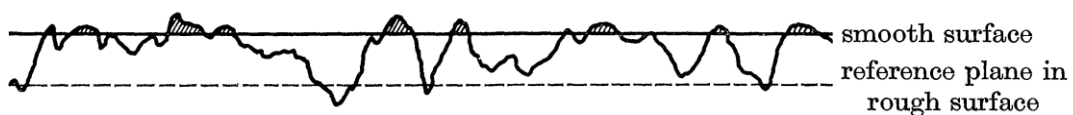


Fig. I-7: Greenwood and Williamson model: smooth surface in contact with a rough surface [9]

Greenwood and Williamson [9] proposed a first answer to the question. They proposed a 2D model of bodies in contact, where the contact occurs between a

plane and a nominally flat surface covered with asperities with spherical summits, Fig. I-7.

The surface profile is characterized by a normal distribution of summits with the same radius. They calculated the total area of contact and the total load starting from the Hertzian equation [65], valid for a single asperity. Then, they introduced the probability of contact from the knowledge of the asperity height and the initial distance between the bodies to determine the expected number of contact junctions. They finally demonstrated that the average size of contact spots and the contact pressure are independent from the load imposed to the body. The size of each contact spot, indeed, increases with load and at the same time small spots are formed in a balance that leaves the average unchanged.

Within the path of the models that consider a multi-asperities contact distribution, after Greenwood and Williamson, other analytical models were proposed, showing a more accurate description of the roughness surfaces [66]. Whitehouse and Archard [67] considered the surface roughness as an array of asperities with a statistical distribution on both heights and curvatures. Onions and Archard [68] proposed a Gaussian distribution of surface heights and asperity peak curvature, instead of a distribution of the asperity heights.

After them, Nayak [69] introduced a contact model with random surfaces characterized by three spectral moments of the profile, equivalent to the variances of the distribution of profile heights, slopes, and curvatures.

Bush [10] exploited the work of Nayak [69] to develop an elastic contact model with asperities characterized by an elliptical paraboloid shape with random principal axis orientation and aspect ratio.

A more sophisticated model by Majumdar et al [70] proposes a fractal characterization of the surface, with the exploitation of the Weierstrass-Mandelbrot [71, 72] fractal function.

A main remark to keep in mind is that all the cited analytical models are *static* models. They can estimate only the value of some contact parameters, such as the contact forces, contact pressure, real, apparent and nominal areas, but they do not investigate the dynamic excitation from the surface roughness and the corresponding response of the system. On the contrary, to have realistic representation of the source of FIVs, all the transient phenomena taking place between asperities, and/or third body particles [73, 74], should account for. To study the evolution of the system during the time, some numerical models have been proposed in the recent literature, in order to simulate the sliding motion of two rough surface.

I-3.2 Numerical models

During the last decades, with the abrupt development of the technology and the consequent growth of the computational capabilities, a relevant number of numerical models have been addressed to the transient simulation of contact problems.

In this section, only the friction models that account for the surface roughness will be described in order to have a sight on the major approaches in the simulation of surface roughness and compare them with the approach proposed in this work.

A classification of the numerical models is proposed by distinguishing two main approaches:

- models that reproduce the surface topography, with the geometrical reproduction of the asperity distribution [75, 76, 77, 78, 79, 80];
- models which define specific contact algorithms [81, 82, 83, 84].

Starting with the models that describe the topography of the surface roughness, Bengisu and Akay [76] considered in their model the deformation and the adhesion between surface asperities. They built a numerical model with two nominally flat surfaces in contact. The surface roughness is described by a probabilistic model and the roughness distributions of the two surfaces are considered independent. The considered dynamic system is a simple rigid block with deformable surface asperities connected to a linear spring and a viscous damping element; the block is in contact with a flat platform which moves at constant speed $v(t)$ (Fig. I-8).

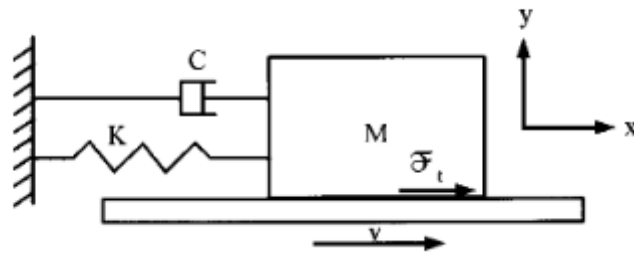


Fig. I-8: Dynamic system used by Bengisu and Akay [76]

The local friction forces are analysed and, extending the expression of the normal and tangential friction forces over the macroscopic surfaces, the model is able to determine the condition of stick-slip. The work highlighted how friction depends both on the local properties of the interface and on the dynamic response of the

system, relating macro-scale friction force to micro-scale forces developed at the true contact area.

Slavic et al [77] studied the dynamics of a ball impacting on a rough surface, the case of the paddle juggling, exploiting the Poisson impact law and the Coulomb friction law. They investigated the response of the system considering three cases: an impact with one contact point, two contacts points and impact with rough surfaces.

The surface roughness of the impact surface was defined by 10000 contact points with 22 μm between adjacent points. The comparison between the numerical results and the closed-form solutions gave good agreement with the experimental results.

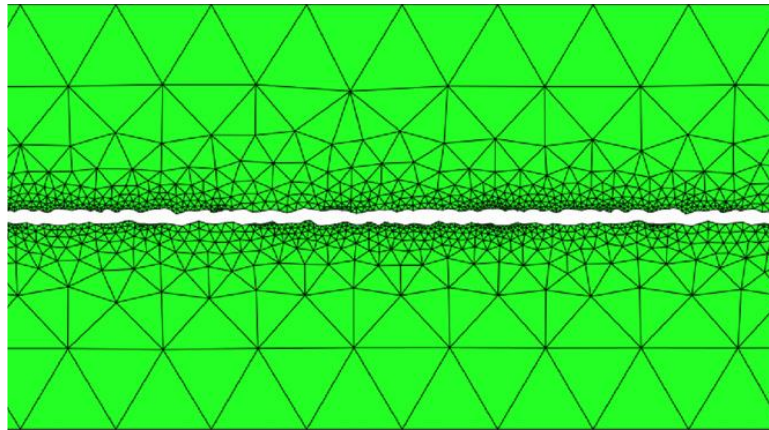


Fig. I-9: Mesh utilized in the contact model proposed by Abdelounis et al [76]

The work of Abdelounis et al [75] focuses instead on the friction noise radiated from the rubbing of two rough surfaces. The finite element method was exploited to simulate the roughness noise, utilizing the Coulomb friction law at the contact interface. A topographic analysis was carried out to determine the distribution of the asperities. With the surface parameters, i.e. the arithmetic surface roughness R_a , Skewness, Kurtosis and standard deviation of the height distributions of asperities [85], the roughness of the surface was completely described.

Fig. I-9 shows the mesh used in the model, with a refinement on the contact surface, where 7764 triangular 2D plain strain elements have been used. This simulation was able to determine the local contact forces and stresses, the number of impacts and their intensities, from which the authors deduced the roughness noise level.

The works carried on by Yastrebov et al. [78] proposed two approaches for the frictionless contact between an elastoplastic material and a rigid plane. The results

from a full scale finite element analysis (FEA) were compared with a reduced model. For both the models the surface roughness was described with a representative surface element, built from a measured surface roughness. The used mesh for the FEA was composed by 105625 nodes. Moreover, a reduced model was proposed. It was based on the representation of each asperity by an element with a force-displacement behaviour derived from the previous FEA analysis of one single asperity. With the reduced model the CPU time was severely reduced. The reduced model had a good agreement with the FEA model, but it could be utilized only for soft materials in contact with rigid bodies; the extension to the case of metal-metal contact is not trivial.

The models discussed above tried to simulate the contact dynamic in presence of surface roughness looking for the best surface representation of the experimental surfaces, but they are in general characterized by a high computational cost, due to the wish of reproducing the real topography of the surfaces. Consequently, they cannot simulate a complete transient response on complex systems with real geometries and for representative time periods.

To overcome this problem, the second family of models proposes friction models with peculiar contact algorithms to be introduced at the contact interface.

The work of Sellegren and Olofsson [84] introduces a micro-slip friction law based on the asperity deformation and able of simulating the oscillations of the friction force. The friction law introduces a friction coefficient μ that depends on the shear modulus, the elastic modulus, the penetration and the tangential sliding displacement. The penetration is found in function of the contact pressure and changes with the characteristics of the contact surface, including the roughness. The friction law has been implemented into the FEM software ANSYS. The results highlighted that the use of a simple Coulomb elastic model could underestimate a large part of the energy dissipated by the contact.

A recent work of Lundberg et al [83] utilizes a state-dependent method to model the contact nonlinearities. In their work *state-dependent* means that the contact conditions depend on the vertical relative displacement. The considered contact system is composed by a steel ball rolling over a steel beam. Two fundamentals parameters are introduced: K_c , the state-dependent contact stiffness, and h , the state-dependent gap value between the two bodies. The global stiffness at the contact interface is calculated as the average of N stiffness obtained from N surface zones. For the time domain model a line of texture heights, measured from experimental tests, is requested. The behaviour of the beam was modelled with the Euler-Bernoulli theory. Once the contact stiffness was calculated, it was included in a nonlinear point force expression, which was a part of the time-

domain model. With this approach, the dynamic interaction is determined by the coupling of a linear dynamic model with a nonlinear point force expression. Experimental tests of a rolling ball on a steel beam have been carried on and showed good correspondence with the numerical results.

Another approach was proposed by the work of Cabboi et al [86], where the introduced friction model is based on the exploitation of a rate-and-state model [32], which defines a friction law as in Eq.1.1

$$F = N\mu = N[\mu_* + a \ln(v/V_*) + b \ln(\varphi/\varphi_*)]$$

Eq.1.1

where v is the slip rate at the frictional interface, the “*” indicates the reference values of the variables, a and b are dimensionless parameters that quantify the rate-and-state deviation from the Coulomb law, and φ is an internal state that represents the measure of the slip resistance at the frictional interface.

Eq.1.1 can be seen as a relaxed Coulomb law, which can allow nonlinear relation between the friction force F and the normal force N .

Starting from the rate-state model, their work introduces a Fourier transform of the friction force, reducing Eq.1.1 into Eq.1.2:

$$\begin{aligned} F &= F_0 + F' e^{j\omega t} \\ F' &= \beta(\omega) v'(\omega) \end{aligned} \quad \text{Eq. 1.2}$$

The friction force F is composed by two terms, a reference term F_0 and a term of perturbation F' . The term of perturbation is proportional to the perturbed speed v' by the mean of $\beta(\omega)$. $\beta(\omega)$ is a general complex number that represents a linearized frequency response function, characterized by the measurements carried on with a peculiar test bench [87]. This model showed satisfactory agreement with experimental measurement conducted with a polymer pin in sliding contact with a glass disc. It should be noticed that the contribution of the system dynamic response, into the calculated perturbative term, is not filtered by this approach.

The above proposed literature of the contact models is certainly not complete and it traces only a string between the main approaches to the contact modelling, with a special regard to the models able to include the contact excitation coming from the surface interface and responsible for friction-induced vibrations. To deepen the literature of contact and friction the reader can refer to several review papers,

such as Bushan [63, 88], Bowden and Tabor [5, 6], Kragelskii [24] and Rabinowicz [89]. Moreover, several specific review on friction-induced vibrations are available into the literature [15, 26].

I-4. Focus and positioning of the thesis

Looking at the works into the literature, the main efforts has been focused on the investigations on unstable Friction-Induced Vibrations, trying to understand the nature of the instabilities and to avoid their arise. Few works focused directly on the analysis and modelling of the dynamic excitation coming from the contact interface, which is at the origin of the vibrational response, either stable or unstable, of the system.

Nevertheless, nowadays, numerical simulations of frictional contacts are more and more used to simulate the behaviour of complex systems with frictional interfaces. The need to account for the dynamic excitation from the contact and its effect of the system vibrational response is more and more of actuality.

In this context, starting from the observation that any frictional contact is accompanied by a broadband excitation from the sliding interface, this thesis wish to focus on this broadband excitation, trying to analyse stable Friction-Induced Vibrations and introduce the broadband excitation from the contact into a transient numerical code.

At this aim, a simple dynamic system is chosen for the study, composed by two steel beams in sliding contact. The simplicity of the system assures indeed an easier decoupling between the local dynamic excitation at the contact and the system dynamics.

The vibrational response of the system (i.e. induced vibrations) has been investigated experimentally and numerically, by means of parametrical analyses. Then, a friction law with a perturbative term, representing the contact broadband excitation, is proposed and validated. The introduction of the excitation directly into the friction law, allows for avoiding the numerical representation of the surface topography and of the third body distribution and evolution. The proposed numerical approach can then be associated to the second family of models in paragraph I-3.2.

The objective of the proposed numerical approach is thus to simulate the dynamic response of the system, by including directly into the proposed friction law the broadband dynamic excitation originated by all the local phenomena occurring at

the contact interface: impact and ruptures between asperities, interaction and evolution of third body, etc.

The absence of the direct description of the surface topography and third body evolution allows for maintaining reasonable computational costs.

II Materials and methods

This chapter has the objective of describing the approach to the problem, the set-ups employed during the experimental campaigns and the numerical models developed to simulate the same phenomena observed in the measurements.

The first section presents the general approach of this work, highlighting the parallel experimental and numerical analyses. Then, the experimental tools are introduced, presenting the two set-ups employed for the measures of the Friction-Induced Vibrations, called *TriboTouch* and *TriboAir*. Finally, the last section concerns the numerical tools, based on the finite element method. In order to analyze the system vibrational response, both the complex eigenvalue analysis (CEA) and the transient analysis (DTA for Dynamic Transient Analysis) have been conducted. The last section of the chapter introduces the contact law used for simulating the broadband excitation generated at the contact interface.

II-1. Analysis methodology

In order to reproduce and analyse the frictional system dynamic response, the work has been divided in two main lines of investigations:

- an extended experimental parametrical campaign, followed by a numerical parametrical analysis;
- the use and validation of a peculiar frictional law, able to reproduce the system dynamics under contact frictional excitation.

The experimental campaign has the objective of characterizing the system and investigating the evolutions in the system vibrational response according to the changes in the contact parameters. The analysis has been focused on the response of the system in terms of Friction-Induced Vibrations, which are originated by the phenomena occurring at the contact (local dynamic excitation) and are the effect of the system dynamic response.

Once the experimental campaign conducted, a numerical model has been developed and investigated to simulate the same frictional conditions. A first parametrical analysis has been developed in parallel to the experimental one, allowing to highlight similarities and differences in the results. Then a new frictional law, implemented into the *Plast2D* code, has been introduced into the model. The objective of the model being the reproduction of the Friction-Induced Vibrations observed during the measurements, the new contact law enables to introduce the broadband excitation from the contact, which excites the system response as in the experiments. Then, the last part of this work is focused on the tuning/up-grading of the parameters of the friction law and the validation of the law by comparison with experiments.

A detailed description of the used experimental and the numerical models is presented in the following sections.

II-2. Experimental tools

The mechanical system chosen for the analysis is composed by two steel beams in relative frictional contact under macroscopical sliding. This choice allows for having a simple dynamics in order to clearly identify the dynamics of the system, within the vibrational response to the broadband excitation from the contact. Moreover, a such simple system allows for better controlling the contact parameters, such as the normal and tangential load, the relative velocity, the surface roughness, etc....

In this work, the contact parameters, varied during the measurements, are the contact normal load F_n , the sliding velocity v , and the surface roughness of the samples in contact. Each contact parameter has been varied during the parametrical campaign with the sake of analyzing the corresponding evolution of the Friction-Induced Vibrations. In Chapter III, the experimental campaign will be extensively described.

The following sections present the two experimental set-up, the TriboTouch and the TriboAir, used for imposing the normal load and relative displacements between the two beams during the parametrical analyses. The use of two set-ups allowed to carry on the parametrical analysis at the two different sites of this research. They both allowed for highlighting the reproductibility and robustness of the performed tests and measurements.

II-2.1 TriboTouch test bench

The TriboTouch test bench has been conceived to measure the contact parameters and the Friction-Induced Vibrations produced by the frictional contacts, reducing parasitic vibrations coming from the set-up [90].

Fig. II-1a presents the set-up. It is composed by a peculiar device that allows the relative motion along the horizontal plane (2). The device consists of a symmetrical couple of double parallelograms with flexible hinges [91, 92]; the movement is assured by the elastic deformation of the hinges. The device is indeed a compliant mechanism. Its characteristics lead to a planar movement of the upper base (Fig. II-1 3) assuring the absence of unwanted sources of friction or parasitic

noise, usually produced by the joints of conventional devices. In such a way, the contact between the two sliding beams is then the only source of vibrations during the measurements.

On the set-up, the two beams have been mounted in order to provide a relative displacement between them, when imposing a contact load between the tip of the inclined beam and the upper surface of the horizontal beam. The beams are then distinguished as beam 1, the upper beam, and beam 2, the lower beam Fig. II-1b. The lower beam is placed on the moving base of the compliant system, the movement of which is assured by a linear voice coil (1) (Gammatic LA15-65-000A), which allows for imposing the wished relative motion. The velocity and position of the base are managed by a controller (Helmo Har-12/60) and a linear optical encoder that allows for closing the position command loop.

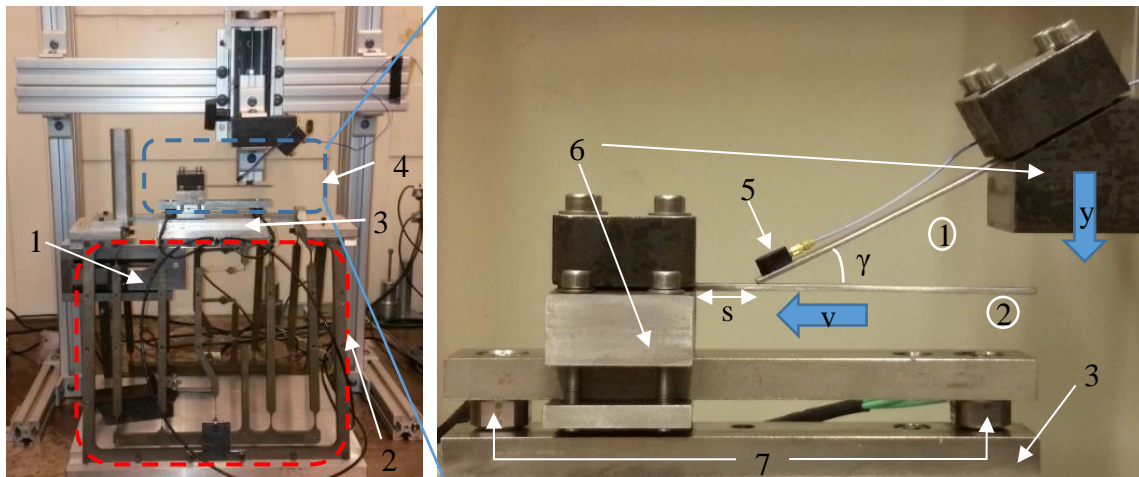


Fig. II-1: a) The TriboTouch test-bench, (1) linear voice coil, (2) compliant device, (3) upper base, (4) fastening system of the beams; b) Magnification of the test-bench on the beams' fastening system, (3) upper base, (5) accelerometer, (6) clamping blocks, (7) force transducers.

Two tri-axial force transducers (Kistler 9017B) are positioned at the connection between the lower beam and the base of the compliant system (7, Fig. II-1b) to measure the overall normal and tangential forces.

An accelerometer (PCB 352A24) placed on the upper beam (5) measures the acceleration perpendicular to the beam upper surface, i.e. the Friction-Induced Vibrations obtained during the sliding between the beams. The chosen accelerometer has a high sensitivity (10.2 mV/m/s^2) and a low mass (0.8 g), allowing the recording of low amplitude vibrations without perturbing the measurements.

Both of the beams are in clamped-free boundary conditions. The clamping condition is ensured by two massive blocks (6 in Fig. II-1b), which play a significant role in the test-bench effectiveness: they filter the dynamics of the simple system under analysis (the two beams in frictional contact) from the more complex dynamics of the whole set-up.

II-2.2 TriboAir test bench

This test-bench has the same objective of the previous one, i.e. to measure frictional parameters and Friction-Induced Vibrations generated by the frictional contacts reducing as much as possible external parasitic noise.

In this set-up, the compliant device has been replaced by an air bearing system Fig. II-2a (3), which assures, as needed, a planar movement of the upper base without introducing unwanted source of friction or parasitic noise. The position of the upper base is steered by the loop of the linear optical encoder (Fig. II-2a (4)) and the controller; the TriboAir has a finer precision in displacement compared to the TriboTouch, a more rigid dynamics and larger ranges of applicable loads and velocities.

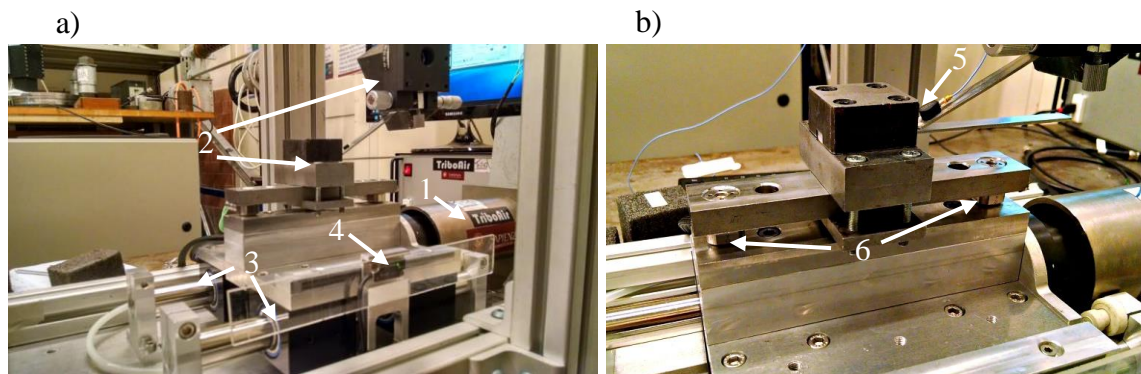


Fig. II-2: a) The TriboAir test-bench: (1) voice coil, (2) clamping blocks, (3) air bushes, (4) linear optical encoder; b) Magnification on the sliding beams (5) accelerometer (6) force transducers

The TriboAir has been used to perform part of the parametrical campaign. While the two set-ups have been both used for the parametrical analysis at the two different sites of this research, the reproducibility of the same measurements on both the set-ups allowed for highlighting the robustness of the performed tests and measurements.

In fact, as stated before, the presence of the two massive clamping blocks allows for filtering the dynamics of the set-up and obtaining comparable measures using the two different set-ups.

Fig. II-3 and Fig. II-4 show the superposition between the time signal and respective spectra of vibrations recovered from the accelerometer with the TriboTouch test bench (red curve) and with the TriboAir test bench (blue curve). The two signals have the same evolution in time and frequency domains; then the performed measurements are not affected by the dynamics of the whole test bench.

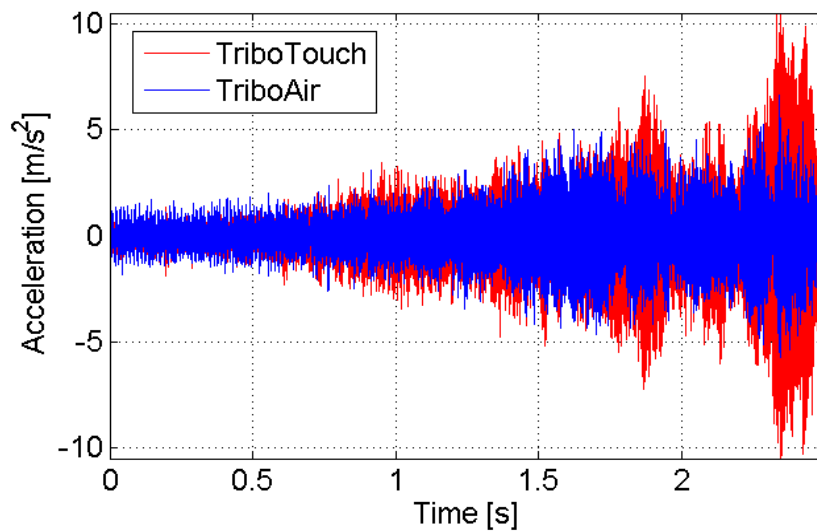


Fig. II-3: Superposition of the time signals from a measure conducted on the TriboAir (blue) and one on the TriboTouch (red). The normal load imposed is of 8N, the sliding velocity of 8 mm/s, surface roughness R120.

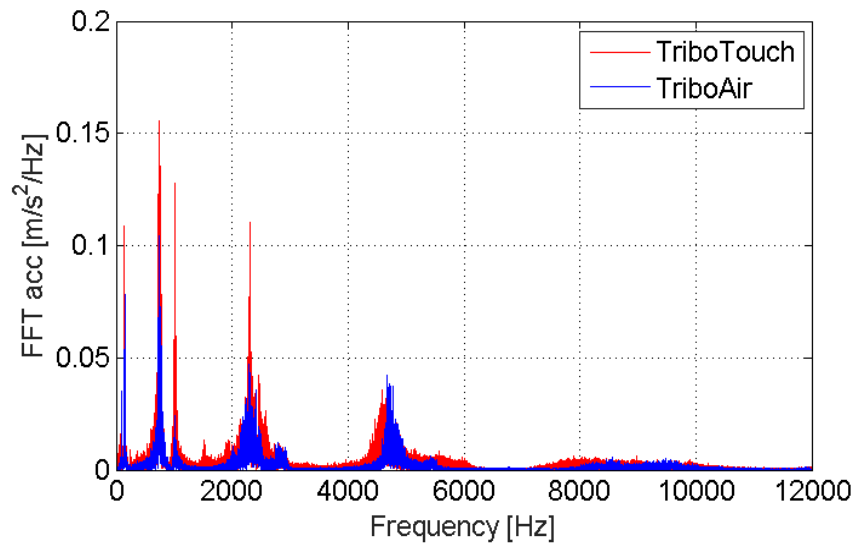


Fig. II-4: Superposition of the spectra of the signals (FFT) from a measure conducted on the TriboAir (blue) and one on the TriboTouch (red). The normal load imposed is of 8N, the sliding velocity of 8 mm/s, surface roughness R120.

II-3. System and contact definition

This section describes in detail the geometry of the beams and the polishing protocol to which they have been subjected before each measurement.

Fig. II-5 shows the drawings of the upper beam: inset a) for the front view, inset b) for the upper view, with the relative dimensions, and a three-dimensional view, inset c). The lower beam has been subjected to the same machining (Fig. II-6), the only difference with the upper beam is in the length and thickness dimensions, as presented in Tab. II-1

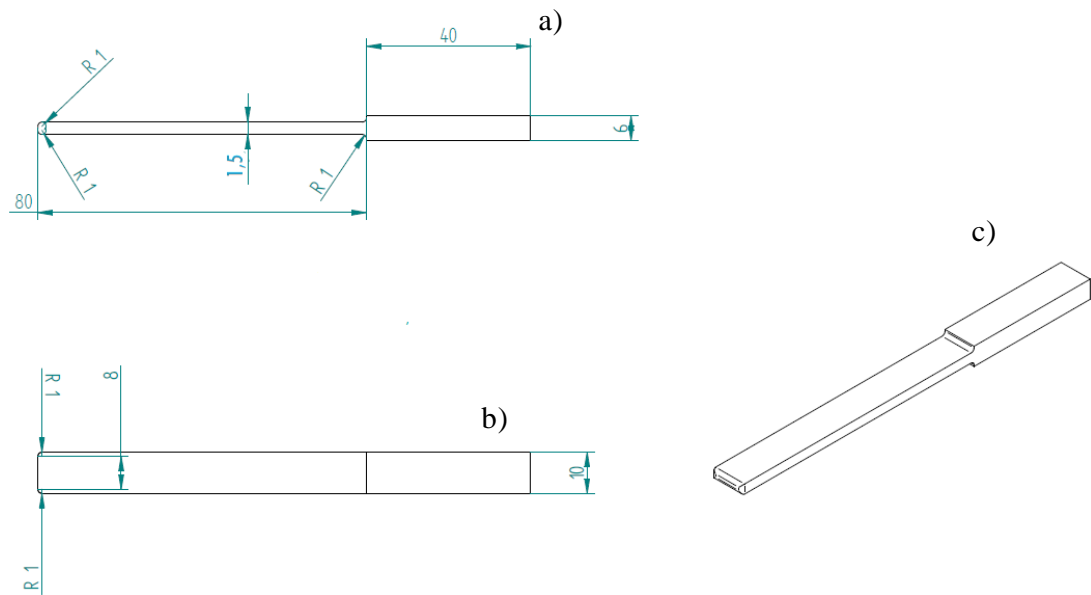


Fig. II-5: Perspective drawing of the upper beam, a) Front view, b) Upper view, c) Three-dimensional view. The dimensions are expressed in mm.

Two main characteristics have to be underlined in Fig. II-5: the presence of two radii at the tip of the beam; the existence of a “beam head” of larger thickness and with a smoothing radius.

The radii of the tip will be distinguished as r_1 in the plane of the beam and r_2 in the perpendicular plane. Both the radii have a dimension of 1 mm, as described in Fig. II-5.

The upper beam has been machined with the two radii of curvature in order to have a reproducible contact surface at the middle of the contacting edge (Fig. II-7), maintaining in this way as constant as possible the contacting zone during the several tests. Moreover, in such a way, the contact area as been reduced as much as possible to avoid problems related with parallelism and to be successively approximated to contact point (see chapter V).

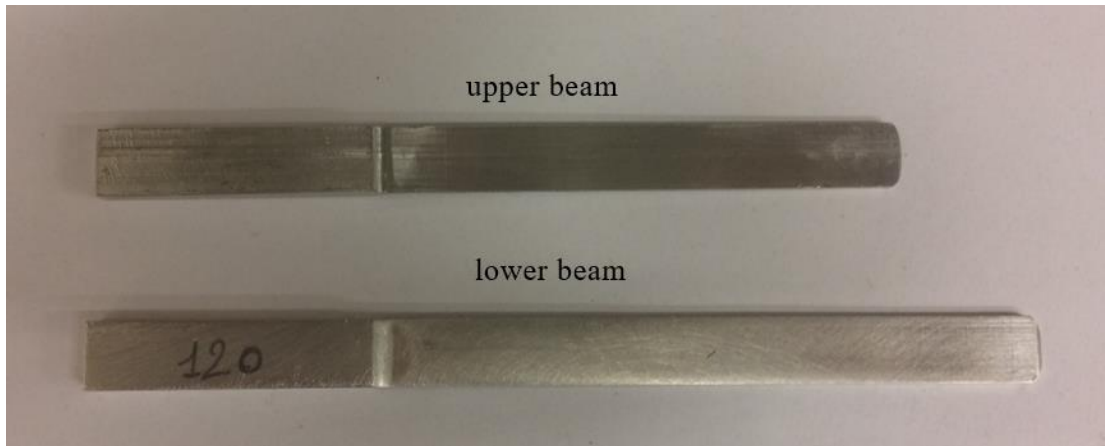


Fig. II-6: Photo of the upper and lower beam, upper view.

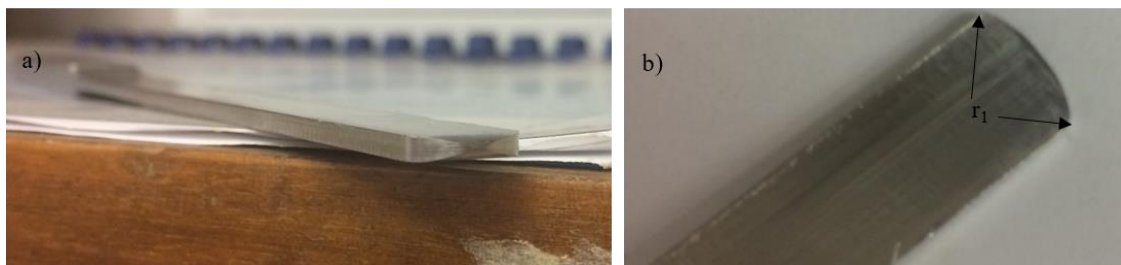
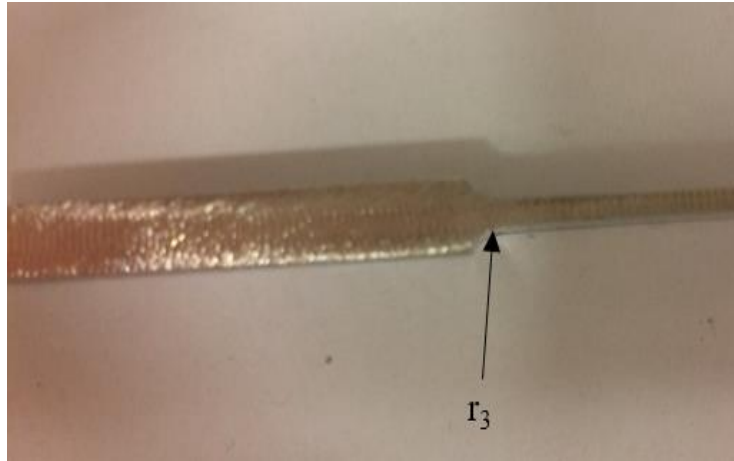


Fig. II-7: a) Tip of the upper beam, characterized by two radii of curvature; b) Magnification on the radius r_1 on the plane of the beam

The “beam head” has been machined to have a thicker part, with the same length of the clamping blocks, in order to determine a condition at the beam edge as close as possible to the clamped condition, with displacement and rotations equal to zero. In fact, the presence of a head with a larger thickness allows to reduce the deformation at the clamping, when the lower beam is subjected to the contact with the upper beam.

The angle that connects the beam head to its surface has been smoothed with a radius ($r_3=1\text{mm}$), to avoid the rise of a stress concentration zone and distribute uniformly the stress along the rounded surface (Fig. II-8).

Fig. II-8: Beam's head with the smoothing radio r_3

Tab. II-1 shows the geometry and the material characteristics of the used beams. Because of the surface hardness and a good behavior in term of wear, the chosen material is the inox steel. The parameter s (Fig. II-1b) in Tab. II-1 is the distance from the clamping block of the horizontal beam at which the contact between the beams is engaged. The dimensions of the beams (L_1 and L_2) have been chosen after carrying on a complex eigenvalue analysis, in order to avoid mode coupling instabilities. This analysis assures that, with the chosen dimensions of the beams, the natural frequencies of the beams are enough far away from each other in order to avoid the mode coupling instability. Section II-3.1 and IV-1.1 will describe in detail the complex eigenvalue analysis carried on to define the geometrical dimensions.

	Beam	
	①	②
Young modulus E [GPa]	210	210
Density ρ [Kg/m ³]	7800	7800
Poisson ratio	0.3	0.3
Dimensions [mm]Length \times width \times thickness	$L_1=80 \times 10 \times 1.5$	$L_2=100 \times 10 \times 2$
Distance from clamped point B	$s = 5 \text{ mm}$	
r_1 [mm]	1	
r_2 [mm]	1	
Leaning angle γ	30°	

Tab. II-1: Geometry's and material's characteristics of the beams

Before each frictional test, the surface of the lower beam and the tip of the upper beam have been subjected to a polishing treatment. Three sandpapers (Tab. II-2) have been chosen to test different surface roughness and investigate, during the parametrical campaign, the influence of the surface roughness in the system dynamic response, in term of Friction-Induced Vibrations.

The polishing protocol has been followed before each test, with the same steps for all the sandpapers:

- The beams are previously cleaned by a towel wet with ethanol.
- The operator, equipped with gloves, cut a piece of the sandpaper and moves it along the beam surface with circular movements and constant force (normal load), in order to generate an isotropic topography of the surface. The number of passages of the sandpaper on the surface is maintained as constant as possible.
- After the polishing treatment the beams are subjected to two consecutive cleanings: first an air flux scatters the particles generated during the rubbing with the beam; then, a towel wet with the ethanol is passed along the polished surfaces.

R120	R320	R800
$R_{a_s} = 0.55 \mu\text{m}$,	$R_{a_s} = 0.45 \mu\text{m}$	$R_{a_s} = 0.34 \mu\text{m}$

Tab. II-2: Average roughness R_a from the measure of the three used sandpapers

The obtained surface roughness has been measured with a profilometer (Altisurf 500), able to recover the surface topography. The roughness profiles have been measured both in the longitudinal and transversal direction to the beam axes, to be sure of having an isotropy surface roughness, with no preferential direction in the asperities distribution and repeatable roughness parameters.

Fig. II-9, Fig. II-10 and Fig. II-11 present the roughness profile measured along the direction transversal to the beam axis for the three used sandpapers, R120, R320 and R800.

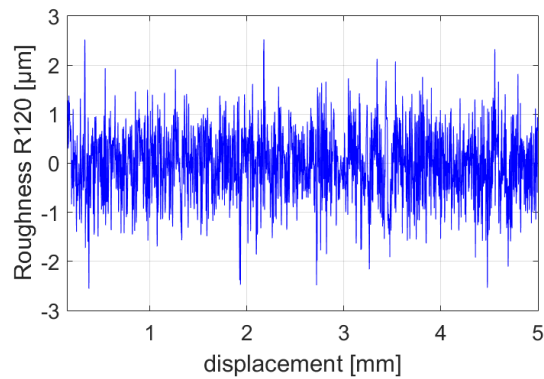


Fig. II-9: Measured roughness profile for the beam surface roughness, sandpaper chosen for polishing R120

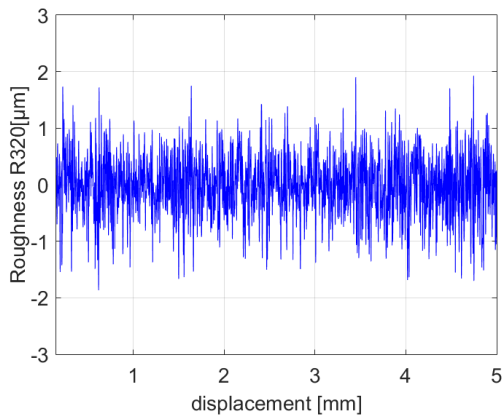


Fig. II-10: Measured roughness profile for the beam surface roughness, sandpaper chosen for polishing R320

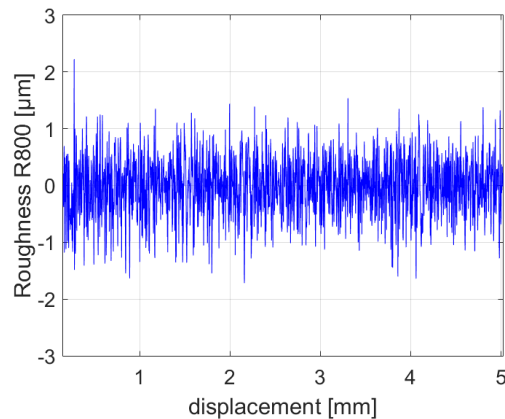


Fig. II-11: Measured roughness profile for the beam surface roughness, sandpaper chosen for polishing R800

Fig. II-9, Fig. II-10 and Fig. II-11 present the roughness topography. For each surface roughness a different set of beams has been used, in order to reproduce always the same roughness profile on the same beam set.

Tab. II-2 shows the arithmetic mean deviation of the asperity heights of the three used sandpapers, R_{a_s} . Tab. II-3 presents instead the roughness parameter R_a for the polished surfaces of the beams, which will be indicated as R_{a_b} . The polishing treatment cannot reproduce the same asperities distribution of the chosen sandpaper and, for this reason, there are small differences between the R_{a_s} values, relative to the sandpaper surface, and the R_{a_b} values, relative to the beam surface. Nevertheless, the values of R_{a_b} identify three surfaces with a different roughness,

which allows the study of the influence of a change in the surface roughness into the system's dynamic response.

R120	R320	R800
$R_{a_b} = 0.51 \mu\text{m}$,	$R_{a_b} = 0.39 \mu\text{m}$	$R_{a_b} = 0.34 \mu\text{m}$

Tab. II-3: Average roughness R_{a_b} from the measures of the polished surfaces

Once described the polishing protocol, it is necessary to describe the measurement protocol, which characterized all the experimental campaigns for the two used test benches. The protocol assured the repeatability of the measures, providing reliable measurements.

The following protocol has been repeated for each test carried on. A vertical displacement is imposed to the vertical blocking system (by means of a screw-guide mechanism) to put the two beams in contact (Fig. II-1b) until the reaching of the wished contact load, monitored by the force transducers. Then the upper base of the set-up, where the lower beam lies, is steered by the voice coil and the controller with a constant sliding velocity v . The vertical displacement imposed is maintained constant during the measure, then the contact normal load varies slightly during the measure, due to the elastic deformation of the horizontal beam under the variation of the position of the loading (contact) point.

For the analysis, to assure a mean constant value of the normal load, a selection of the signal has been operated, removing the initial phase, corresponding to 2 mm of sliding, and considering 20 mm of sliding distance. The complete measurement protocol is described in Chapter III, where the results from the parametrical experimental campaigns are presented and discussed.

II-4. Numerical tools

The frictional dynamic system, investigated experimentally, has been reproduced and analyzed numerically. First, a Finite Element model has been developed for the dynamic analysis of the structure, by a pre-stressed modal analysis (Complex Eigenvalues Analysis) focused on the stability of the system. A second Finite Element model has been then developed to reproduce the transient behavior (Dynamic Transient Analysis) of the system, by simulating the frictional contact between the two beams, first with a classic Coulomb law and then with the new law implementing a perturbative term.

The commercial software ANSYS has been employed for the dynamic analysis. An in-house software, PLAST2D [93, 94], explicitly developed for the reproduction of contact issues in explicit dynamics, has been used.

In the following sections, these models will be described, detailing the governing equations, the geometry, the bounding conditions and the implemented contact law.

II-4.1 FEM modelling for system dynamic analysis (CEA)

The purpose of the dynamic analysis is to determinate the natural frequencies and the mode shapes of the system, choosing the suitable geometrical dimensions of the beams in order to assure stable vibrations, i.e. avoiding mode coupling conditions that would give origin to unstable vibrations [95].

Fig. II-12 presents the model implemented into the ANSYS software. It is a 2D model including the two beams and the contact definition between the tip of the upper beam and the upper surface of the lower beam. The choice of a 2D model allows to save computing time by reducing the number of nodes and elements; indeed the dynamic problem can be considered as a *plane strain* problem, neglecting the deformation perpendicular to the sliding plane (ε_z). On the other side, such simplification will neglect the out-of-plane modes and the torsional modes of the system. Fig. II-12a shows the model with the lower beam, beam 2, and the upper one, beam 1.

The boundary conditions have been chosen to approach the same conditions imposed experimentally with the TriboAir and the TriboTouch set-ups. The lower beam is subjected to a clamped-free condition, Fig. II-12b showing a magnification of the point B where the beam is clamped. By the prestressed analysis, the point C of the upper beam (Fig. II-12c) is subjected to a vertical displacement to reach the contact with the lower beam at the wished normal load.

Once the contact between the two beams is assured, a relative horizontal displacement is imposed. In this dynamic model, the horizontal movement is applied to beam 1 with a constant velocity $v(t)$.

A particular attention is paid to the simulations of the clamping conditions, which experimentally have been realized by the massive blocks.

A perfect clamp (displacements and rotations equal to zero) is impossible to realize in practice and the boundary conditions employed in the numerical model show a higher stiffness than the experimental ones.

The numerical frequencies of the system are affected by this discrepancy and they result higher than the experimental ones (Tab. II-4). To overcome this problem, the numerical model has been improved by adding a layer of less stiff material at the connection of the beam with the frame, in order to simulate the lower stiffness of the clamping condition. Fig. II-12b and Fig. II-12c show the magnification for the constraint edges of the beams, where the effective compliance of the connection is introduced by two layers of elements with less stiff material.

To obtain the same natural frequencies observed experimentally during the sliding test, a parametrical complex eigenvalue analysis has been carried on. The Young modulus of the material of the intermediate layers has been updated to recover a good correspondence between the experimental and the numerical natural frequencies (Tab. II-5).

Experimental frequencies [Hz]	Numerical frequencies [Hz]	Percentage error $\varepsilon\%$
142	175	23,2
738	903	22,4
1021	1096	7,3
2306	2907	26,1
2463	3066	24,5

Tab. II-4: Comparison between the experimental and the numerical natural frequencies calculated with initial stiffer modelling

Experimental frequencies [Hz]	Numerical frequencies [Hz]	Percentage error $\varepsilon\%$
142	144	1,4
738	758	2,7
1021	955	6,5
2306	2529	9,7
2463	2774	12,6

Tab. II-5: Comparison between the experimental and the numerical natural frequencies obtained with a layer of less stiff material (updated model)

From the developed model, two eigenvalues analyses have been carried on:

- the first one to determine the geometrical dimensions of the beam to assure stable vibrations,
- the second one to choose the appropriate Young modulus for the intermediate layers at the clamped edges.

Both the analysis are characterized by the coupling of a preliminary static structural analysis followed by a pre-stressed modal analysis.

The static analysis simulates the loading phase between the beams and imposes the sliding condition. A vertical displacement is applied on the point C until the reaching of the contact between the upper and the lower beam, followed by a horizontal displacement to reach the sliding condition at the contact interface.

The contact between the beams is managed by the ANSYS software as a “frictional contact” with a constant friction coefficient $\mu=0.45$ (see section III-2). The method used to solve the contact problem is the Augmented Lagrange [96], which is a penalty-based contact formulation. The penalty formulation [97] introduces a contact stiffness, k , allowing a small penetration between the bodies in contact, x_p , for a chosen normal load F_n , Fig. II-13.

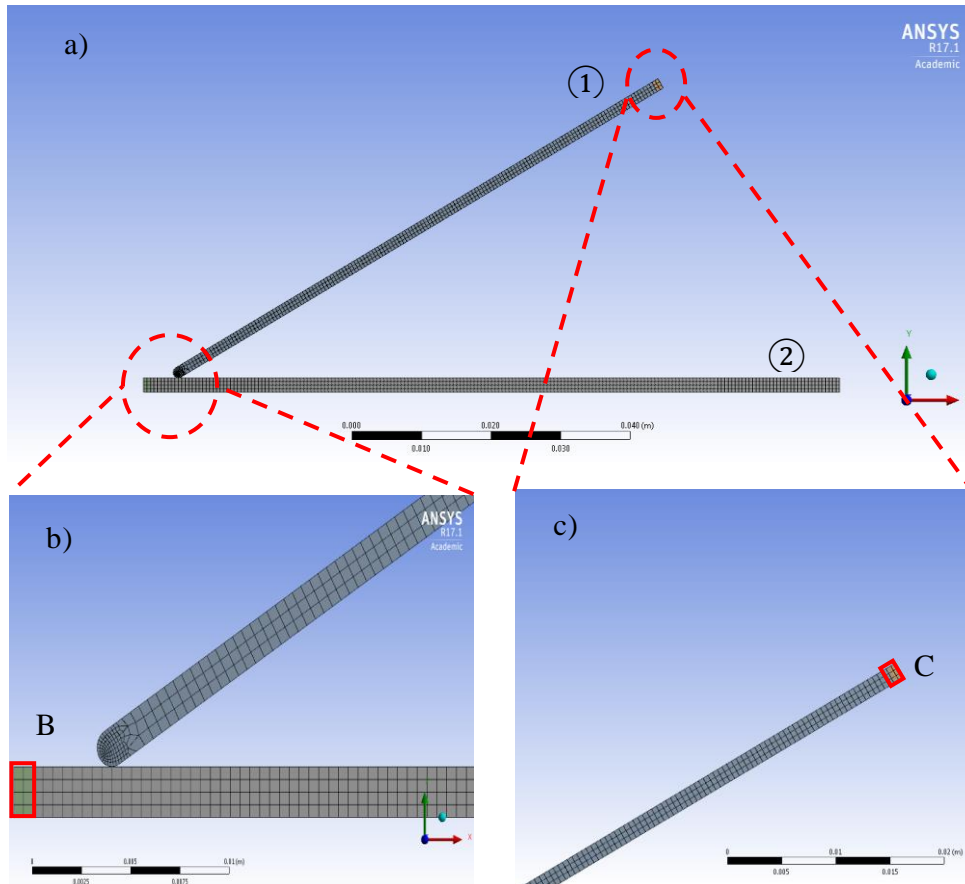


Fig. II-12: Representation of the numerical model implemented in Ansys, a) Complete model; b) Magnification on the clamped lower beam on point B; c) Magnification on the upper beam's edge on point C.

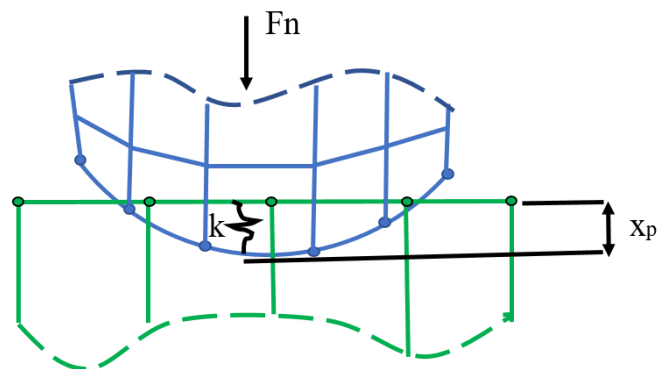


Fig. II-13: Contact stiffness, k , penetration, x_p , and normal force, F_n , for two bodies in contact with the Penalty formulation

The choice of a higher contact stiffness k determines a lower penetration x_p , Eq.2.1:

$$F_n = k \cdot x_p \quad \text{Eq.2.1}$$

The Augmented Lagrange method introduces an extra term, λ , into the contact law, making the normal force less sensitive to the contact stiffness, Eq.2:

$$F_n = k \cdot x_p + \lambda \quad \text{Eq. 2.2}$$

This method has been chosen because the slight penetration admitted x_p allows for an easier convergence of the problem in comparison to other contact formulations. Nevertheless, the introduced error is not relevant for the dynamic analysis of the whole system.

Among the results of the static structural analysis (force reaction, deformation, stresses...) the contact status has to be checked carefully: the condition needed to simulate the same experimental condition is the *sliding state* condition, in which the beams are in sliding contact. Under the contact condition, the system of the two beams can be treated as a *coupled* system and the asymmetric terms of the stiffness matrix allow for investigating the stability of the system.

Starting from this condition a modal analysis has been carried on, obtaining the complex eigenvalues and modal shapes of the system.

Chapter IV, sections IV-1.1 and IV-1.2, will describe in detail the complex eigenvalue analysis computed to choose the beam dimensions and the eigenvalue analysis carried on to determine the correct Young modulus for the intermediate layers at the clamped edges

II-4.2 FEM model for transient simulations (DTA)

The objective of this section is to describe the numerical model employed to reproduce the transient dynamic response of the system, from the loading phase with the contact between the beams until the end of the sliding phase. Furthermore, the model has to reproduce the frictional contact between the two beams. By the contact point of view, to reproduce with accuracy the transient state, two main effects have to be taken into account: the quasi-static frictional response due to the mean normal and tangential forces (Fig. II-2b (6)); the dynamic system response to the contact broadband dynamic excitation, resulting in Friction-Induced Vibrations.

The software used for the transient analysis is PLAST2D [94], which is an in-house explicit FEM code designed for large deformations and non-linear contact behavior. The used contact algorithm applies the Forward Lagrange Multiplier method [98]. To detect the contact, the algorithm defines the slave nodes and the target elements. In this model, the nodes of the beam 1 characterized by the refined mesh (Fig. II-15b) are the slave nodes; the elements of the upper surface of the beam 2, where the contact is engaged, are chosen as target elements. Each body is modeled with a four nodes quadrilateral element with 2x2 Gauss quadrature rule, while the target segments are composed by two nodes and approximated by bicubic spline [99].

Focusing on the forward Lagrange multiplier method, it is characterized by an equation of motion formulated at the time $t_i = i \Delta t$, with the displacement conditions imposed on the slave nodes at the time t_{i+1} :

$$\begin{cases} M\ddot{u}^i + C\dot{u}^i + Ku^i + G^{(i+1)T}\lambda^i = F^i \\ G^{i+1}\{X^i + U^{i+1} - U^i\} \leq 0 \end{cases} \quad \text{Eq.2.3}$$

M , C and K are respectively the mass, damping and stiffness matrix. M and K are symmetric and defined positive. For the damping matrix C , the Rayleigh damping model has been employed (see section III-1).

X is the coordinate vector calculated at the time t^i . \ddot{u} , \dot{u} , u represent respectively the vector of nodal accelerations, velocities and displacements. F is the vector of the external forces.

$\lambda = [\lambda_n \ \lambda_t]$ is the vector of the surface contact forces, composed by the normal forces, λ_n and the tangential forces, λ_t .

$G^T = [G_n^T \ G_t^T]$ represents the global matrix of the displacement conditions. It assures the condition of non-penetration and determines the contact law.

The equation 2.3 is solved with a direct time integration, the explicit Newmark scheme; \ddot{u} , \dot{u} are defined at each time step by the time scheme of type β_2 ($\beta_2 \in [0.5; 1[$):

$$\begin{cases} \ddot{u}^i = \frac{2}{\Delta t^2}(u^{i+1} - u^i - \Delta t \dot{u}^i) \\ u^i = \frac{1}{1+2\beta_2} \left\{ \dot{u}^{i+1} + \Delta t(1 - \beta_2)\ddot{u}^{i-1} + \frac{2\beta_2}{\Delta t}(u^{i+1} - u^i) \right\} \end{cases} \quad \text{Eq.2.4}$$

The displacement $u^{*(i+1)}$ at the contact nodes are calculated for the initial step under the condition $\lambda^i = 0$, thus without the presence of the contact forces. Choosing $\beta_2 = 0.5$ the nodal displacement at the time $t^{*(i+1)}$ is the following:

$$u^{*(i+1)} = \Delta t^2 M^{-1}(F^i - Ku^i) + 2u^i - u^{i-1} \quad \text{Eq.2.5}$$

After the first step, if the slave nodes have penetrated through the target surface, the matrix G^{i+1} is formulated, generating the contact forces λ^i and the displacements at the time t^{i+1} :

$$\begin{cases} \lambda^i = \left(\Delta t^2 G^{i+1} M^{-1} G^{i+1 T} \right)^{-1} G^{i+1} (u^{*(i+1)}) \\ u^{(i+1)} = u^{*(i+1)} - (\Delta t^2 M^{-1} G^{i+1 T} \lambda^i) \end{cases} \quad \text{Eq.2.6}$$

Eq.2.6 are solved with the Gauss-Seidel method. The method employed to solve the transient dynamics of the system is a coupling between the Newmark method (for the time resolution) and the Forward Lagrange Multiplier method (for the contact conditions). The Lagrange Multiplier method allows to assure the non-penetration between the slave nodes and the target surface, imposing contact conditions closer to the real surface status than other methods commonly used, as the Penalty method [97]. At the same time, the introduction of the unknown λ^i term increases the computational effort.

For each iteration step, two conditions have to be checked at the slave node:

$$\lambda_n^k \leq 0 \begin{cases} \lambda_n^k < 0 & \text{contact condition} \\ \lambda_n^k = 0 & \text{separation condition} \end{cases} \quad \text{Eq.2.7}$$

$$\|\lambda_t^k\| \leq \mu \|\lambda_n^k\| \begin{cases} \text{if } \|\lambda_t^k\| < \mu \|\lambda_n^k\| \rightarrow \dot{u}_t = 0 \rightarrow \text{stick} \\ \text{if } \|\lambda_t^k\| = \mu \|\lambda_n^k\| \rightarrow \lambda_t \cdot v_t \leq 0 \rightarrow \text{slip} \end{cases} \quad \text{Eq.2.8}$$

λ_n^k and λ_t^k represents the normal and the tangential contact load at each k slave node, μ is the friction coefficient. Eq. 2.7 describes the contact normal force as a compression force, eq.2.8 characterizes the used friction law, distinguishing between the stick and the slip conditions. The used friction laws in this work are the Amontons-Coulomb law [2, 3] and a modified version of this law, characterized by a friction coefficient with a term of perturbation, as it will be described in the next section.

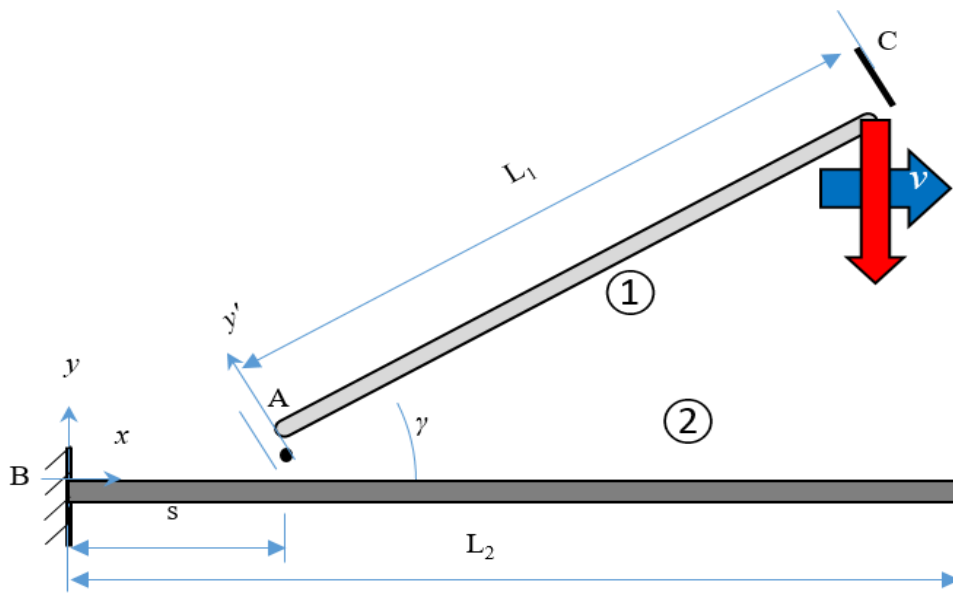


Fig. II-14: 2D numerical model of the frictional system.

Fig. II-14 presents the developed numerical model. As for the model realized in ANSYS, the geometry dimensions and the boundary conditions reproduce the experimental ones. Also for this analysis, a plane strain 2D model has been developed. The parametrical complex eigenvalue analysis, section IV-1.2, will show that using two layers of less stiff material for the clamped edges, the experimental boundary conditions are better simulated. Transient simulations have been performed both with (Fig. II-15) and without the layers of different materials, in order to verify the effect of the layers into the transient vibrational response of the system.

Fig. II-15 shows the chosen mesh. The elements with a different color represent the clamped edges with a less stiff material. The material properties are the same presented for the ANSYS model, Tab. II-6.

Fig. II-15b is a magnification of Fig. II-15a, which underlines the nodes, in red, where the accelerometer is placed during the experimental tests. The average of the acceleration calculated in these nodes, along the same direction measured by the accelerometer, will be taken in consideration to analyze the dynamic response of the system, e.i. the Friction-Induced Vibrations. Tab. II-6 presents the parameters used in this numerical model.

When simulating the vibrational response in contact issue, it is necessary to account for a realistic estimation of the system damping, due mainly to material

damping and energy dissipation at the joints with the blocks. Within the numerical model, the damping term is modeled with the Rayleigh damping (i.e. proportional damping):

$$C = \alpha M + \beta K \quad \text{Eq.2.9}$$

where C is the damping matrix, composed by the sum of the matrix mass M multiplied by the α coefficient and the stiffness mass K multiplied by the β coefficient.

In order to be representative, as much as possible, of the real energy dissipation, the choice of the mass and stiffness damping coefficients have been subjected to a specific experimental analysis. In section III.1, the analysis carried on to evaluate the damping coefficients is described in detail.

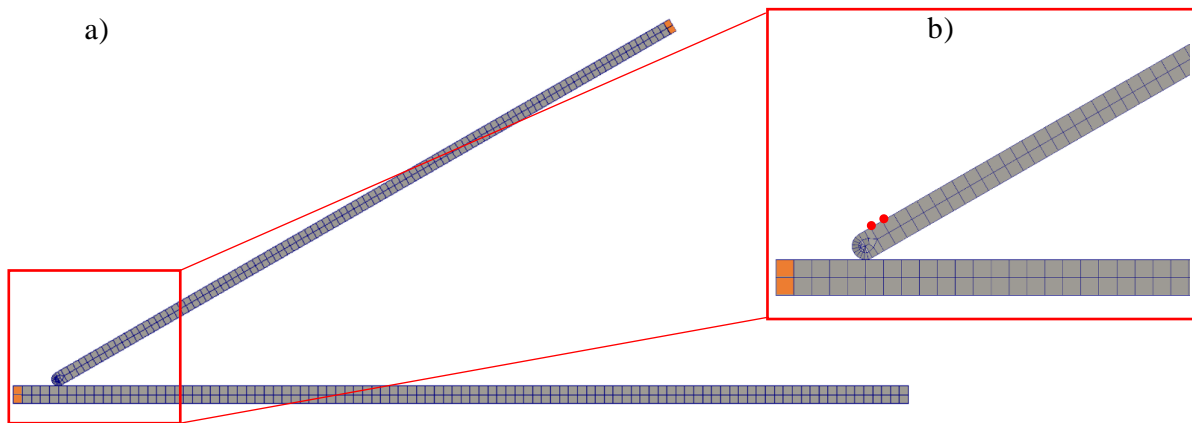


Fig. II-15: a) Representation of the mesh of the transient model, where the orange color represents the elements with a less stiff material; b) Magnification of the mesh, where the nodes underlined in red are at the same position of the accelerometer in the experimental campaign

	Beam	
	①	②
Young modulus E [GPa] beams	210	210
Young modulus E [GPa] edges	21	21
Dimensions [mm]Length \times width \times thickness	$L_1=80 \times 10 \times 1.5$	$L_2=100 \times 10 \times 2$
Distance from clamped point B	$s = 5$ mm	
Upper beam edge radius r [mm]	1	
Leaning angle γ	30°	
Mass Matrix damping coefficient $\underline{\alpha}$ [s^{-1}]	10	
Stiffness Matrix damping coefficient $\underline{\beta}$ [s]	$5e-9$	

Tab. II-6: Characteristics of the numerical model

II-4.3 Modified friction law

In this work two friction laws have been applied. The first one is the classic Amontons-Coulomb law, which employs a constant coefficient of friction, which has been recovered from the experimental tests:

$$F_t = \mu F_n \mu(x) = \mu_{const} = 0.45 \quad \text{Eq.2.10}$$

where F_t represents the contact tangential force and F_n the normal contact force. The first set of numerical simulations has been carried on with this law, considering only the presence of the mean friction force at the contact interface, without accounting for the presence of the surface roughness and local dynamic excitation coming from interface phenomena such as impacts between the asperities of the surfaces, local ruptures of the interface, evolution of the third body, ...

The results from this simulation are shown in section IV-2.2. From the comparison with the experimental results it is clear that this law is not able of correctly simulate the vibrational response of the system, i.e. the Friction-Induced Vibrations, ignoring the local phenomena which happen at the contact interface. It is then essential to introduce a friction law able to reproduce the contact dynamic excitation, accounting for the effect of the presence of surface roughness

and local contact dynamic phenomena. For this sake, a modified formulation for the friction law has been introduced (Eq.2.11):

$$\mu(x) = \mu_{const} + \mu_{perturbative} = \mu_{const} + A|v(t)|^b R(x) \quad \text{Eq.2.11}$$

The proposed law introduces two different terms in the friction coefficient: the first term, μ_{const} , is the constant term previously used with the Amontons-Coulomb law; the second term, $\mu_{perturbative}$, is a perturbative term, which has the objective to represent the broadband excitation from the contact interface.

For the proposed formulation, three multiplicative factors compose the perturbative term: A , $|v(t)|^b$ and $R(x)$.

- $|v(t)|^b$ represents the influence of the sliding velocity on the amplitude of contact excitation. According to the choice of the exponent b , it is possible to simulate a linear [100], quadratic or different bond between the sliding velocity and the amplitude of the perturbative term. In this work, a linear bond has been introduced, according to the experimental evolution of the system frictional dynamic response with the sliding velocity, as described in section III-3.1.
- The factor $R(x)$, is a vector representing the evolution of the excitation signal with the sliding distance at the contact interface, and it determines the spectral distribution of the dynamic excitation. The signal $R(x)$ is introduced for each contact node as a function of the relative sliding distance x . Then, considering the sliding velocity of the contact node for each time step, during the sliding of the slave node on the conjugate target surface, the time evolution of the perturbative term can be calculated.
- Finally, the term A considers the influence of other contact parameters, such as for example the normal contact load, which affect the amplitude of the dynamic excitation from the contact.

The modified Amontons-Coulomb friction law with perturbative term has the aim to simulate the local contact broadband excitation (due to the local phenomena such as impacts and ruptures between asperities) and the following dynamic response of the system in term of induced-vibrations, without describing the surface and third body topography into the mesh of the model. Indeed, the mesh chosen for the analysis is a coarse one (Fig. II-15). In fact, without the representation of the physical local topography of the surfaces, there is no need in increasing the dimension of the model with extremely finer elements at the contact.

A convergence analysis on the overall frictional behavior (mean normal and tangential forces) has been carried on in order to choose the mesh at the contact. The minimum edge length obtained for the contact interface has the size of 0.07mm.

III Experimental analysis

This section has the purpose to describe the parametrical experimental campaigns carried on to characterize the frictional response of the investigated system [100]. The first part focuses on the dynamics of the system, identifying its natural frequencies as well as the modal damping factors. The second part presents the followed protocol for the frictional measurements, together with the analysis of the system response both in time and frequency domains. The third part outlines the results of the experimental campaigns, analysing the effects of the different parameters (normal load, sliding velocity and surface roughness) on the system vibrational response, i.e. on the Friction-Induced Vibrations. The last section draws the conclusions of the three parts, underling the main results.

III-1. Dynamics of the system

The system dynamics has been investigated through the measurement of the frequency response function of each subsystem. Each subsystem is composed by the beam, already clamped on its respective support. In such a way, the frequency response function accounts for all the system characteristics (beam, stiffness, damping and mass of the clamping system, etc.), except for the contact between the two beams. Thus, each beam has been subjected to the analysis in order to characterize the behaviour of the uncoupled system and to distinguish the natural frequencies corresponding to each subsystem. In fact, the small contact surface and the simple system dynamics allows for better identifying the contribution of each subsystem dynamics on the assembled system dynamics

The modal analysis frequency response functions have been determined employing a hammer impact technique. The beams have been excited with an impulsive force by an instrumented hammer with a steel tip (wider band of excitation). An accelerometer has been positioned on the beams on the opposite side to the excitation, obtaining the response at the drive point.

Fig III-1 and Fig. III-2 show the Frequency Response Function (FRF) of the upper (beam1) and lower (beam 2) subsystems from the measure at the drive point and the associated coherence. Only the first two natural frequencies of the beams are visible, after 2000 Hz the coherence starts to decrease severely and the results are no more acceptable. This behaviour is probably due to the compliance of the beams, which does not allow to provide a short impact in order to achieve higher frequencies.

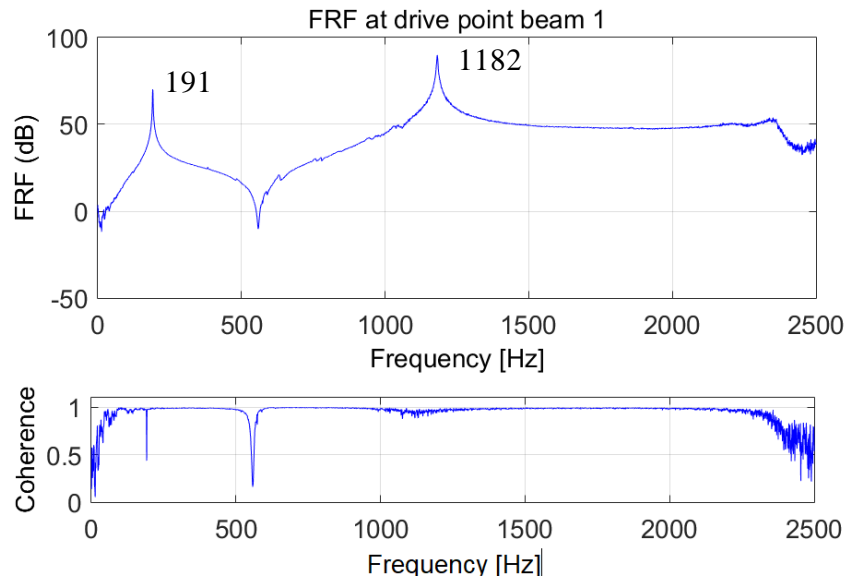


Fig III-1: FRF of the upper beam (beam 1) and coherence of the measure

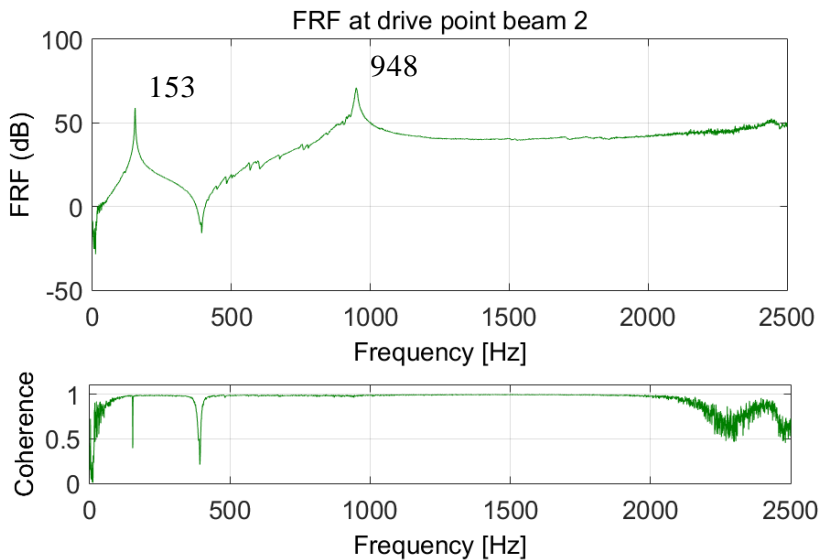


Fig. III-2: FRF of the lower beam (beam 2) and coherence of the measure

The FRFs have been used as well for identifying the modal damping factors of the subsystem, allowing for obtaining the Rayleigh coefficients α and β , which better fit the evolution of the damping factors in the frequency range of interest.

$$\alpha = 10$$

$$\beta = 5e - 9$$

The modal damping corresponding to each natural frequency has been calculated by the half-power method. For each subsystem (beam mounted on the clamping

structure), the values of the α and the β coefficients that better fit the modal damping values have been chosen (Fig. III-3 dotted curve).

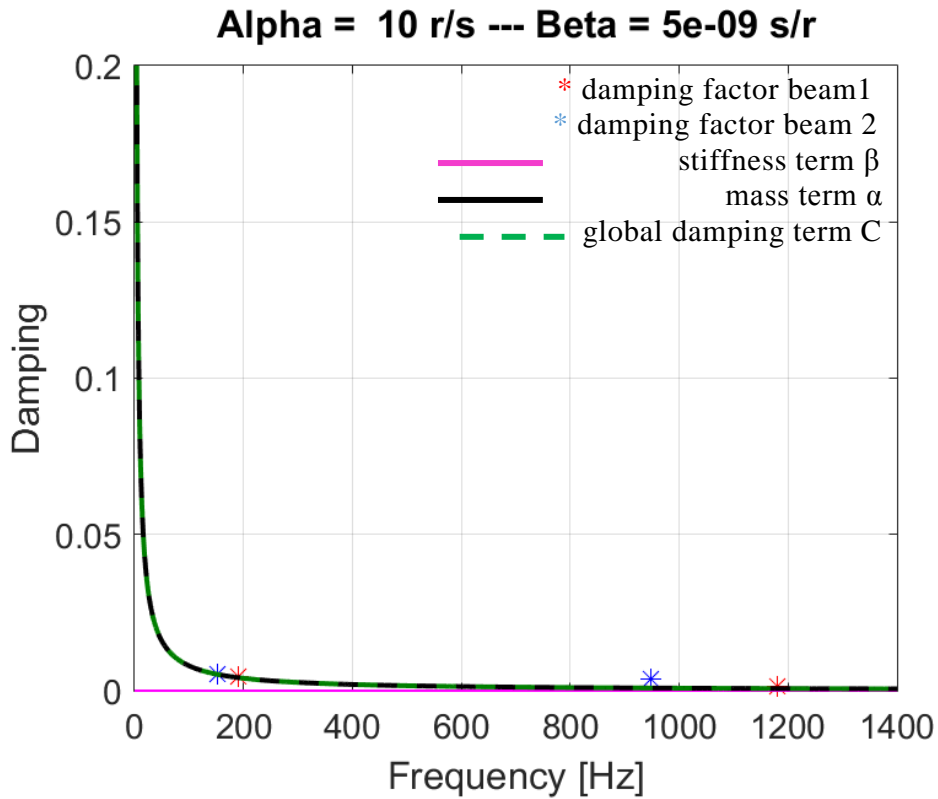


Fig. III-3: Evolution of the damping terms α and β with the frequency range

Fig. III-3 shows the evolution of the modal damping terms in the frequency domain: the red points represent the modal damping factors of the upper subsystem (beam 1); the blue points are the modal damping factors of the lower subsystem (beam 2). The pink and the black curves represent the stiffness and mass contribution to the Rayleigh damping, while the green dotted curve represents the total damping introduced into the model.

For both the beams, the first frequency represents the first bending mode, while the second frequency is the second bending mode. Because the drive point has been chosen on the upper surface, and the force is perpendicular to the beam axis, the torsional and longitudinal modes are not excited.

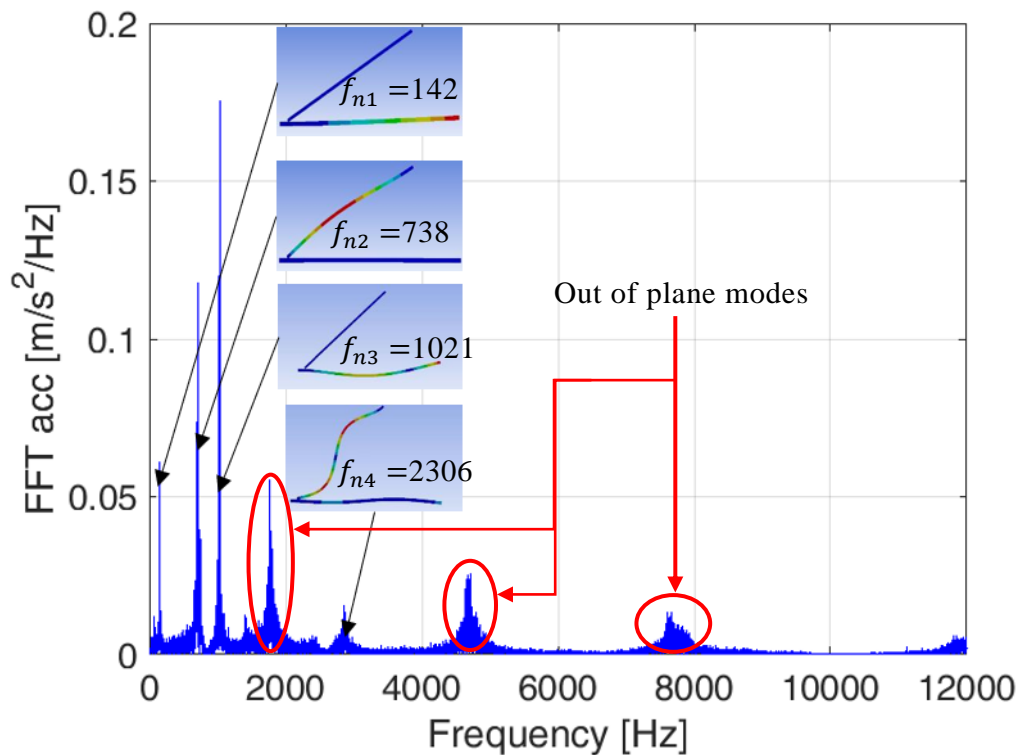


Fig. III-4: FFT of the coupled system (beams in contact), normal contact load 8N, sliding velocity 8mm/s, surface roughness R320

Because it is not possible to perform a frequency response function during the sliding condition, in order to recover the natural frequencies of the coupled system, the spectrum of the acceleration measured during the sliding transient phase has been considered.

In such a way, looking at the peaks of the spectrum, it is possible to identify the natural frequencies of the assembled system in operating conditions.

Fig. III-4 presents the Fast Fourier Transform (denoted thereafter FFT) obtained from the measure by the accelerometer. The measure correspond to an imposed normal load of 8N, a sliding velocity of 8 mm/s and a surface roughness R320, characterized by $R_a=0.45 \mu\text{m}$.

Comparing the frequencies of the two beams (Fig III-1 and Fig. III-2) with the frequencies of the coupled system (Fig. III-4), it is possible to identify the main contributions of each subsystem to the dynamics of the assembled system. The identification of each mode of the assembled system has been performed with the help of the numerical modal analysis, which allows to identify the modes of the coupled system (section II, Tab. II-4, Tab. II-5).

The modes of the coupled system are slightly different from the modes of the beams: once the beams are put in contact, the upper beam is subjected to two constraints, one from the displacement imposed to its clamped edge, the other from the contact with the lower beam. The 1st bending mode of the upper beam (beam1) shows, under the contact conditions, a higher frequency in the coupled system; the deformation shape is changed, with the maximum deflection at the center of the beam and not at the “free end”, as for the uncoupled beam.

The other modes are subjected to a shift to higher or lower values with respect to the increasing or decreasing of the stiffness under the imposed contact condition. The bending modes of the lower beam, for example, have a higher frequency in the coupled system, caused by the contact with the upper beam which increases the respective stiffness (under the imposed test conditions).

A further numerical investigation has been carried on for identifying the frequencies of the coupled system at about 1800 Hz, 4500 Hz and 8000 Hz (Fig. III-4 underlined by the red circles). From the complex eigenvalue analysis (sections II-3.1 and IV-1.1) with a bidimensional (2D) model, these frequencies can not be retrieved. Then, a tridimensional (3D) model, under the same boundaries conditions, has been developed, showing that these modes are characterized by a transversal deformation of the upper and lower beam (Fig. III-5), which couldn't be simulated by the 2D model.

This explains also the low amplitude of these peaks in the system vibrational response, because the friction forces excite the system mainly along the directions perpendicular to its deformed shape.

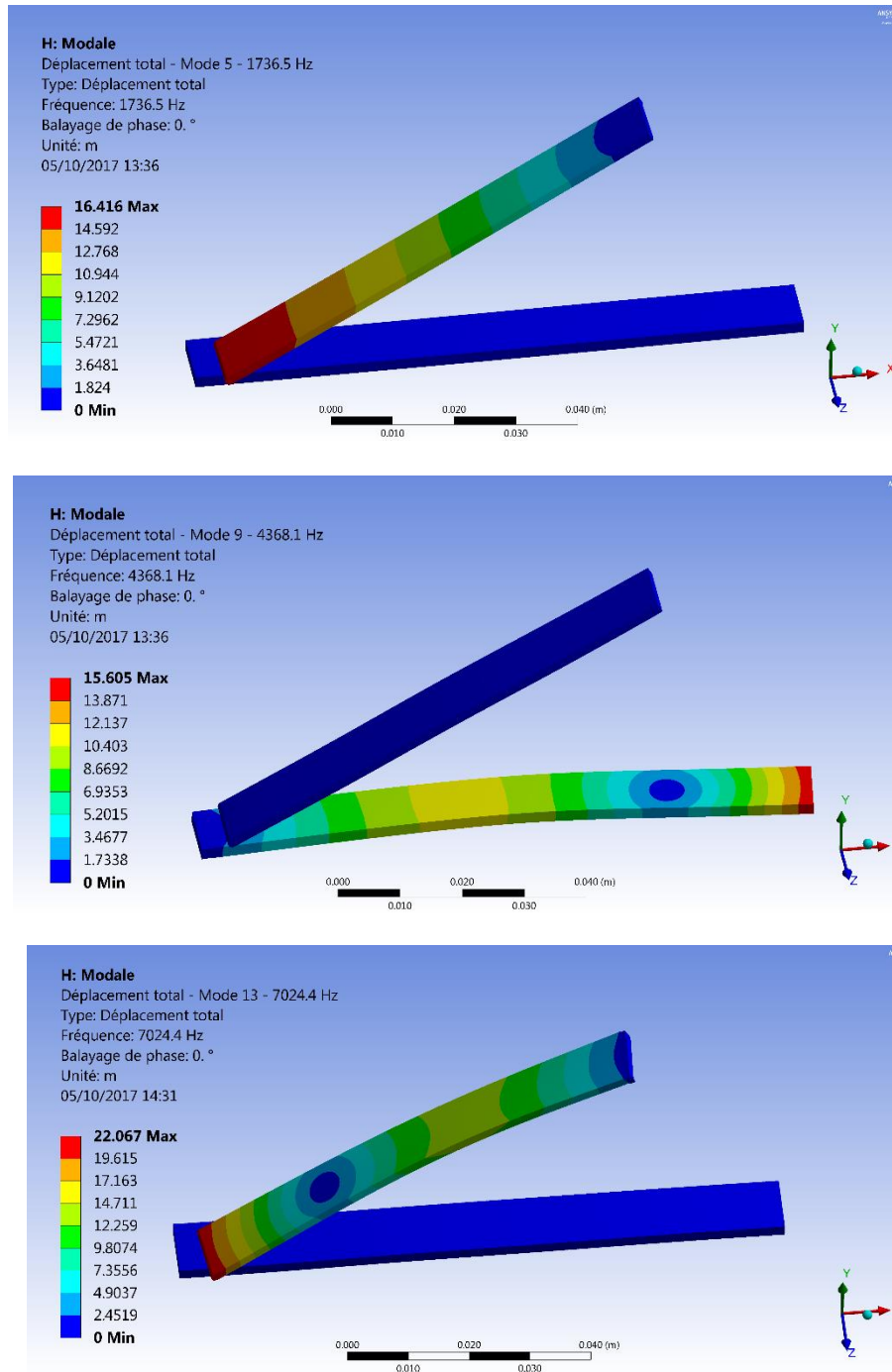


Fig. III-5: Deformation shape for the out of the plane modes of the coupled system retrieved with a tridimensional model

III-2. Reproduction of FIV

This section has the objective to describe the analysis in the time and spectral domain of the Friction-Induced Vibrations reproduced on the test bench.

The experimental tests have been carried on by following the same protocol: the contacting surfaces have been polished and cleaned as described in section II-3; Then, the beams are put in contact, applying a vertical displacement to the upper beam, until the reaching of the required normal load, monitored by the force transducers (Fig. III-6b); After the loading phase, a constant horizontal velocity is applied to the lower beam placed on the upper base of the compliant device.

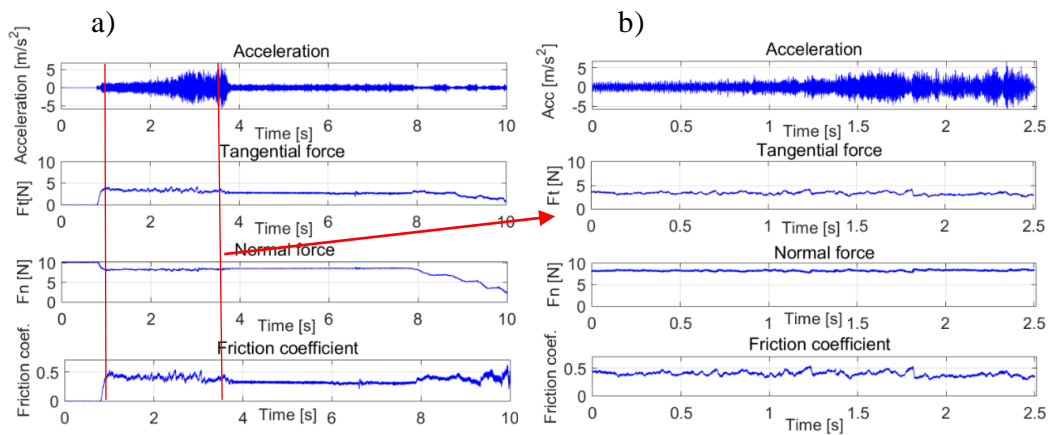


Fig. III-6: a): Response of the experimental system: acceleration of the upper beam, tangential force (Ft), normal force (Fn) and friction coefficient; b) SELECTION on the stable sliding phase.

Fig. III-6a shows the time evolution of four signals: the acceleration measured by the accelerometer placed on the upper beam; the tangential force Ft and the normal force Fn, measured by the force transducers; the friction coefficient, which is retrieved as the ratio between the tangential and the normal forces.

During the measurements, the vertical displacement of the upper beam is maintained constant, and the normal force has a small variation during the sliding, due to the deflection of the lower beam. To ensure stable boundary conditions at the contact interface, a selection of the signal is operated for the analysis: only the part of the signals when the contact point stays close to the clamped edge has been considered, so that the variation of the contact force, due to the deflection of the lower beam, can be neglected. Fig. III-6b presents the selection of the signal, on 20 mm of sliding, during which the tangential and the normal force are constant. All the analyses reported in the following refer to this selection of the

signals. For the reported case, the normal force is about 8N, and the friction coefficient is equal to 0.45.

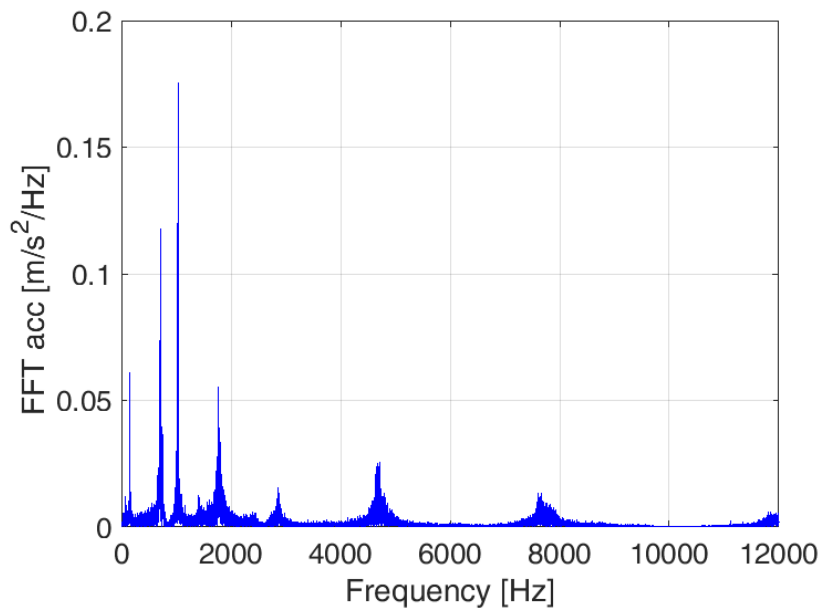


Fig. III-7: Spectral evolution of the acceleration in term of FFT. Surface roughness R320, sliding velocity 8 mm/s, normal load 8 N.

The spectral evolution of the acceleration, recovered from the 20mm of sliding, is illustrated in Fig. III-7. Its trend is characterised by a high energy in the low frequency band, between 100 Hz and 2500 Hz. The associated peaks represent the natural frequencies of the assembled system with most of the energy content. After this frequency band, there is a decreasing in the amplitude of the system response, due to a decreasing of the excitation spectrum generated at the frictional interface. The peaks decrease until the achievement of a negligible amplitude in the band between 8 and 12 kHz.

Before each test, the surface of the beam has been subjected to a polishing protocol (see section II-3) to obtain a specific surface roughness: the sliding surface of the lower beam and the tip of the upper beam are treated with the same sandpaper. Three roughness have been tested, each sandpaper being characterized by a specific Ra [101].

The polishing treatment has been repeated after every sliding of the beams to assure reproducible surface topography for each measurement, guaranteeing so the same contact conditions for the whole experimental campaigns.



Fig. III-8: a) Measure of the vibrational velocity of the upper beam with the accelerometer, b) Measure of the vibrational velocity of the upper beam without the accelerometer

As described in Chapter 2, the accelerometer placed on the upper beam has been used to measure the Friction-Induced Vibrations generated by the excitation from the frictional contact. To assure that the presence of the accelerometer doesn't affect the measures, a further investigation has been carried on. A laser vibrometer (red point in in figure III.10) has been employed to measure the vibrational velocity of the upper beam during the sliding motion and two configurations have been tested: with and without the presence of the accelerometer.

Fig. III-8a and Fig. III-8b present the measurements on the TRIBOAIR test bench with and without the presence of the accelerometer.

Fig. III-9 and Fig. III-10 shows the superposition of the spectral (Power Spectral Density) and time evolution of the measured velocity for the two configurations: the red curve represents the measured velocity with the accelerometer, in blue without it. The curves, for both the time and spectral domain, are in good agreement, demonstrating that the presence of the accelerometer doesn't influence the measurements of the Friction-Induced Vibrations.

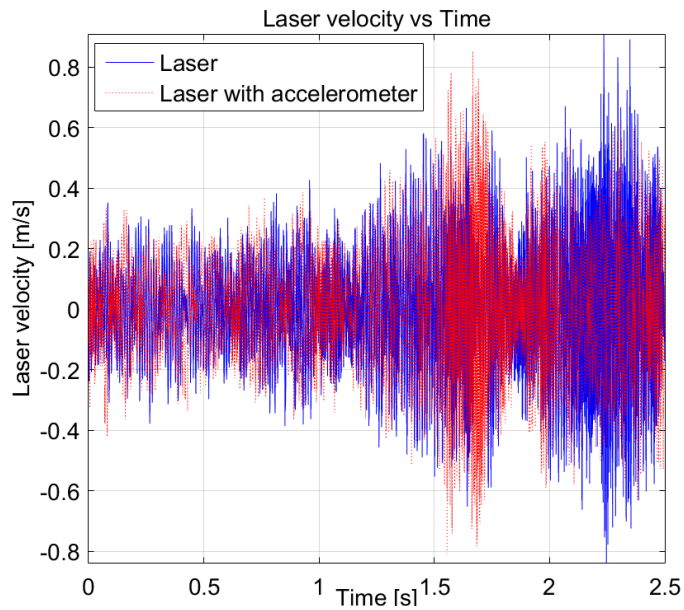


Fig. III-9: Superposition of the vibrational velocity with and without the accelerometer

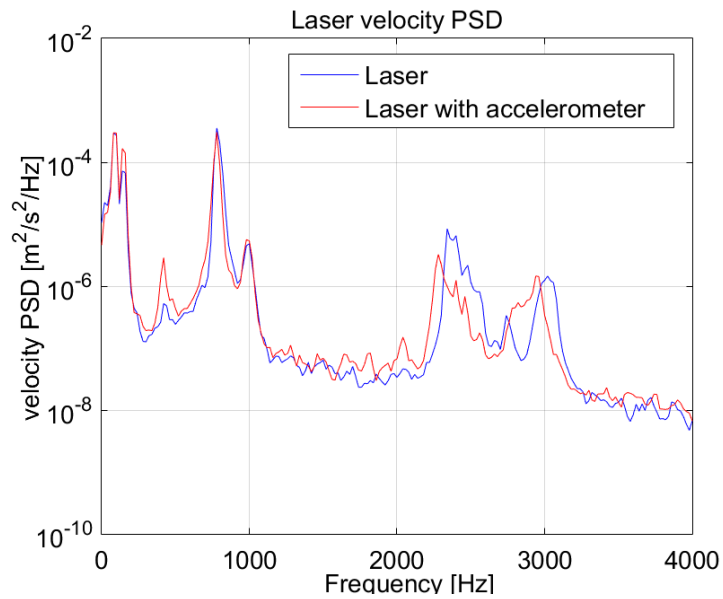


Fig. III-10: Superposition of the PSD of the vibrational velocity with and without the accelerometer

III-3. Parametrical analysis

In this section, the parametrical campaign is described and the major results are presented, focusing on the bonds between the evolution of the Friction-Induced Vibrations and the contact parameters.

The experimental campaign has been carried on choosing as parameters the contact normal load F_n , the sliding velocity $v(t)$ and the surface roughness. 10 normal loads have been tested, between 0.2 and 20 N. For each load, 3 sliding velocities have been used, for each surface roughness. Each test condition has been repeated at least 3 times for verifying the robustness/reproducibility of the results, even on different test benches (TriboTouch and TriboAir namely).

Every measurement is labelled with the respective normal load and sliding velocity: the measurement N8v8 refers to the measurement with a normal load of 8N and a sliding velocity of 8mm/s.

In the following paragraphs, the evolutions of the Friction-Induced Vibrations with the sliding velocity, the normal load and the surface roughness are presented.

III-3.1 Acceleration Root Mean Square (RMS) vs sliding velocity

The RMS of the measured acceleration has been calculated for 10 normal loads, from the lowest charge at 0.2N up to the highest one at 20N, and for 3 values of the sliding velocity: 4 mm/s, 8 mm/s and 32 mm/s.

Fig. III-11 shows the evolution of the acceleration RMS with the sliding velocity for each value of the normal load. All the curves present a monotonic, almost linear, increasing trend between the acceleration and the velocity. An increase in the velocity causes indeed a growth in the power injected into the system through the contact surface, determining higher values of the induced vibrations. In fact, considering the energy balance and the energy flows at the contact [13], the Friction-Induced Vibrations are due to a quota part of the energy at the contact, which is reinjected into the system in the form of induced vibrations. Increasing the power at the contact, by increasing the velocity, has, as a consequence, the increase of the induced vibration amplitude too.

Fig. III-11 presents the results for only a surface roughness, R120, but the same increasing evolution has been recovered for the other roughness, R320 and R800.

This behavior of the RMS acceleration is of main importance for the definition of the relationship between the perturbative term of the friction law and the sliding velocity, as presented in section V-3.2.

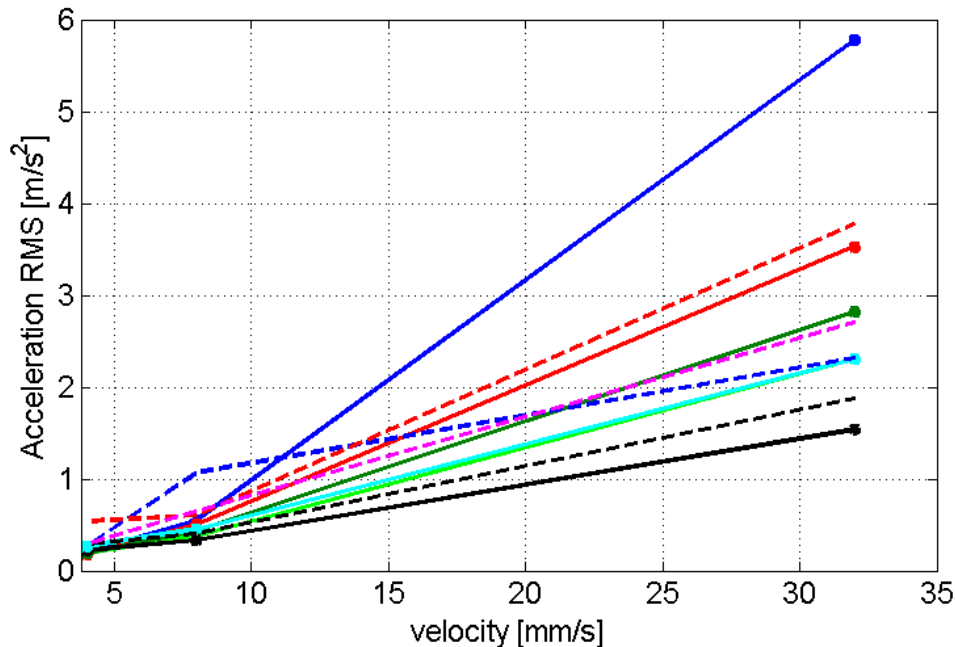


Fig. III-11: Acceleration RMS of the induced vibrations vs sliding velocity, for the R120 roughness

III-3.2 Acceleration RMS vs normal load

The second contact parameter analysed during the experimental campaign corresponds to the normal load. The normal load is measured by the force transducers positioned under the support of the lower beam. The measured values have a quasi-static connotation, representing their trend during the frictional tests. In fact, the mass of the clamping blocks of the support filters the dynamic component (higher frequencies) of the forces.

Fig. III-12 shows the trend of the acceleration RMS with the increasing of the normal load. Three groups of curves can be distinguished: in blue the curves with slow sliding velocity, 4mm/s; in red the curves with a sliding velocity of 8mm/s; in green the curves with high velocity, 32 mm/s. Each group is composed by 3 curves, one for each surface roughness.

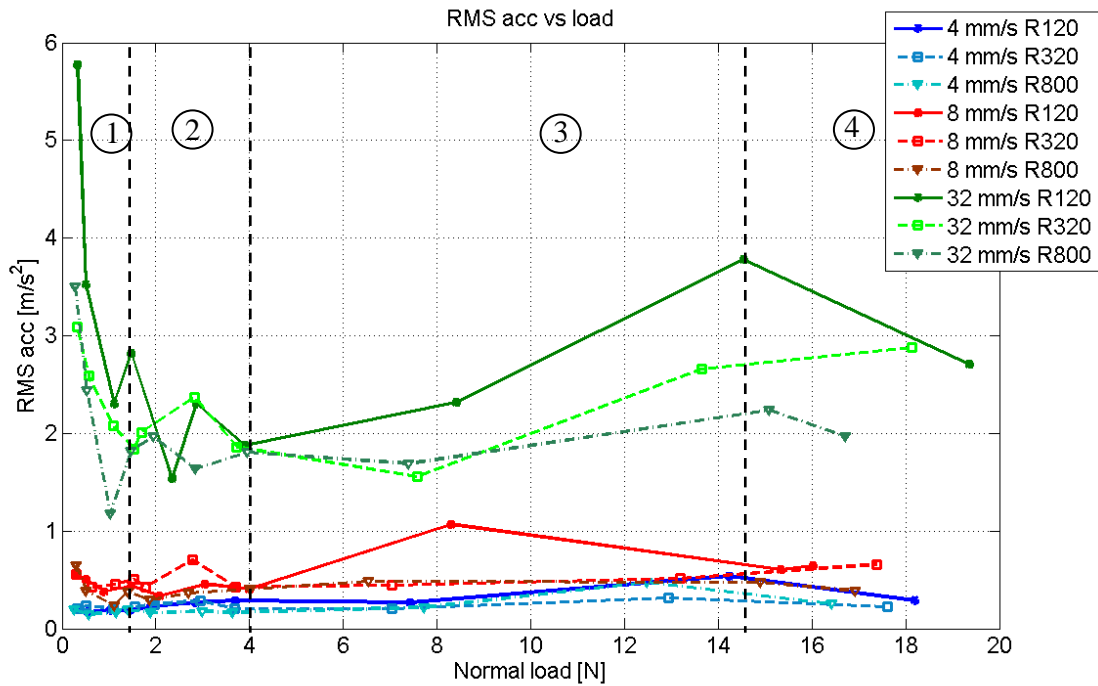


Fig. III-12: Acceleration RMS vs normal load, superposition of the evolutions for 3 roughness and 3 sliding velocities: in green the curves for 32mm/s, in red for 8mm/s, in blue for 4mm/s

The evolution, for every curve, can be subdivided in four main zones:

1. Zone 1: [0.2-1] N
2. Zone 2: [1-4] N
3. Zone 3: [4- 14.5] N
4. Zone 4: [14.5- 20] N

The four zones are characterized by different boundary conditions and phenomena occurring at the contact interface.

Zone 1:

The first zone is characterized by low values of the contact force, the upper beam undergoes to a weak constraint at the contact with the lower beam, determining an almost clamped-free condition (*weak contact condition*). Under this condition, the contacting edge of the upper beam is free to vibrate, it is excited by the impacts between the surface asperities and the system shows high amplitudes of vibration.

Zone 2:

The second zone, from 1N to 4 N, is a transition zone, where the amplitude of the induced vibrations varies in a non predictable way with the increase of the normal

load. This phase has been further investigated by choosing a finer rate of variation of the normal load.

The chosen rate of variation for the normal load is of 0.25N. For each load, the same measure has been carried on at least 3 times, to evaluate the mean value and the standard deviation.

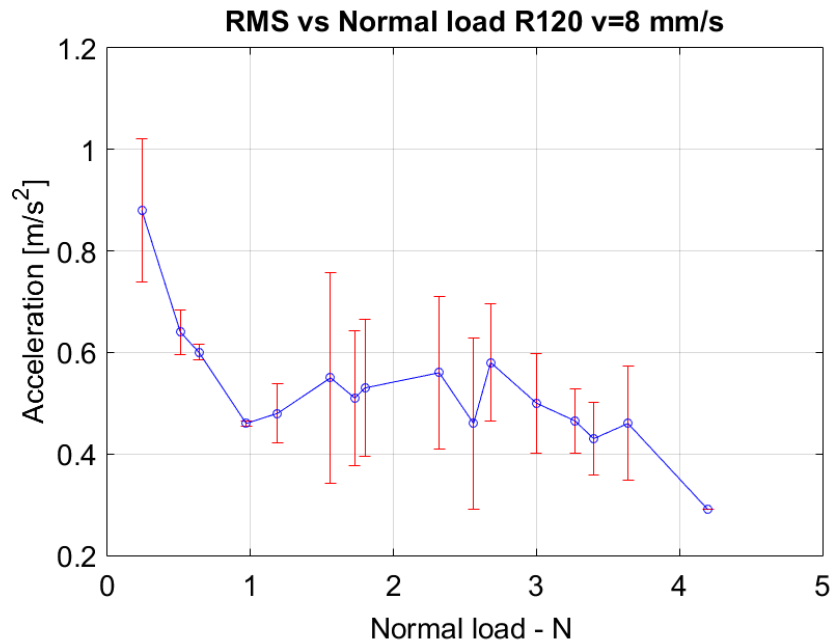


Fig. III-13: Acceleration RMS vs normal load for low normal loads. The red lines represent the deviation of the measures from the mean value obtained with the same load conditions.

Fig. III-13 presents the obtained trend of the induced vibrations: the blue curve being the mean of the performed tests for each value of the load, with the respective standard deviation represented by the red intervals.

Comparing the trend of the mean value of the acceleration RMS with respect to the load, i.e. the trend of the blue curve, with the amplitude of the deviation recovered from the repetition of the tests (i.e. the amplitude of the red bars), it can be noticed that, in the transition zone (between 1N and 4N), the deviation is larger than the variation of the trend of the curve. This means that in this zone the repeatability of the measure is not guaranteed, and the amplitude of the friction-induced vibrations varies largely for the same load condition. This behavior can be attributed to the transition values of the contact load and of the respective boundary conditions for the system, passing from almost uncoupled condition at the contact (up to 1N) to full coupled conditions at the contact (from 4N). In this

intermediate range, the contact conditions, due to the presence of the surface roughness, change drastically with small variations of the parameters, leading to the large deviation of the vibrational response amplitude of the system.

Zone 3:

The third zone, from 4N to 14.5N, is characterized by a full coupling at the contact. The acceleration increases with the increasing of the normal load. In this zone, an increase in the normal load corresponds to an increase in the power exchanged at the contact. Consequently, the amplitude of the friction-induced vibrations increases with the load.

Zone 4:

With a further increase in the normal load, the roughness at the contacting surface of the lower beam experiences a severe plasticization during the passage of the tip of the upper beam. The asperities of the surface roughness, instead of exciting the system, are plasticized by the high contact pressure and, consequently, a decreasing evolution of the acceleration RMS with the load is observed within the last zone, from 14.5 N to 20 N.

Considering these results with respect to the literature, the first zone, under low contact loads, can be described as the zone of *weak contact*, where the so-called roughness noise, i.e. the dynamic excitation from the impacts between surface asperities, excites the vibrational response of each subsystem. On the contrary, within the zone characterized by high loads the system is fully coupled and it undergoes instead in *strong contact*. In the intermediate zone (zone 2) there is a transition phase in which the system pass from weak to strong contact, and the system response varies between the two contact conditions.

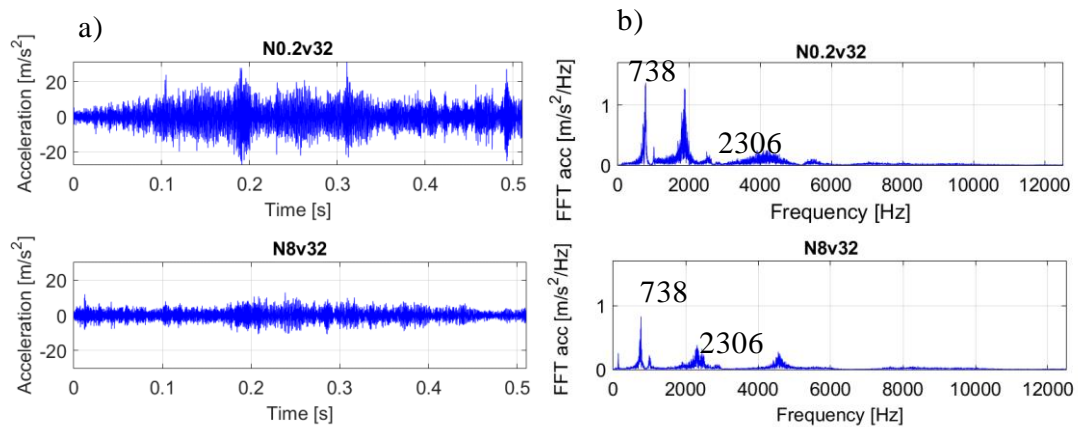


Fig. III-14: Acceleration signals (a) and corresponding FFT (b) for $v=32$ mm/s and two normal loads: from the top to the bottom 0.2N, 8N, (R120).

Fig. III-14 shows the evolution of the acceleration with an increase in the normal load: it presents the time (a) and spectral (b) trend for two loads: 0.2N, which belongs to the *weak contact* zone, and 8N, in the *strong contact* zone.

With the low load (0.2N), the weak coupling at the contact interface produces a spectral distribution peaks due to the frequencies of the uncoupled system; increasing the normal load and achieving the clamped-clamped conditions for the upper beam, the spectrum tends to have peaks at the natural frequencies of the coupled system (Fig. III-14b).

This analysis allowed for showing that increasing the normal load the dynamics of the system pass from the weak to the strong contact condition.

III-3.3 Acceleration RMS and spectra vs surface roughness

This section describes the bonds between a change in the surface roughness and the dynamic response of the frictional system.

A different surface roughness implies a different surface topography. The contact conditions are then directly influenced, determining a diverse degree of coupling between the beams and a different spectrum of the dynamic excitation coming from the interaction between the surface asperities.

An increase in the surface roughness causes a lower number of greater asperities that engage the contact, generating a lower degree of coupling, together with more energetic impacts between the impacting asperities. As a consequence, larger vibrations of the system are recorded (Fig. III-15 and Fig. III-16).

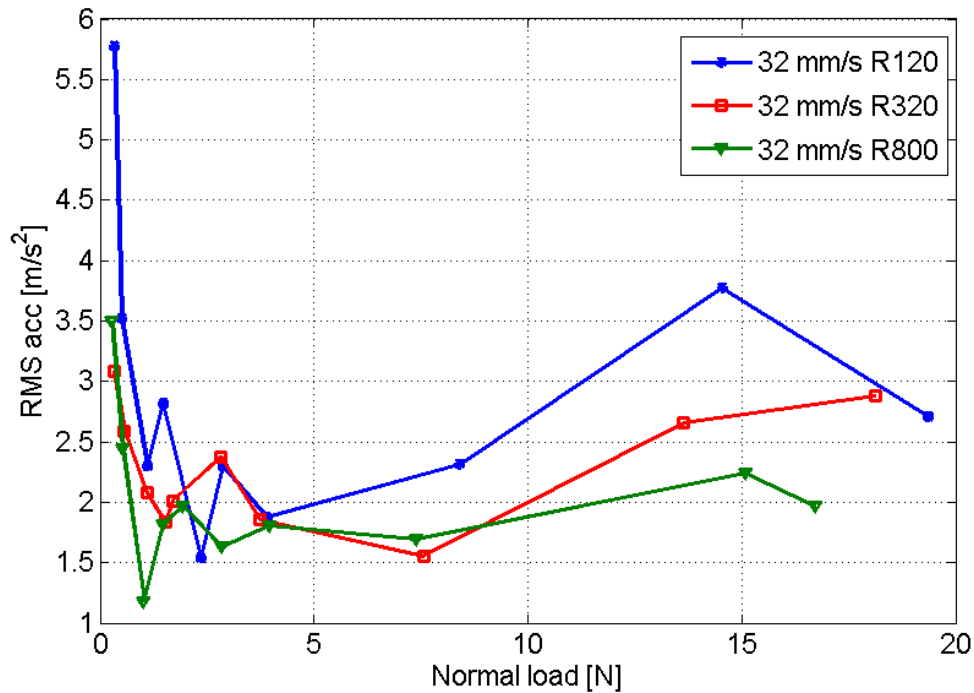


Fig. III-15: Superposition of the acceleration RMS for the three roughness, with a sliding velocity of 32 mm/s

The opposite behaviour is showed for the smoothest surfaces: a surface characterized by smaller asperities implies a more uniform distribution of the contact on the surface and less energetic impacts, reducing the vibration amplitude of the frictional system.

Fig. III-15 shows that the highest amplitudes of FIV are achieved with the highest surface roughness, i.e. R120. Moreover, the decrease in amplitude for the highest loads, due the plasticization of the roughness, is more pronounced on the surface with highest roughness too.

Analysing the evolution of the acceleration RMS with the sliding velocity, Fig. III-16 presents the superposition of the RMS for the three roughnesses with respect to the sliding velocity. The normal load is maintained constant to a value of 0.5N, i.e. in weak contact conditions. Increasing the sliding velocity, the power at the contact is increased, generating a growing amplitude in the Friction-Induced Vibrations. The trend is similar for the three roughness, with an almost linear increase of the vibration amplitude with the sliding velocity.

Fig. III-17 presents the superposition of the vibrational signal evolution for the three roughnesses, in the time (a) and spectral domains (b); the sliding velocity is fixed at 8 mm/s and the normal load at 8N.

The excitation at the contact interface is due to the collision and ruptures between the asperities, behaving as micro-shocks. The level of excitation is directly tied to the number of shocks in unit time, the velocity of the collisions and on the average load on the single asperity. An increase in the surface roughness causes a decrease in the number of asperities in contact per unit area, but, at the same time, a raise in the load on each asperity, releasing more energy from their detachment or impacting. Indeed, Fig. III-17b shows a spectrum with an increasing amplitude passing from R800 to R120-

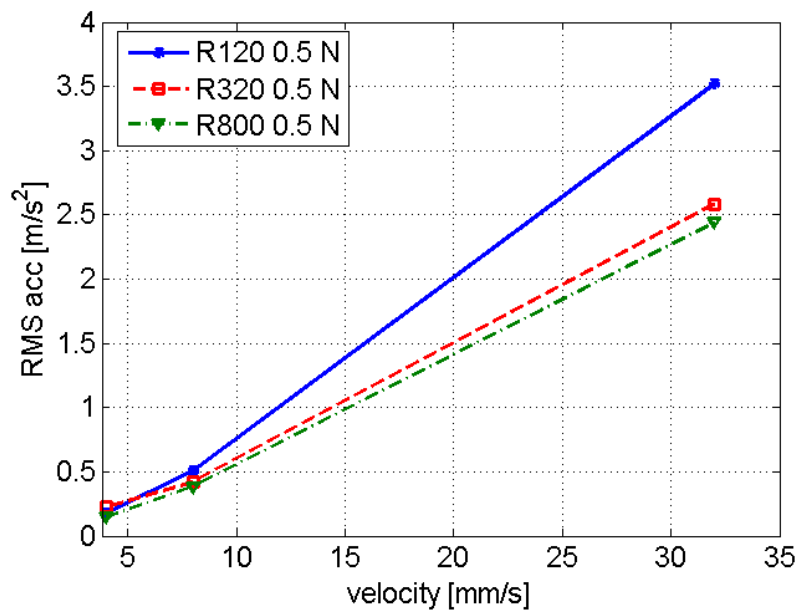


Fig. III-16: Acceleration RMS vs sliding velocity for the three different roughness (N=0.5N).

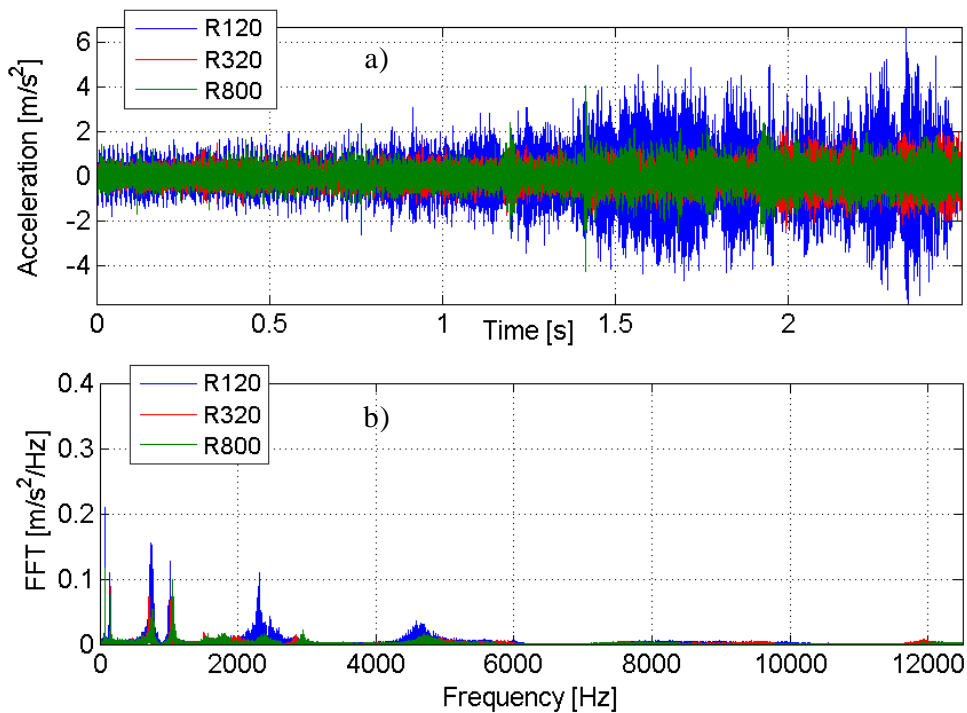


Fig. III-17: a) Superposition of the time evolution of the acceleration for the three roughness, b) Superposition of the acceleration FFT. Normal load 8N, sliding velocity 8mm/s

III-4. Conclusions

In this section, the parametrical experimental analysis has been presented. Within the whole experimental campaign, the effects of three main parameters have been focused; the evolution of the acceleration RMS and spectra has been investigated as a function of the sliding velocity, the normal load and the surface roughness.

The following main conclusions can be drawn:

- The spectra of the Friction-Induced Vibrations highlight the broadband feature of the excitation from the contact interface, which excites the system response up to about 4-5 kHz. The system responds with its natural frequencies, which can slightly vary when passing from weak (uncoupled) to strong (coupled) contact conditions.
- The system response showed a strongly nonlinear behaviour with respect to the contact load. This is mainly due to a change in the degree of coupling between the two subsystems in contact. Four zones can be distinguished with a change in the normal load:

- (i) for low contact load, the frictional system is under weak contact conditions, and the response of the system, excited by the roughness at the contact interface, reveals a high amplitude of vibration;
 - (ii) A transition zone is observed when increasing the load, where the contact condition passes from the weak to the strong coupling;
 - (iii) increasing the applied normal load, the coupling condition becomes a strong contact condition. The system responds with the dynamics of the coupled system and with lower amplitude, due to the increased constraint. Increasing the load the amplitude increase with the increase of the power;
 - (iv) A further increase in the normal load, after the reaching of the strong contact conditions, causes a plasticization of the contact area, generating a decrease in the vibration amplitude.
- Analysing the evolution of the acceleration with the sliding velocity, an almost linear trend is established between an increase in the sliding velocity and the amplitude of the induced vibrations. This behaviour is mainly attributed to the increase in the power transferred at the contact with the increase of the sliding velocity.
 - The last investigated contact parameter, the surface roughness, plays a fundamental role for the amplitude of the excitation from the contact, due to the different energy content of the local impacts and ruptures between asperities, which excite the system response. A higher surface roughness determined less contact points, but more energetic, showing higher amplitude of the Friction-Induced Vibrations.

These preliminary experimental results on the effect of the main contact parameters, together with the analysis of the time and frequency features of the Friction-Induced Vibrations, are the basis for the introduction and validation of the perturbative term of the friction law. The aim is to reproduce numerically the contact dynamic excitation and the consequent response of the system, i.e. the FIV.

IV Numerical analysis

This chapter presents the numerical simulations carried on to reproduce the frictional and vibrational response of the system under relative sliding. The objective is to reproduce numerically the experimental tests presented in the previous Chapter. The comparison between numerical and experimental Friction-Induced Vibrations will allow for highlighting the drawbacks of classical frictional transient simulations.

The chapter is organized as follows.

Sections IV-1.2 presents the complex eigenvalue analyses (CEA) carried out on the system. A preliminary CEA has been performed to determine the dimensions of the beams, in order to avoid the rising of dynamic instabilities. This preliminary numerical analysis of the system dynamics allowed for defining both the numerical and experimental system dimensions. The second one has been performed to update the numerical model with respect to the experimental system, by calculating the Young modulus for the layers added at the clamped edges of the beams (as described in section II-4.1).

Sections IV-2 focuses on the transient numerical simulations. For this set of transient simulations, the presence of the broadband excitation coming from the interface is neglected, and a classical Coulomb friction law is used. A parametrical numerical analysis is presented and compared with the experimental one. The comparison with the experimental results highlights the need of introducing a friction law that is able to account for the broadband dynamic excitation from the contact.

The last section of the chapter, as usual, summarizes the main conclusions.

IV-1. System dynamics by eigenvalue analysis

Two complex eigenvalue analyses have been carried on to develop a numerical model which could correctly simulate the experimental system and, simultaneously, avoid unwished contact dynamic instabilities (mode coupling).

The first analysis has been carried on in order to determine the geometrical dimensions of the beams, which assure distinct natural frequencies of the lower and upper beams. This in order to avoid a coalescence in the beam modes and the following mode coupling instability.

The second eigenvalue analysis has the objective to update the numerical model for simulating the experimental clamping conditions as close as possible.

For both the analysis the numerical model has been detailed in section II-3 and the friction coefficient, recovered experimentally, has been set to 0.45 (see section III-2).

IV-1.1 Complex eigenvalue analysis for system stability

Three different values for the distance s (distance at which the contact between the beams is engaged, Fig.II-14) have been tested in order to cover the whole sliding distance during the experiments, as shown in [100]. Choosing the beam dimensions presented in Tab. II-1, the eigenvalues of the coupled system present a negative value of the real part for each choice of the parameter s (Tab. IV-2), revealing always a stable dynamics (stable modes). Tab. IV-1 shows the system natural frequencies and Fig. IV-1 the deformation shapes for the first five modes of the system, for $s=5\text{mm}$.

As described in section II-4.1, the pre-stressed analysis brings the beams in contact and in the *sliding state* condition.

The first mode is mainly related with the oscillation of the lower beam L_1 (inset a, Fig. IV-1); increasing s , the constraint to which the beam is subjected moves towards a larger deflection of the deformed shape, rising the stiffness of the constraint and then the value of the first natural frequency.

N°	s [mm]		
	5	10	25
1	175,19	175.2	175.46
2	903,13	897.16	832.22
3	1096	1098.2	1130.8
4	2907,3	2821.2	2544.4
5	3066,3	3117.4	3290.

Tab. IV-1: natural frequencies of the coupled system for three values of s

N°	s [mm]		
	5	10	25
1	-2.390	-2.39	-2.3902
2	-2.4642	-2.4632	-2.4526
3	-2.50	-2.50	-2.5078
4	-3.18	-3.13	-2.99
5	-3.27	-3.30	-3.40

Tab. IV-2: real parts of the eigenvalues of the coupled system for three values of s

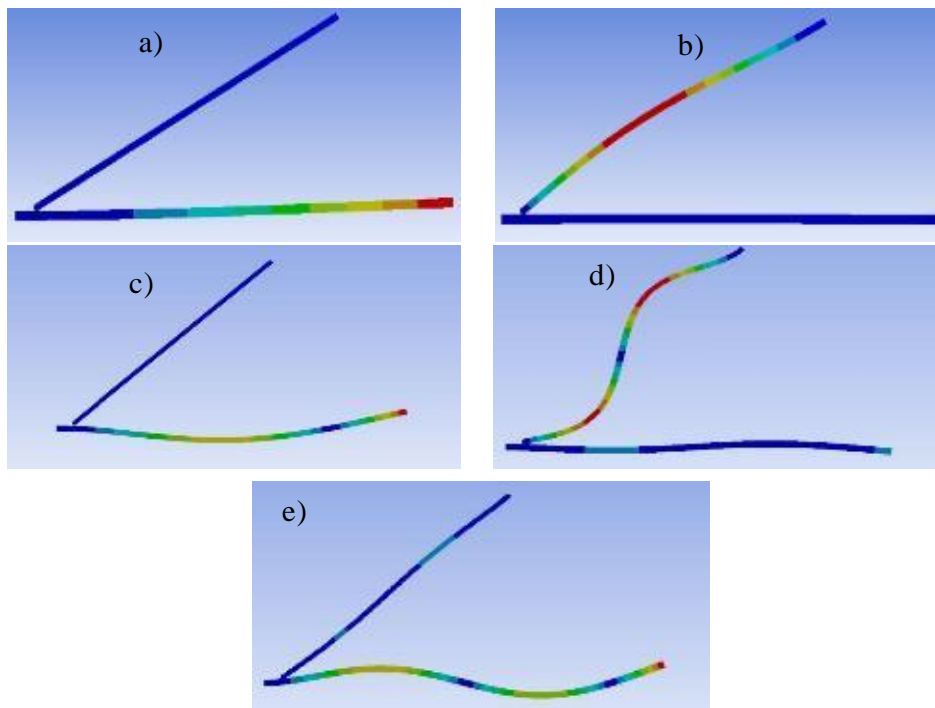


Fig. IV-1: *deformation shapes for 1st (a), 2nd (b), 3th (c), 4th (d), and 5th (e) natural frequency, with $s=5$ mm*

The second mode shows mainly the bending of the upper beam L_2 (inset b, Fig. IV-1). The constraint due to the contact becomes softer with the increasing of s , because the equivalent stiffness of the lower beam decreases and, accordingly, the value of the natural frequency decreases.

The third mode is mainly related to the second bending mode of the lower beam (inset c, Fig. IV-1) and, as for the first mode, the increase of s determines an

increasing value of the stiffness constraint, i.e. an increase of the value of the third natural frequency.

The higher frequency modes are a combination of the upper and the lower beam deformations. An increase in variable s , corresponding to the position of the contact point, can lead either an increase or a decrease in the natural frequencies with respect to the deformed shapes.

The results show that the system will not undergo in mode coupling instability during the frictional tests, while the contribution of each beam deformation into the modes of the coupled system is highlighted too.

IV-1.2 Updating of the clamping conditions

The natural frequencies of the numerical model are higher than the experimental ones and the percentage error shown in Tab IV-1 underlines a difference of about 30%. This discrepancy is due to the clamping conditions at the beam edges, which are stiffer of the clamped conditions realized in the experimental test-bench.

To overcome this problem, a complex eigenvalue analysis has been carried on, introducing a layer of softer material at the clamped edges (Fig. IV-2), in order to simulate the lost of stiffness of the experimental clamping conditions.

The stiffness of the connection has been introduced choosing a different value of the Young modulus for the first two rows of elements (Fig. IV-2), with respect to the value corresponding to the beam material properties (Tab. II-1).

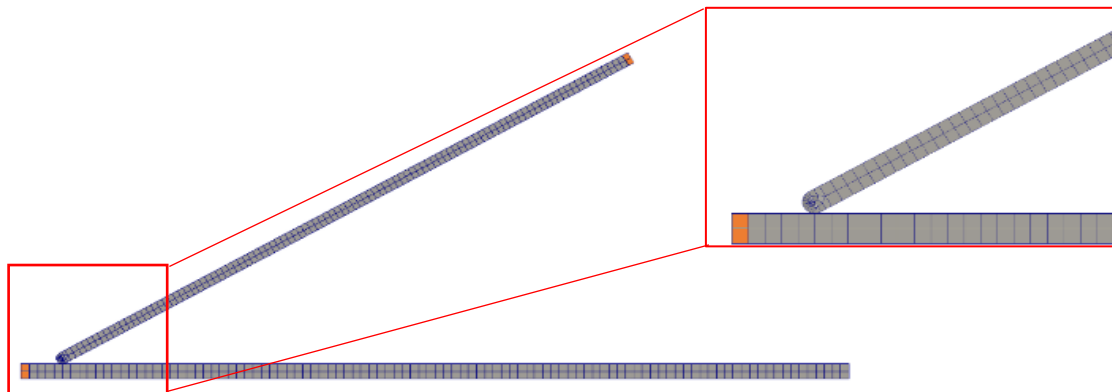


Fig. IV-2: Mesh chosen for the numerical model of the sliding beams. In orange the layers of less stiff material are underlined. The magnification on the lower beam edge, shows in orange the elements with a less stiff material.

Tab IV-2 shows the numerical frequencies obtained using a Young modulus of $2.10e10$ Pa for the clamping layers at the lower and upper beam edges. The percentage error is reduced (Tab IV-1 and Tab IV-2), staying lower than 13%. This modification has been introduced into the numerical model for the following

transient simulations in order to approach quantitatively the experimental results. This numerical model will be called in the following sections as the *updated model*.

Experimental frequencies [Hz]	Numerical frequencies [Hz]	Percentage error $\varepsilon\%$
142	175	23,24
738	903	22,36
1021	1096	7,35
2306	2907	26,06
2463	3066	24,48

Tab IV-1: comparison between the experimental and the numerical natural frequencies

Experimental frequencies [Hz]	Numerical frequencies [Hz]	Percentage error $\varepsilon\%$
142	144	1,41
738	758	2,71
1021	955	6,46
2306	2529	9,67
2463	2774	12,63

Tab IV-2: comparison between the experimental and the numerical natural frequencies obtained with a layer of less stiff material.

Once defined the geometrical dimensions of the beams and the Young modulus of the clamping layers, the simulations have been carried on: first neglecting the presence of the dynamic excitation from the contact; then introducing the new friction law in chapter V.

IV-2. Simulations without contact dynamic excitation

The first set of simulations carried on the model of the frictional system do not account for the dynamic excitation from the contact. The surface of the lower beam and the tip of the upper beam are considered flat. The simulations are carried out in a standard manner, as usual in the majority of the actual finite element software. The friction law used in this case is the classical Coulomb law:

$$\mu = \mu_{const} = 0.45 \quad \text{Eq.4.1}$$

The friction coefficient is defined by a constant value, which is a function of several material, surface, system and environmental parameters. The chosen value (0.45) for the friction coefficient, has been retrieved from the experimental measurements, as the ratio between the global tangential and normal forces (Fig. III-6b).

IV-2.1 Transient simulation of the sliding contact

The objective of the work presented in this section is the reproduction of the frictional tests and the parametrical campaign performed experimentally.

Thus, the main objective of the model is to reproduce the overall frictional behaviour of the experimental system, neglecting voluntary the real topography of the contact surfaces, in order to have a numerical model of reduced dimensions (reduced number of nodes and elements) to perform parametrical transient analyses with reasonable computational costs.

For this reason, a preliminary analysis has been performed in order to have convergence on the overall frictional behaviour of the system (normal and tangential contact forces), by maintaining a mesh size (including the contact zone) as coarse as possible. The final model is composed by 659 nodes and 442 elements.

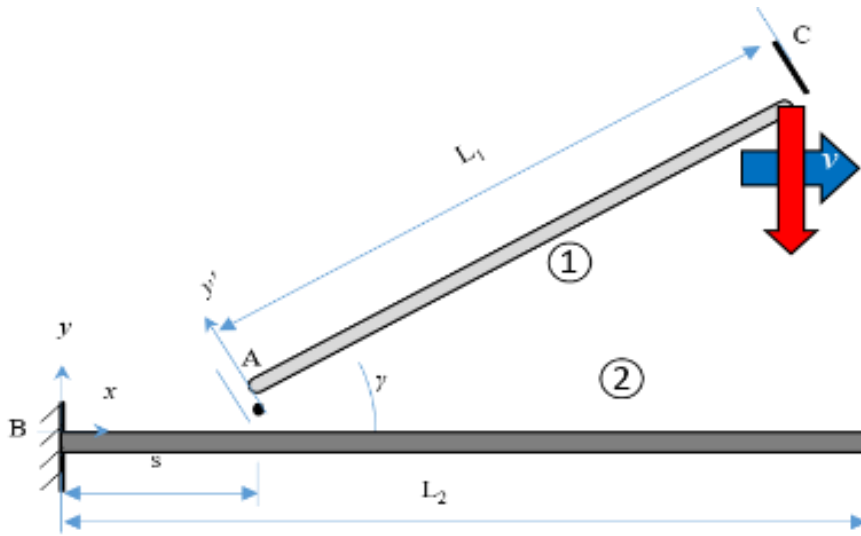


Fig. IV-3: 2D numerical model of the sliding beams

Fig. IV-4a presents the mesh used for the transient simulation, with a magnification of the mesh focused on the contact area. The two nodes underlined by red points lie in the same position of the accelerometer in the experimental campaign.

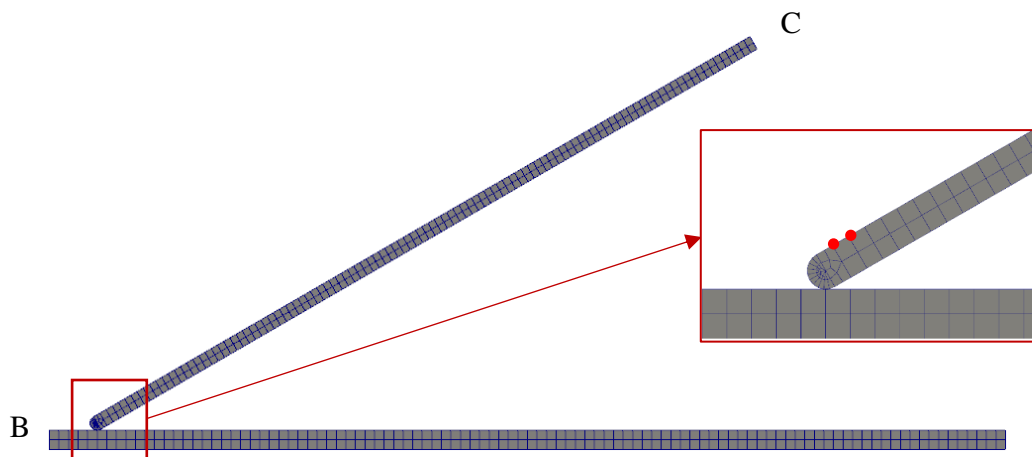


Fig. IV-4: Representation of the chosen mesh, with magnification of the mesh at the contact; The nodes underlined in red have the same position of the accelerometer in the experimental campaign.

To retrieve the dynamic response of the system, the average of the acceleration of these nodes has been considered, along the same direction measured by the accelerometer.

The protocol followed during the experimental campaign, to apply the load and the relative motion between the beams, has been reproduced in the numerical simulations.

A vertical displacement is imposed to the upper beam, to put the beams in contact until the reaching of the wished normal load. Fig. IV-5 presents the evolution of the acceleration, the normal and tangential forces, with an increasing trend of the normal load to reach the attainment of the desired load. When the beams engage the contact, an impulsive force occurs and the system responds with an impulsive response. In order to reduce the computational time, the load is imposed within a relatively short duration. Consequently, a high impulsive response is recorded. To damp the oscillations in a relative small time interval, an artificial damping is imposed at this initial stage: the α coefficient is increased of two orders of magnitude, with respect to the value retrieved by the modal analysis (section III.1), and the oscillation is damped within about 0.01s. After this initial phase, the α coefficient is decreased again to restore its real value. In such a way, the presence of artificial vibrations due to the engagement of the contact is avoided. Therefore, in Fig. IV-5, three main phases can be distinguished: i) the loading phase, in which the contact is engaged and an impulsive response is recorded; ii) a stabilization phase, during which the vibrations due to the contact engagement are fully damped; iii) the sliding phase, which is the object of the following investigation.

Fig. IV-5a shows the upper beam acceleration, which presents a first high oscillation due to the attainment of the contact with the lower beam: thanks to the increasing of the α coefficient, the oscillation is quickly damped during the stabilization phase, from 0.01s to 0.024s, when the beams are in contact but the relative sliding between them is not yet started.

In Fig. IV-5, the increasing of the tangential force and the decreasing in the normal force, due to the beam deflection, shows the begin of the relative sliding. Indeed, after the reaching of the contact with the wished normal load, the upper beam starts to slide, covering a length of 20mm, like in the experimental tests. In Fig. IV-3, v (blue arrow) indicates the constant horizontal velocity. During the sliding phase, the values of the material damping parameters, α and β , are those recovered experimentally (see section III-1).

Once the model developed, a parametrical numerical analysis has been carried on, as for the experimental campaign, choosing the same ranges of values for the

normal load and the sliding velocity. The next section shows the results from the analysis and compares the numerical results with the experimental ones, in terms of amplitude and time and spectral evolutions.

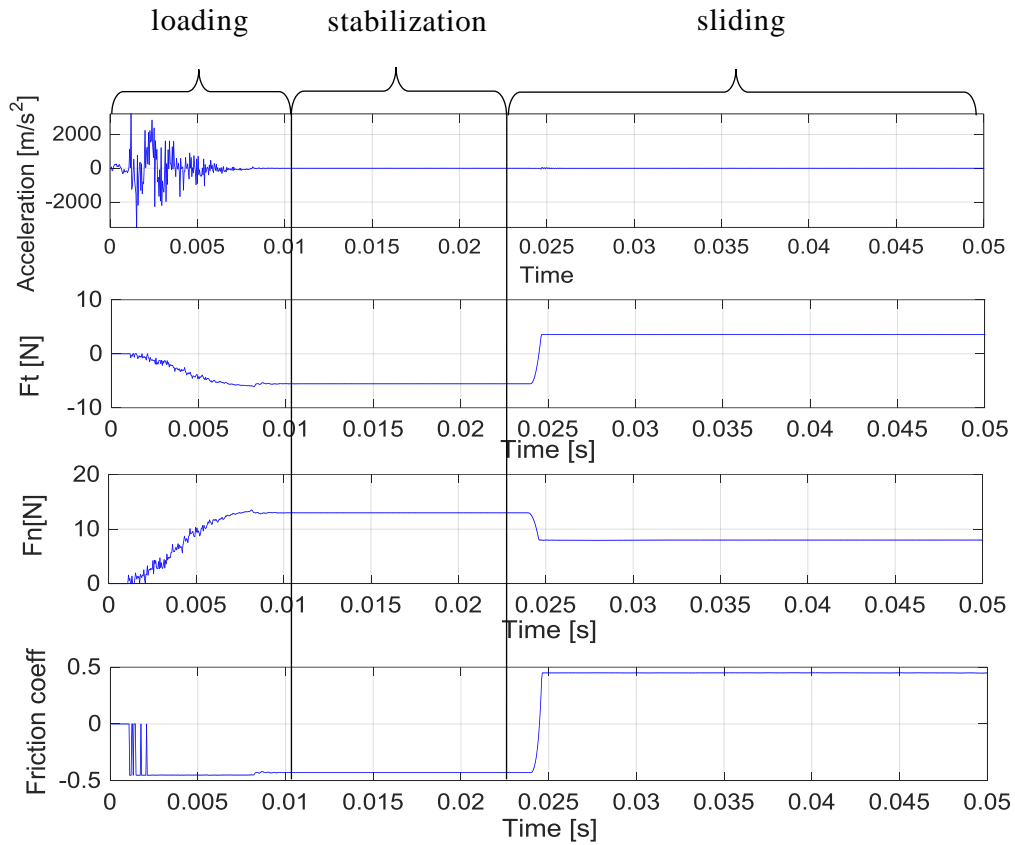


Fig. IV-5: upper beam acceleration, tangential force, normal force and friction coefficient

IV-2.2 Parametrical analysis: comparison with the experimental results

The first set of simulations has been focused on the evolution of the amplitude (acceleration RMS) of the Friction-Induced Vibrations with respect to the sliding velocity, to compare the simulated amplitudes and trends with the experimental ones. Fig. IV-6a shows the experimental trends of the RMS acceleration, when increasing the velocity from 4mm/s to 32 mm/s. For each sliding velocity several normal loads have been tested, identified by the different colours in the legend. Fig. IV-6b presents the numerical evolution for the same range of the sliding velocities and the same values of the normal load. As stated before, these first set of simulations does not take into account the presence of the excitation from the local dynamics at the contact.

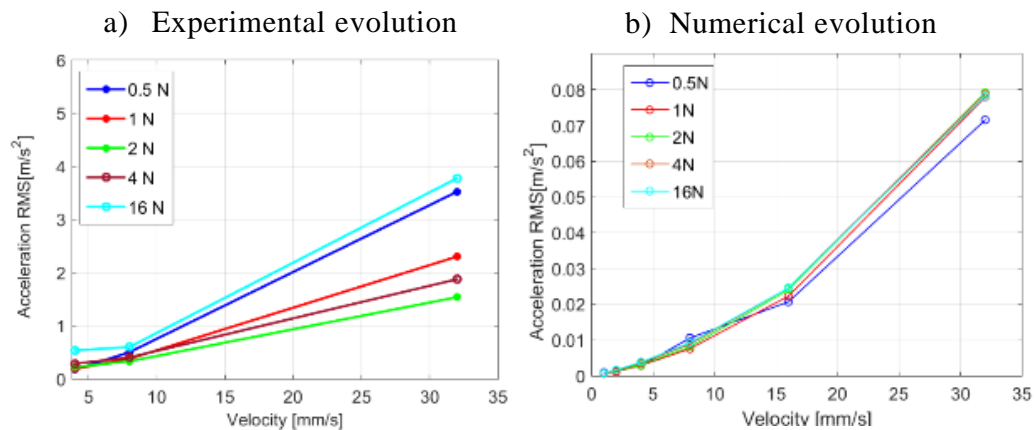


Fig. IV-6: a) experimental evolution of the acceleration RMS with respect to the sliding velocity, for a surface roughness R120; b) numerical evolution of the acceleration RMS with respect to the sliding velocity. Classical friction law with 0.45 as friction coefficient.

From the comparison between the experimental and the numerical trends, it can be highlighted that the experimental linear bond (section III-3.1) between the amplitude of the induced vibrations and the sliding velocity is reproduced numerically too. An increasing into the sliding velocity involves a growth in the power injected in the system through the contact, both for the numerical and the experimental system. The difference between them lies in the amplitude of the induced vibrations: in Fig. IV-6b the numerical amplitude is two order of magnitude lower than the amplitude measured experimentally. This discrepancy can be attributed to the lack, in the numerical model, of the dynamic excitation coming from the contact interface.

The second parametrical analysis is focused on the evolution of the Friction-Induced Vibrations with respect to the normal load: several normal loads have been tested for different sliding velocities, illustrated in Fig. IV-7a and Fig. IV-7b by the different colours of the curves.

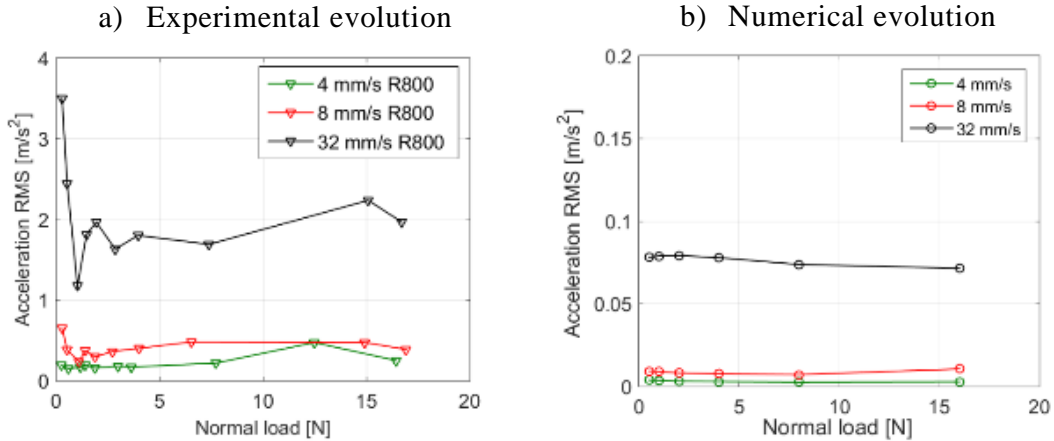


Fig. IV-7: experimental evolution of the acceleration RMS with the normal load for three sliding velocities, surface roughness R800, b) numerical evolution of the acceleration RMS with the normal load. Classical friction law with 0.45 as friction coefficient

Fig. IV-7a shows the experimental evolution of the induced vibrations. As described in paragraph III-3.2, two main zones can be identified: the first one in the band of the low normal load, which is characterised by a condition of *weak contact* between the beams; after a transition phase, at higher loads, the second one is characterized by the *strong contact* condition, until the reaching of the plasticization of the asperities (at about 15N). Fig. IV-7b presents the numerical evolution of the induced vibrations: for all the sliding velocities the absence of the surface roughness causes a more regular trend of the curves than the experimental one. While it is still possible to observe a decrease and following increase of the vibrations, due to the variation of the coupling conditions between weak and strong contact, the decreasing trend for high normal load cannot be simulated because it is not possible to recover the phenomenon of the roughness plasticization. Moreover, the lack of the broadband excitation from the local contact dynamics (local impacts and ruptures) is testified by the lower amplitude of the numerical results.

Fig. IV-8 presents the superposition between the numerical (red curve) and the experimental (blue curve) time evolution of the acceleration, of the normal and tangential forces and of the friction coefficient. From these evolutions it is clear

that, although the mean frictional conditions are the same for the numerical and the experimental tests (same values of normal and tangential forces), the vibrational response of the numerical system is not in agreement with the experimental one, showing a quite lower amplitude of the numerical Friction-Induced Vibrations. This means that, while in the physical system a part of the energy at the contact is re-introduced into the system as vibrations (FIV), and then damped by the system, in the numerical simulations this part of energy transfer between contact and system is missed.

Fig. IV-9 presents the comparison between the experimental (Fig. IV-9a) and the numerical (Fig. IV-9b) spectral evolution (Fast Fourier Transform) of the measured acceleration. The lack of the dynamic excitation from the contact in the numerical model determines two main differences between the numerical and the experimental FFTs: the numerical spectrum has an amplitude of two order of magnitude lower than the experimental one; the numerical spectrum presents only two peaks, relative to the first two natural frequencies of the system, compared to a larger frequency distribution of the experimental spectrum. In fact, the experimental spectrum shows visible peaks until 8000 Hz, due to the broadband excitation from the local contact dynamics (contact and breakage of the asperities, local ruptures, ...), which is able to re-inject energy into the system within a large frequency band.

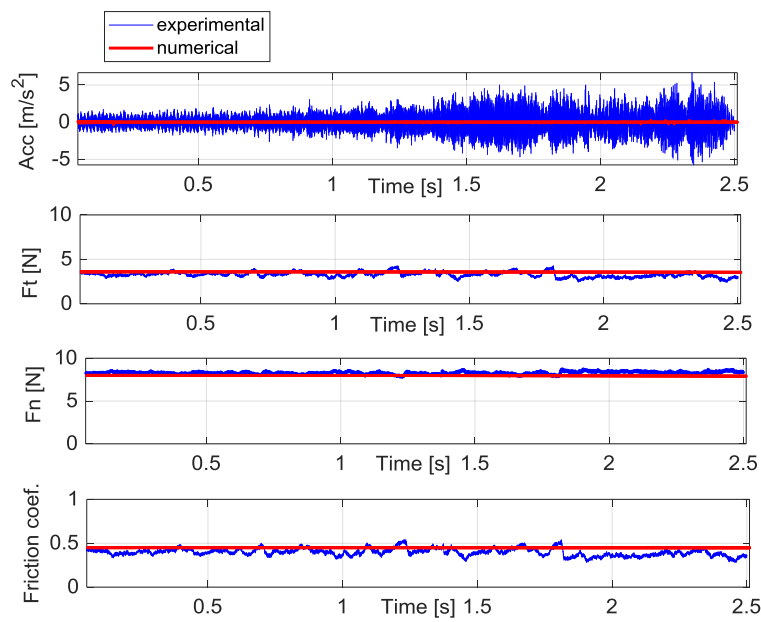


Fig. IV-8: Superposition of the numerical (red curve) and the experimental (blue curve) evolution of the acceleration, tangential (Ft) and normal force (Fn), and friction coefficient, during the 20mm of relative sliding.

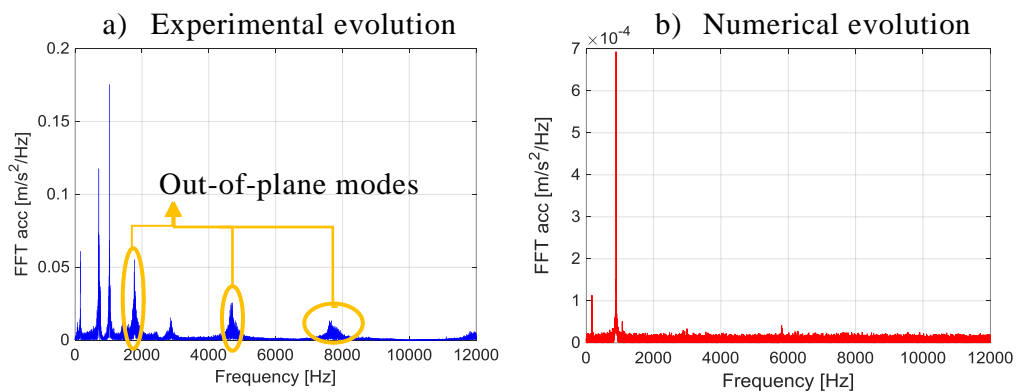


Fig. IV-9 a) experimental FFT of the measured acceleration, for 8N, 8mm/s and R320, the orange circles underline the out-of-plane modes; b) numerical evolution of the FFT of the calculated acceleration for 8N and 8mm/s.

IV-3. Conclusions

This chapter described the numerical results obtained from the transient simulations of the frictional system, in order to compare the obtained Friction-Induced Vibrations with the experimental ones.

This first analysis has been carried on without considering the presence of the contact dynamic excitation, with a classical Coulomb friction law. A parametrical analysis has been carried on, investigating the influence of the sliding velocity and the normal load on the response of the dynamic system, as did with the experimental campaign.

From the comparison between the experimental and numerical results, with the aim of simulating the contact in frictional systems, it has been showed that the absence of the contact dynamic excitation causes a vibrational response of the numerical system that differs from the one encountered experimentally

It is then clear the need of introducing the presence of the broadband excitation, coming from the contact interface, in the numerical model. A new friction law has been then introduced and further simulations have been carried on, as presented in the next chapter.

V Numerical analysis with perturbative friction law

The first sections of this chapter are reserved to the description of the methodology pursued to define the frequency content of the perturbative term introduced into the friction law, thanks to which it is possible to simulate the contact excitation and, thus, the Friction-Induced Vibrations.

In order to validate the new friction law, as a first step, simulations have been carried on considering a constant sliding velocity and a constant normal load. Different spectral distributions of the perturbative term have been tested. The simulated Friction-Induced Vibrations are then compared with the experimental ones to validate the selected spectral distribution and the proposed law.

Then, further simulations have been then carried on to introduce the effect of a change in the contact parameters, such as the surface roughness and the sliding velocity, into the friction law. The effect of a difference between the dynamics of the numerical and experimental systems is investigated too, by considering the numerical model without updating of the clamping conditions.

The main conclusions are reported at the end of the Chapter.

V-1. Determination of the perturbative term

Because of the need of taking into consideration the presence of the dynamic excitation from the contact interface, a new friction law has been introduced into the numerical model. The friction law (here recalled with Eq. 5.1) has been presented in II-4.3. In this chapter, the methodology to retrieve the perturbative term of the friction coefficient and the validation of the friction law, by comparison with the experiments, are presented.

The proposed friction law wants to introduce the effects of the presence of a broadband excitation from the contact into the overall dynamic response of the system, reproducing the Friction-Induced Vibrations measured during the experimental campaign.

$$\mu(x) = \mu_{const} + \mu_{perturbative} = \mu_{const} + A|v(t)|^b R(x) \quad \text{Eq.5.1}$$

As a first step, different signals have been tested for the $R(x)$ term, investigating the effects of the spectral distribution of the perturbative term into the dynamic response of the system and searching for the contributions of the signal that better reproduce the experimental contact excitation.

The numerical results will be showed always together with the experimental measurements, to compare the respective time and spectral evolutions.

With the sake of choosing the appropriate signal for the perturbation term $R(x)$, a preliminary analysis has been carried on, studying the effect of the different spectral contributions on the simulated induced vibrations. Three spectral distributions have been evaluated: a simple white noise; a white noise filtered by a Butterworth filter to have a spectral distribution representative of the surface roughness; finally, the spectral distribution recovered experimentally by an inverse method [102, 103, 104].

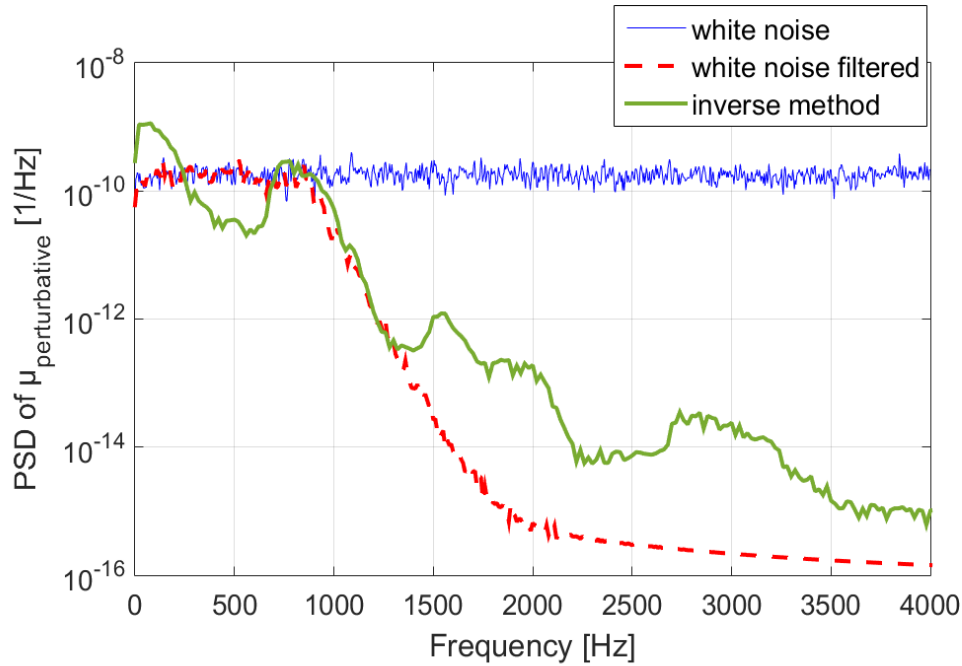


Fig. V-1: comparison between the three tested perturbative terms $\mu_{\text{perturbative}}$: white noise (blue); Butterworth filtered white noise (dotted red); from inverse method (thick green).

Fig. V-1 shows the superposition of the frequency spectra of the three signals tested for the perturbative term. The figure presents the Power Spectral Density recalculated as a function of time $R(t)$, where the transition from the space function $R(x)$ to the time function $R(t)$ is subjected to the knowledge of the sliding velocity v :

$$R(x) = R(v \cdot t) \quad \text{Eq.5.2}$$

Considering a constant sliding velocity, Eq.5.2 allows for passing from the spatial domain $R(x)$ to the time domain $R(t)$.

The first attempt for the perturbative term has been a white noise, illustrated by the blue curve in Fig. V-1 and representing a broadband frequency excitation. The

spectral distribution of this signal allows for exciting uniformly the system in the overall selected frequency range.

In a second stage, with the aim of accounting for the surface topography, the surface roughness of the contact surface has been measured with a profilometer (Altisurf 500); the considered profile has a surface roughness polished with the sandpaper R320.

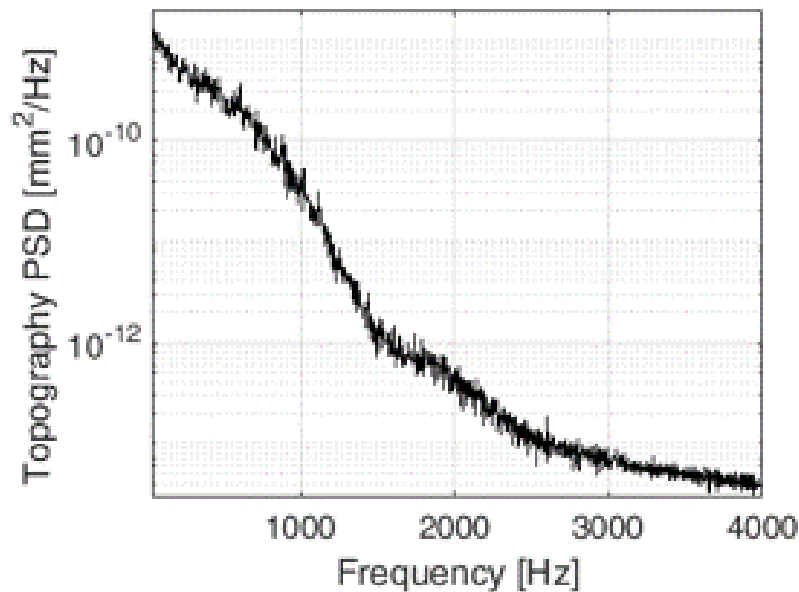


Fig. V-2: spectral representation of surface's topography for R320 sample

As for the perturbative term, the spatial distribution has been transformed in time variation of the signal, multiplying the space coordinate by the sliding velocity. From Fig. V-2, it can be seen that the major frequency content of the surface signal is between 0 and 1 kHz, with a decaying shape until about 2 kHz. To reproduce a similar frequency content in the contact excitation, a Butterworth filter has been applied to the white noise, resulting on the red dotted curve in Fig. V-1.

Then, the last step on the estimation of the perturbative term has been the exploitation of an inverse method from the measurements performed during the frictional tests, in order to have a more realistic frequency distribution of the effective contact dynamic excitation.

In the case under investigation, the contact excitation is localized at the reduced contact area between the two beams. Consequently, the contact excitation has been approximated as a punctual one and the inverse method consists here in a simple ratio between the system response and the transfer function, calculated

between the contact (excitation) point and the point of measurement of the acceleration. Thus, the spectrum of the contact excitation is recovered from the knowledge of two terms: the transfer function $H(f)$ of the system and the Power Spectral Density S_{aa} of the system response (i.e. the PSD of the measured acceleration). The $H(f)$ has been calculated by a numerical harmonic analysis computed by the means of the ANSYS software. As for the complex eigenvalue analysis, the harmonic analysis has been coupled to a previous static structural analysis to assure the sliding condition at the contact interface. The used contact algorithm is the Augmented Lagrange. Fig. V-3 shows the obtained FRF of the system.

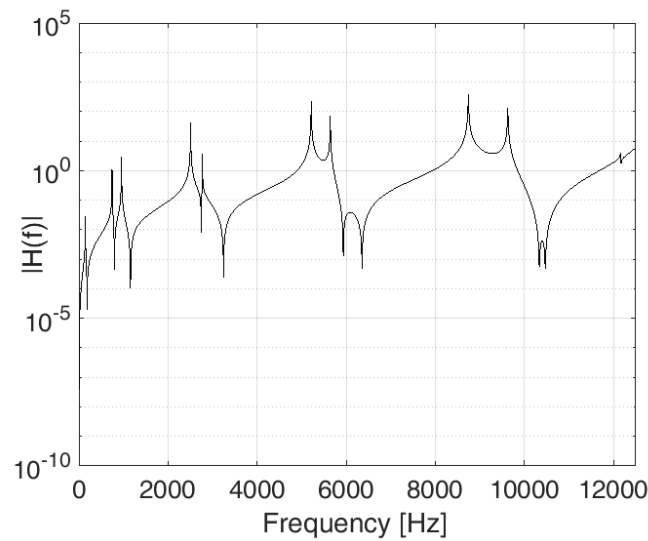


Fig. V-3: FRF obtained from a numerical harmonic analysis by the means of the Ansys software.

The S_{aa} term is the PSD of the acceleration that has been measured during the frictional tests, when the system is subjected to the excitation from the frictional interface.

$$S_{ff} = \frac{S_{aa}}{H^2} \quad \text{Eq.5.3}$$

Eq.5.3 shows the existing relationship between the PSD of the system acceleration and the transfer function used to estimate the term S_{ff} . S_{ff} corresponds to the Power Spectral Density of the excitation, which is generated by the frictional interface during the sliding. In this way, the dynamic of the system is filtered, thanks to the frequency response function, and the term S_{ff} indicates the effective spectral distribution of the broadband excitation coming from the contact.

After recovering the spectral distribution of the perturbation term, S_{ff} has been subjected to a time reconstruction with the sake to employ it as the perturbative term $R(t)$.

A code has been implemented in the MATLAB software. Few steps have been carried on to reconstruct the time evolution of the contact force generated at the sliding interface, from the spectral evolution S_{ff} . In fact, any time signal can be described as a multiplication between an amplitude factor B and a term F function of the time, which includes a phase:

$$X(t) = B \cdot F(t + \varphi) \quad \text{Eq.5.4}$$

with φ the phase and $X(t)$ the time signal.

For the signal in exam the amplitude B has been determined as the square root of the signal in the spectral domain, multiplied by the frequency resolution df [105] (reminding that S_{ff} is a discrete Power Spectral density):

$$B = \sqrt{(S_{ff} \cdot df)} \quad \text{Eq.5.5}$$

Considering the random nature of S_{ff} , the phase has been represented with a random signal characterized by a normal distribution. A sinus has been chosen for the function F , considering that, thanks to the Fourier Transform, each signal can be decomposed as sum of sinus. The obtained time signal is the following:

$$X(\tau) = \sum_{\tau=1}^{\tau=tf} (B \cdot \sin(2\pi f \cdot t(\tau) + \varphi)) \quad \text{Eq.5.6}$$

with f representing the frequency vector. The signal has been thus reconstructed as a sum of sinus functions with the respective amplitudes given by the spectral distribution.

$X(\tau)$ is then used as the perturbative term $R(t)$.

Fig. V-1 (green thick curve) presents the spectral evolution of the perturbative term retrieved by the inverse method, choosing the surface roughness R320. Comparing it with the other frequency distributions, two different ranges of frequency can be distinguished as a function of the different level of amplitude: a higher amplitude is observed in the low frequency range, corresponding to the frequency range covered by the roughness spectrum (Fig. V-2); then, the amplitude starts to decrease until a second frequency range with a still relevant amplitude. This second part of the excitation spectrum coming from the contact, at higher frequencies, can be attributed to the contribution of the micro impacts and ruptures occurring between the surface asperities and/or third body particles [73, 74], which have the form of local impulsive excitations.

V-2. Numerical results and experimental validation of the friction law

A preliminary analysis has been conducted considering a constant sliding velocity, i.e. imposing $b = 0$, and reducing the friction coefficient in the following formulation:

$$\mu(x) = \mu_{const} + A \cdot R(x) \quad \text{Eq. 5.7}$$

As described above, three signals have been analysed for the perturbative term: a white noise signal, a white noise filtered by a Butterworth filter and, finally, a signal retrieved from the experimental measures (Fig. V-1). The results from the simulations using each of the three perturbation signals are shown in the following sections, analysing the differences with the experimental results.

The normal load and the sliding velocity have been maintained constant for this set of simulations, choosing an imposed normal load of 8N and a sliding velocity of 8 mm/s. The roughness of the surface considered for this analysis is the one obtained with R320

V-2.1 White noise

The white noise has been the first signal tested to simulate the spectral distribution of the contact excitation. This signal is characterized by a constant amplitude within the whole frequency range of interest (Fig. V-4).

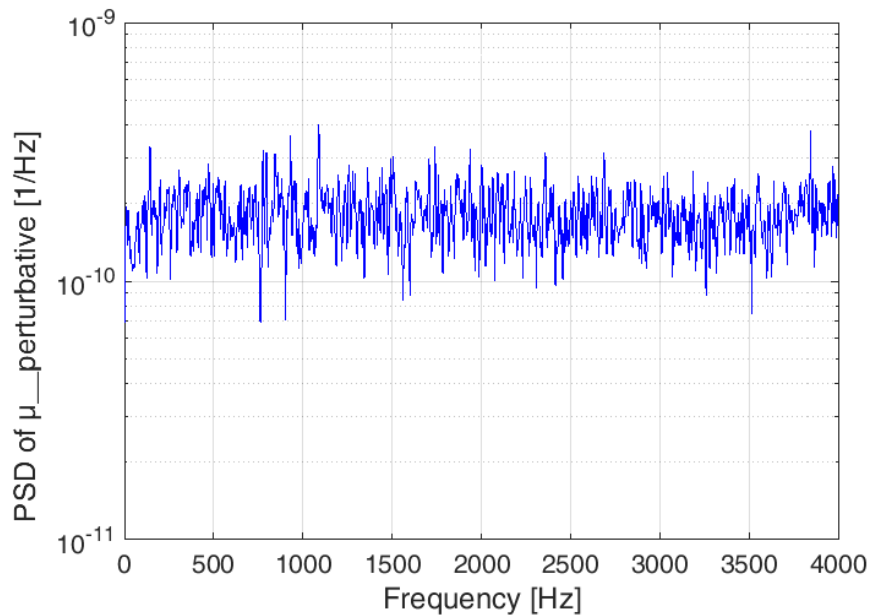


Fig. V-4: spectral evolution of the white noise, chosen as the first signal for the perturbation term $R(x)$.

Fig. V-5 shows the superposition between the numerical (red curve) and experimental (blue curve) time evolutions of forces, acceleration and friction coefficient. The normal force, the tangential force and the friction coefficient are comparable, showing the same almost constant values during the sliding phase. As in the simulations with classical friction law, presented above, the constant term of the friction coefficient allows to recover the measured values of the frictional forces. The numerical and experimental accelerations, instead, show a different behaviour both in the time and in the spectral domain. The spectral domain highlights a completely different frequency distribution of the simulated friction-induced vibrations (Fig. V-6). In fact, Fig. V-6 a) presents the numerical spectral evolution of the acceleration, where the system response is excited in a wider frequency band, revealing an overestimation of the contact excitation at higher frequencies (2-12 kHz). This behaviour is directly bonded with the use of the white noise signal, which has a constant excitation level in the whole frequency range. The experimental response, instead (Fig. V-6a), presents the major energy content in the low frequency band, 0-2kHz, showing a decreasing trend in the response amplitude from the lower to the higher frequencies. Because they are not reproduced by the 2D model, in Fig. V-6a (and in following experimental spectra) the peaks which correspond to the modes out of the plane are underlined, in order to exclude them from the comparison. The white noise,

then, is not able to reproduce correctly the vibrations induced by the simulated frictional contact.

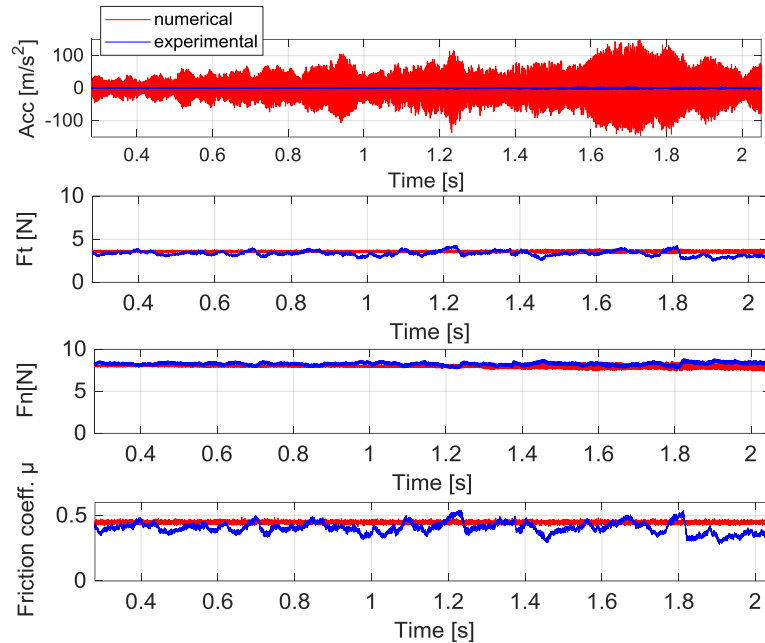


Fig. V-5: superposition of numerical (red) and experimental (blue) time evolution of contact forces, acceleration and friction coefficient. The signal chosen for the perturbative term is a white noise. Results obtained for 8 N and 8 mm/s, experimental roughness R320.

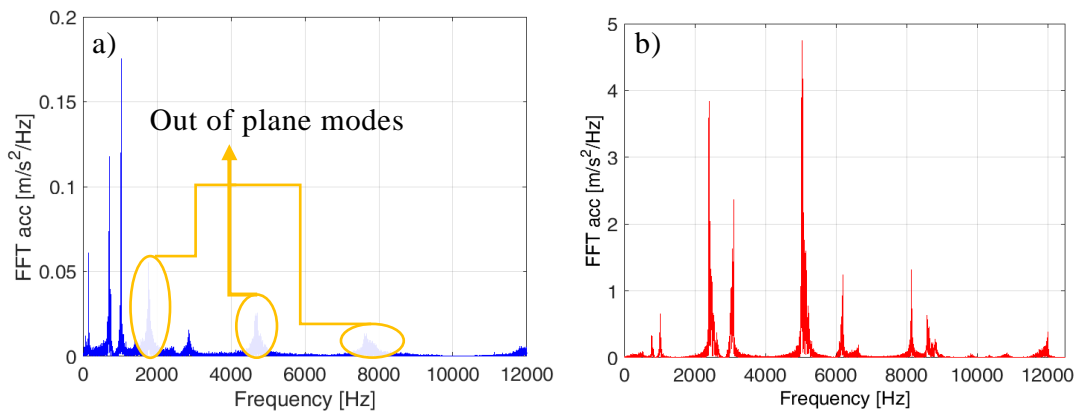


Fig. V-6: experimental a) and numerical b) FFTs of the acceleration; the signal chosen for the perturbative term is a white noise. Results obtained for 8 N and 8 mm/s experimental roughness R320.

V-2.2 Butterworth filtered white noise

The second signal employed for the perturbative term is a white noise filtered by a Butterworth filter (Fig. V-7). This kind of signal has been introduced in order to investigate the effects, into the spectrum of the simulated friction-induced vibrations, of a signal that accounts for the profile of the surface roughness.

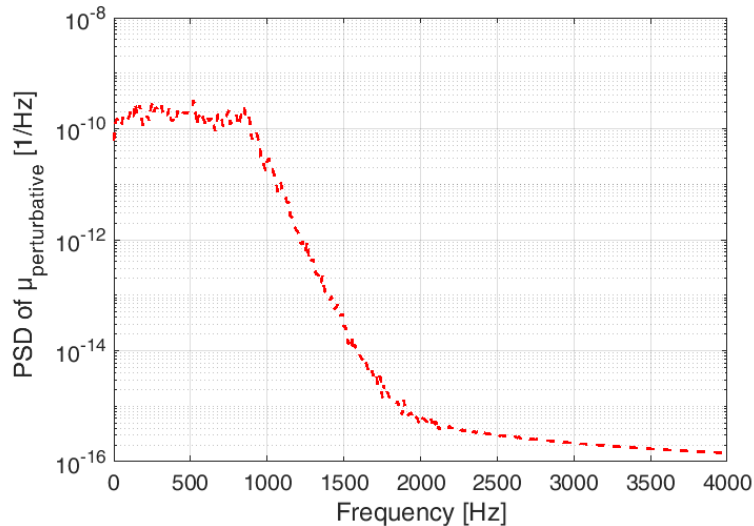


Fig. V-7: spectral evolution of the Butterworth filtered white noise, chosen as the second signal for the perturbation term $R(x)$

Fig. V-8 and Fig. V-9 show the comparison between the numerical and the experimental Friction-Induced Vibrations in term of time and frequency evolution. Fig. V-8 shows a similar time evolution of the numerical and the experimental results: the experimental and the numerical values of the contact forces are the same, the numerical evolution of the acceleration has the same order of magnitude of the experimental one and a similar evolution in time.

The spectral evolution, instead, highlights significant differences between measured and simulated induced vibrations at higher frequencies. The cut-off frequency of the Butterworth filter reduces abruptly the excitation after 2000 Hz, not allowing for the excitations of the higher natural frequencies of the system at 2.3 and 4.4 kHz, Fig. V-9b. Moreover, the experimental measurements show a broadband response of the system at higher frequencies, which is absent into the simulated acceleration spectrum. Fig. V-9b present a magnification of the

superposed spectral evolution. As always the frequencies corresponding to the out-of-plane modes have been neglected for the comparison.

Focusing on the amplitude of the FFT, the numerical spectrum shows an amplitude of the second natural frequency four times higher than the experimental one, reducing instead the amplitude of the third natural frequency. The spectral evolution reveals then a discrepancy in the energy distribution among the natural frequencies between the numerical and the experimental system response. Therefore, neither the white noise and the filtered white noise are correct signals to reproduce the dynamic excitation from the contact.

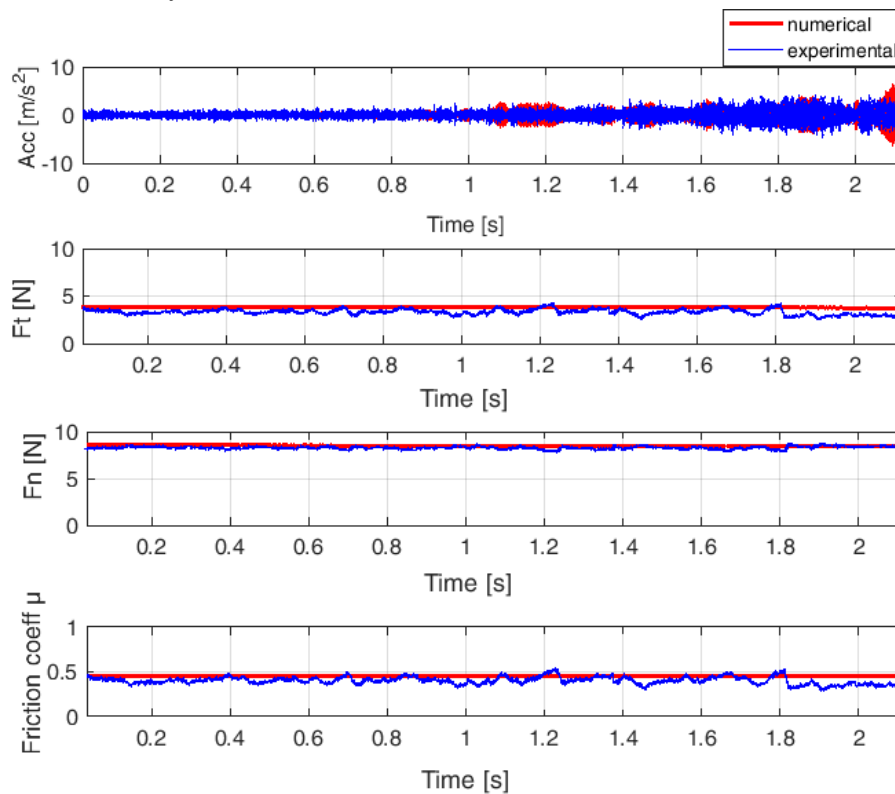


Fig. V-8: superposition of numerical (red) and experimental (blue) time evolution of contact forces, acceleration and friction coefficient. The signal chosen for the perturbative term is the filtered white noise.

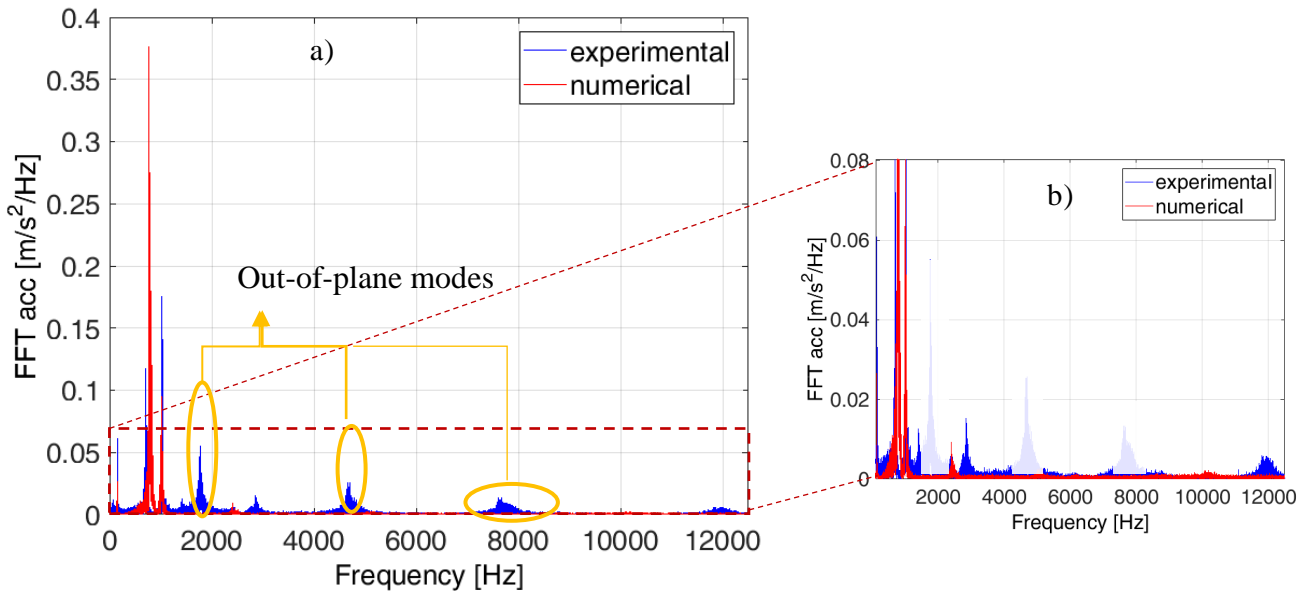


Fig. V-9: a) superposition of numerical (red) and experimental (blue) spectral evolution of the acceleration b) magnification of the spectral evolution with focus on the higher frequency band. The signal chosen for the perturbative term is the filtered white noise.

V-2.3 Signal retrieved from experiments by inverse method

Considering the previous results and the differences showed between the experimental measurements and the numerical simulations, a third signal has been implemented into the friction law. This signal is retrieved from the experimental measurements, exploiting the measured acceleration and the transfer function of the system (paragraph V-1). Employing this method, the spectral distribution of the perturbative term of the friction coefficient is directly recovered from the spectral distribution of the acceleration, measured experimentally (Eq.4.4).

Fig. V-10 shows the spectral distribution of the signal: the most energetic band is within the low frequency range, as for the Butterworth filtered white noise; nevertheless, after 2000 Hz, there is still a not negligible contribution to the energy content of the signal. This distribution is then able to account for the two frequency components of the contact excitation: the one mainly related to the spatial distribution of the surface roughness, characterized by a frequency content in the low frequency band at which the asperities interact, and one related to the local impulsive phenomena at the contact (ruptures, impacts, ...), which extend the spectrum at the higher frequency range.

The introduction of the contact excitation, in term of perturbation of the friction coefficient, allows for introducing the dynamic effect of the contact interaction without considering the effective topography of the surface and/or third body particles, maintaining unchanged the computational costs.

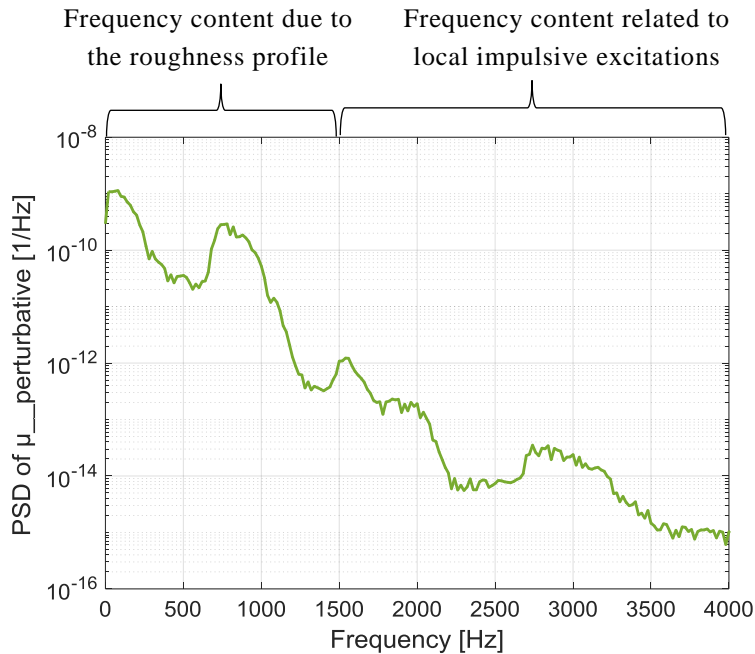


Fig. V-10: spectral evolution of the signal from the inverse method, chosen as the third signal for the perturbation term $R(x)$

Fig. V-11 presents the superposition between the numerical (red curve) and experimental (blue curve) time evolutions of the acceleration, normal force, tangential force and friction coefficient. The forces and the friction coefficient have the same evolution. The numerical response presents indeed the same trend of the experimental response both in term of amplitude (maximum and minimum are included between -5N and 5N) and time evolution. The acceleration in particular, showed with a magnification in Fig. V-13, presents a slight discrepancy between the experimental and the numerical evolution: the experimental signal has a higher amplitude in the initial phase due to the background noise of the signal, generated by the electrical noise of the acquisition chain.

Fig. V-12 shows the superposition of the spectrum (FFT) of the acceleration for the experimental (blue) and the numerical (red) results. The numerical evolution is in agreement with the experimental distribution, both in term of amplitude and frequency distribution. Fig. V-12a and Fig. V-12b show how, neglecting the peaks related to the transversal bending deformation modes of the upper beam (orange

circles), the numerical evolution has a good correspondence with the experimental response both for the low and the high frequency bands.

From the last analysed results, it can be affirmed that the spectral distribution of the perturbative term determined by the inverse method allowed for simulating correctly the measured Friction-Induced Vibrations, validating the proposed friction law for introducing the broadband excitation coming from the contact interface. Moreover, these results confirm the need for accounting for both the contributions to the contact excitation, due to the spatial distribution of the surface topography (lower frequencies) and the local impulsive excitations due to local impacts and ruptures (higher frequencies).

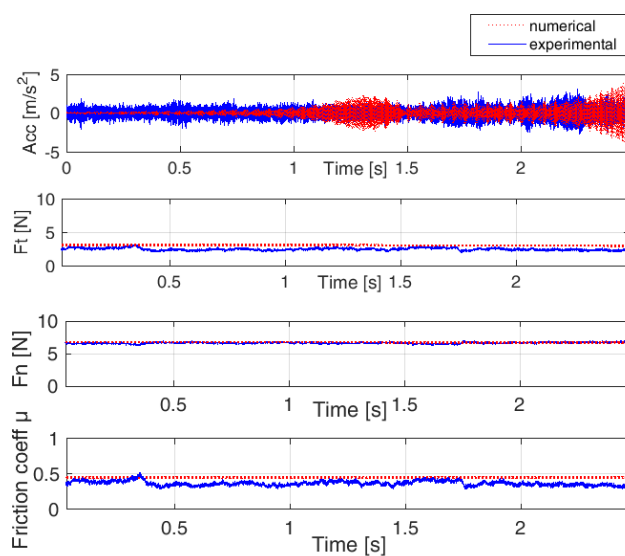


Fig. V-11: superposition of numerical (red) and experimental (blue) time evolution of contact forces, acceleration and friction coefficient. The signal chosen for the perturbative term is the one retrieved from the inverse method

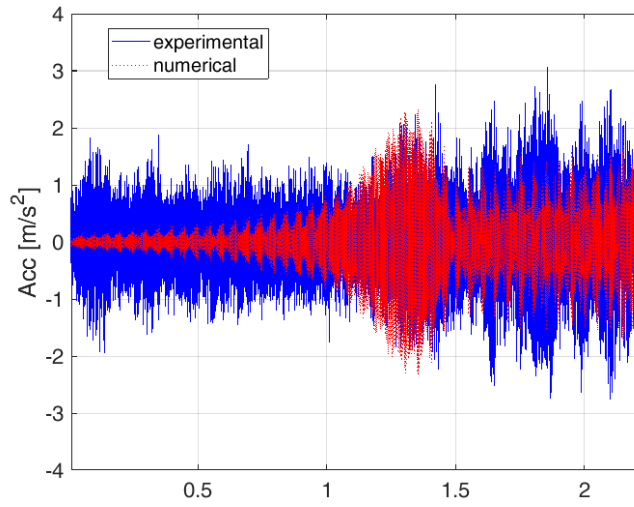


Fig. V-13: magnification of the first line in Fig. V-13, superposition of the experimental (blue curve) and the numerical (red curve) time evolution of the acceleration

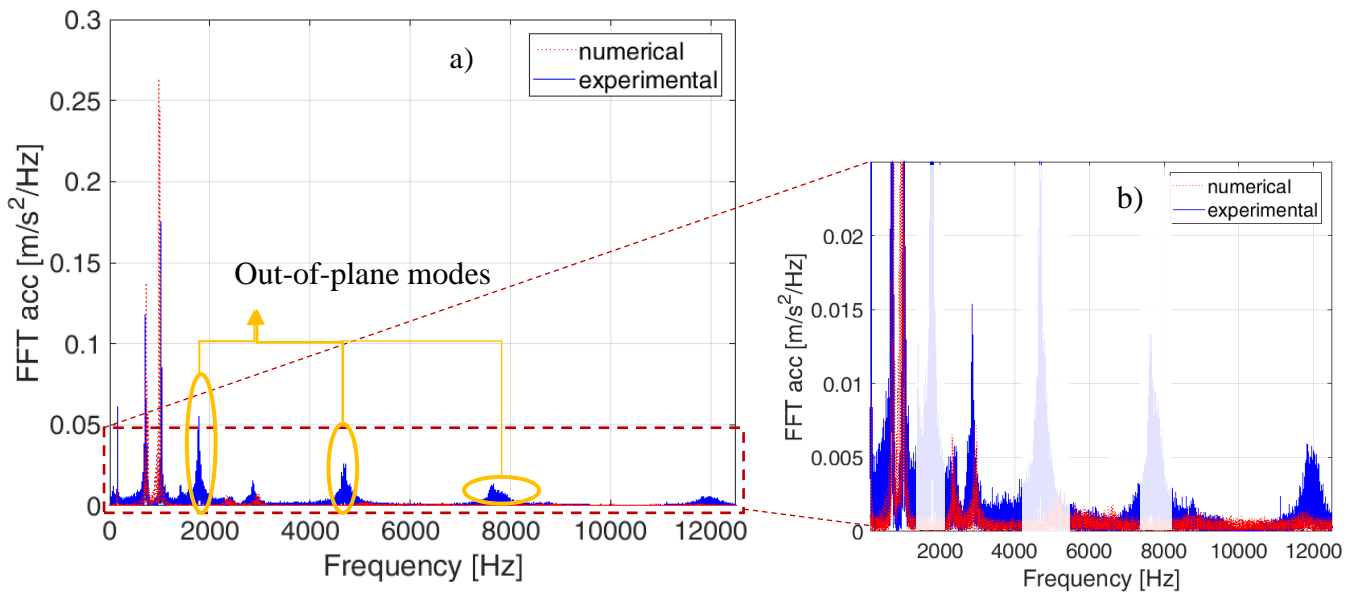


Fig. V-12 a) superposition of the experimental (blue) and the numerical (red) spectral distribution (FFT) of the acceleration; b) magnification of the spectral evolution with focus on the higher frequency band. The signal chosen for the perturbative term is the one retrieved from the inverse method, choosing the surface roughness R320.

V-3. Effect of contact and system parameters

The simulations described until now referred to a specific sliding velocity, 8 mm/s, and a peculiar surface roughness, R320. In these sections, the new friction law will be implemented for simulating variation in the contact and the system parameters. First, a different sliding velocity and different surface roughness are investigated and implemented into the numerical simulation. Then, a difference in the dynamics of the numerical and experimental systems, due to the difference in the stiffness of the boundary conditions, is investigated.

V-3.1 Influence of surface roughness

In the experimental campaign, different sandpapers for polishing the lower beam and the tip of the upper beam have been used to recover different surface roughness. The numerical simulations have been performed as well for the R320 and the R800 sandpapers in order to verify the possibility to account for the different surface roughness by the perturbative term of the friction law. The corresponding surface roughness are $R_a=0.39\mu\text{m}$ and $R_a=0.34\mu\text{m}$ respectively.

In the used friction law for the numerical simulations, this change is accounted by the $R(x)$ term. Using the same method presented in section V-1, the $R(x)$ term has been reconstructed from the acceleration (S_{aa} term) measured with the new surface roughness.

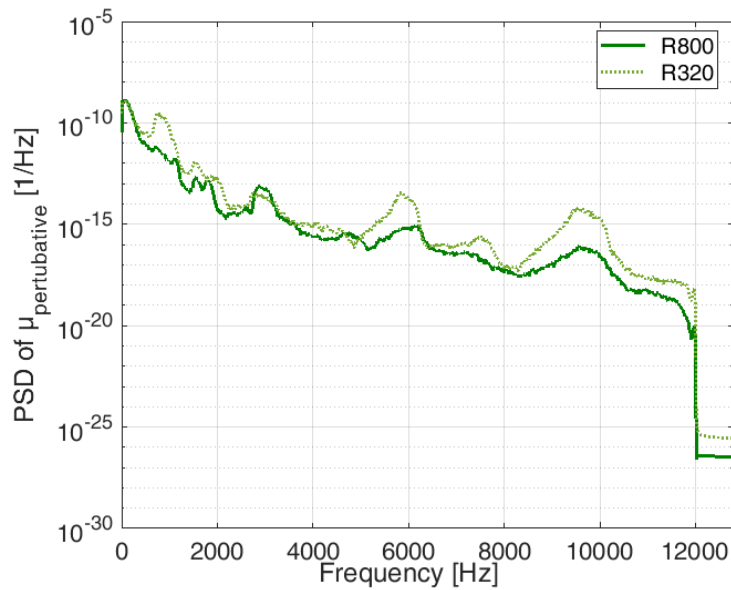


Fig. V-14: superposition between two signals of the perturbation term. The dotted curve is representative of the signal retrieved by the measure with a roughness R320, while the continuous curve with a roughness R800

Fig. V-14 shows the superposition of the spectral evolution of the perturbative term for the two different roughness. The dotted curve represents the trend for the R320 roughness, while the dark green curve is the one obtained for the R800 roughness.

Fig. V-15 shows the spectrum of the friction-induced vibrations (acceleration) measured (blue curve) and simulated (green curve) for the R800 surface roughness.

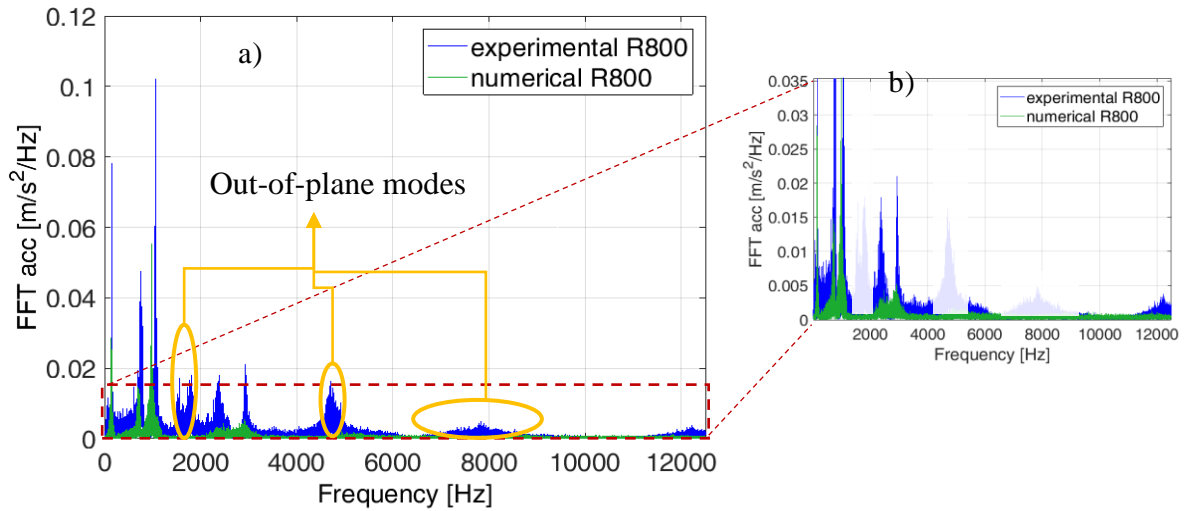


Fig. V-15: superposition of the experimental (blue) and the numerical (green) spectral distribution (FFT) of the acceleration for a surface roughness R800; b) magnification of the spectral evolution with focus on the higher frequency band

The numerical spectral evolution are in agreement with the experimental results in term of amplitude and spectral distribution, as showed before for the case of the R320 surface roughness. As for the previous analysis, the transversal vibration modes, not recoverable with a 2D numerical model, are neglected.

Fig. V-16 and Fig. V-17 show the superposition of the numerical results (time and spectral distribution) for the two surface roughness, R320 and R800. As remarked with the experimental results (section III-3.3), the level of excitation is related to the surface roughness: the vibration amplitude for both the spectral and time evolution has an increase passing from R800 to R320.

The used friction law is thus able to account for the change in the surface roughness, providing reliable results for the dynamic response of the system to the dynamic contact excitation.

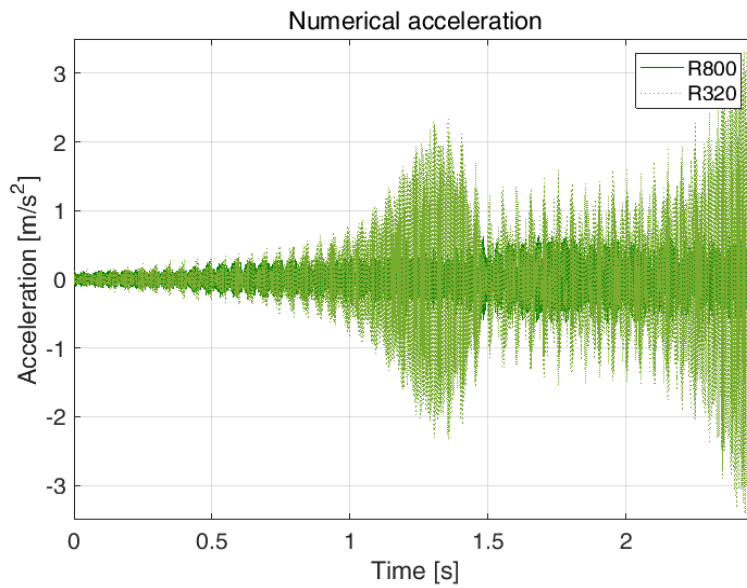


Fig. V-16 superposition of the numerical time evolution of the upper beam's acceleration for a surface roughness R800 (dark green) and R320 (dotted green).

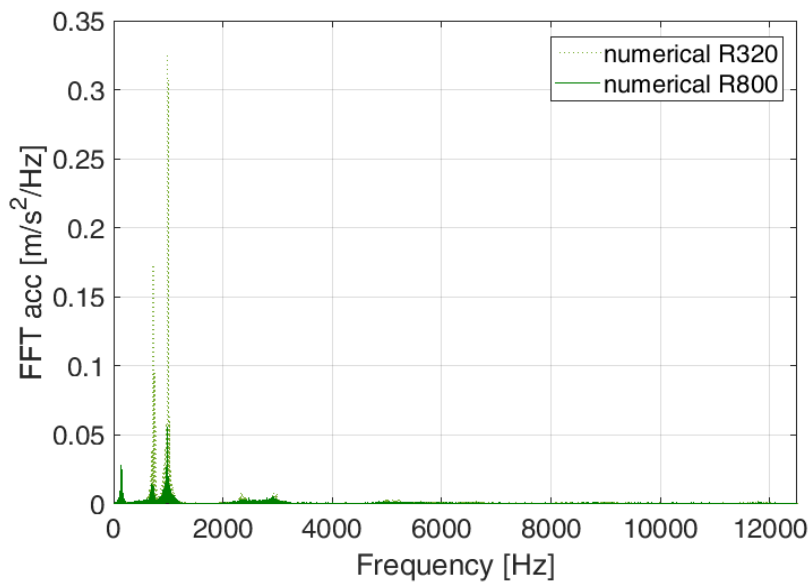


Fig. V-17: superposition of the numerical spectral distribution (FFT) of the acceleration for a surface roughness R800 (dark green) and R320 (dotted green)

V-3.2 Influence of sliding velocity

From the experimental parametrical analysis, an almost linear trend of the amplitude of the Friction-Induced Vibrations (RMS acceleration), with respect to the sliding velocity, has been identified (see section III-3.1). In the friction law, represented in Eq. 5.1, the linear trend with the sliding velocity has been then introduced, meaning that the exponent b in the equation Eq.5.1 has been set to 1:

$$\mu(x) = \mu_{const} + A|v(t)|R(x) \quad \text{Eq.5.8}$$

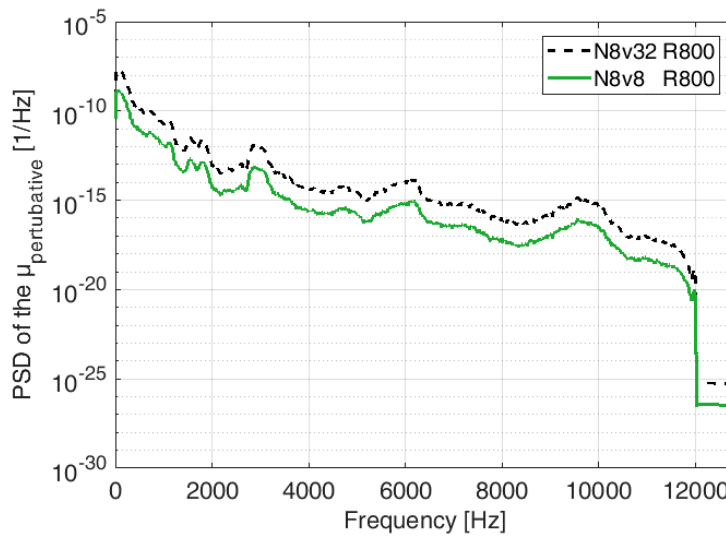


Fig. V-18: superposition of the spectral evolution of two perturbative contribution to the friction law (the term $A|v(t)|R(x)$): in dotted black for a sliding velocity of 32mm/s, in green the one for a sliding velocity of 8mm/s. Surface roughness R800

In order to verify that the proposed friction law is able to reproduce the effect of the sliding velocity on the friction-induced vibrations, the perturbative term of the friction law for 32 mm/s has been calculated directly using the same term $R(x)$ retrieved for 8 mm/s, simply multiplying the perturbative term by the ratio (equal to 4 in this case) between the two tested velocities (Fig. V-18). This means that the effect of the sliding velocity, on the broadband excitation from the contact interface, is directly introduced into the velocity term of the friction law, without the need of recovering the spectrum of the excitation by inverse method for each value of the velocity.

Fig. V-19 shows the superposition between the spectral evolutions of the perturbative terms of the friction coefficient at 32 mm/s, in the following different manners: the one retrieved from the evolution at 8 mm/s, and multiplied by 4, in

dotted black; the other one, in sky blue, recovered directly from the measure with a sliding velocity of 32 mm/s. The two evolutions have a good correlation, validating the introduction into the friction law of a linear relationship between the sliding velocity and the amplitude of the spectrum, maintaining unchanged the term $R(x)$ retrieved from the inverse method for one single velocity.

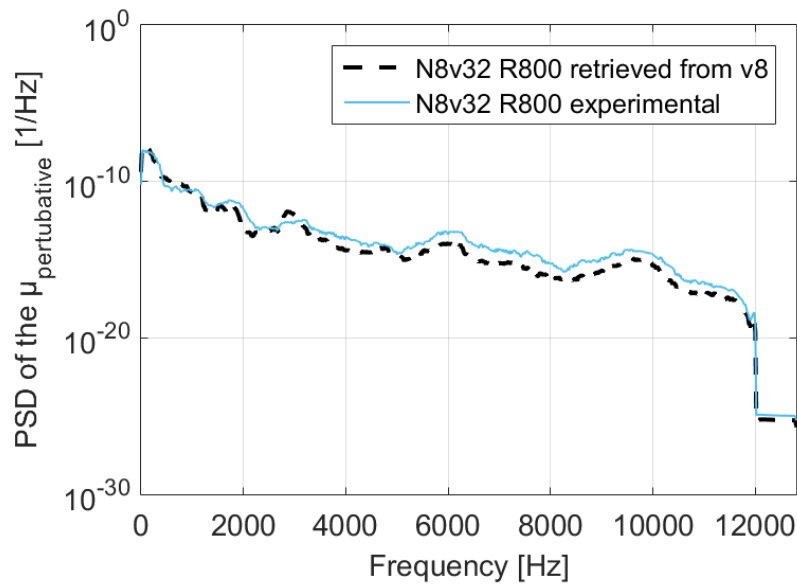


Fig. V-19: superposition of the spectral evolution of two perturbative contribution to the friction law (the term $A|v(t)|R(x)$) for a sliding velocity of 32mm/s: in dotted black retrieved from the experimental measure with a sliding velocity of 8mm/s, and multiplied by 4; in sky blue the evolution retrieved from the experimental measure at 32 mm/s. Surface roughness R800.

Fig. V-20 presents the comparison between the experimental (blue curve) and the numerical (black curve) time evolution for a velocity of 32 mm/s, with an imposed normal load of 8N and a surface roughness R800. The two evolutions show a good agreement, as for the case with a lower sliding velocity (Fig. V-13).

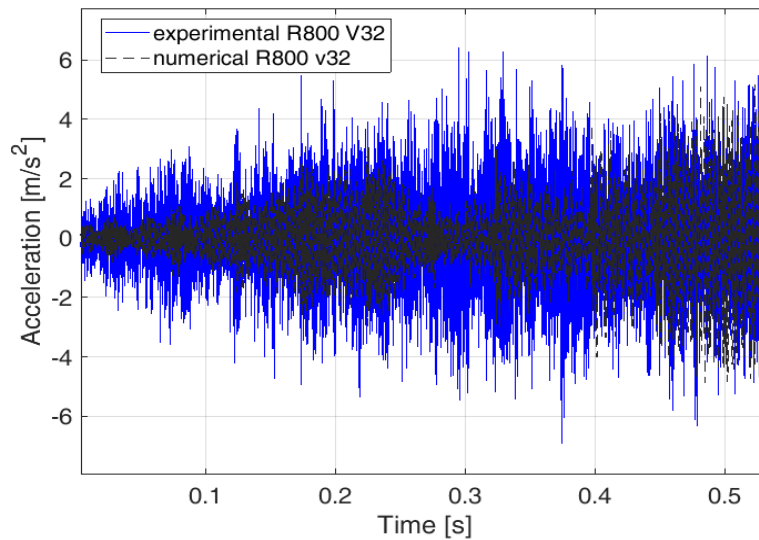


Fig. V-20: superposition of the numerical (black) and experimental (blue) time evolution of the acceleration for 32 mm/s, with 8N of normal load and R800 roughness

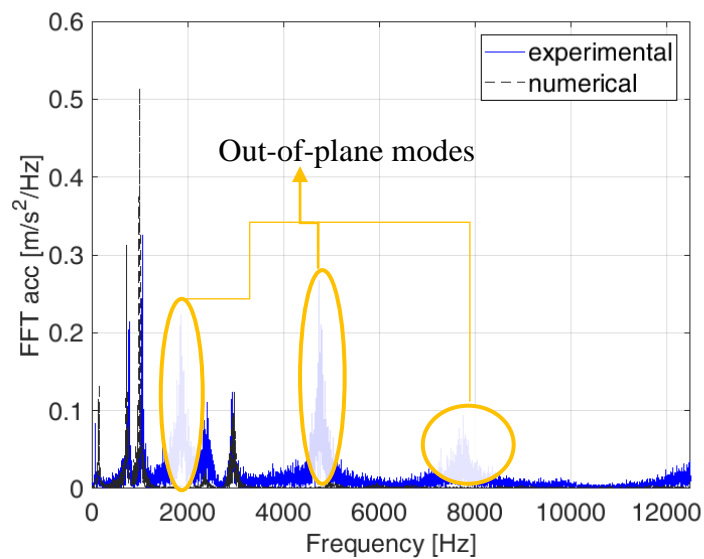


Fig. V-21: superposition of the experimental (blue) and numerical (black) response in term of FFT for 32 mm/s, with 8N of normal load and R800 roughness

Fig. V-21 presents the superposition between the experimental measurement and numerical simulation in the spectral domain. The frequency distribution and amplitude of the induced vibrations show a good agreement, except for the

frequency peaks relative to the out-of-plane vibrational modes, which vibrate outside the simulated plane by the 2D model.

The same analysis has been conducted for the other surface roughness, R320. Fig. V-22 presents the spectral distribution of the perturbative term for the two sliding velocities with a surface roughness of R320. The friction law has been modified only changing the term $R(x)$, retrieved from the measure at 8 mm/s. As for the case of roughness R800, the signal has been multiplied by a factor 4, to take into account the passage of the sliding velocity from 8 mm/s to 32 mm/s.

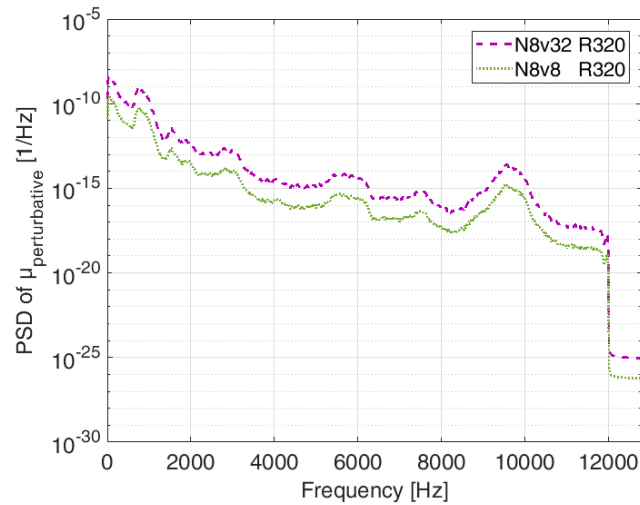


Fig. V-22: superposition of the spectral evolution of the two perturbative contributions to the friction law (the term $A|v(t)|R(x)$): in dotted green for a sliding velocity of 8mm/s, in violet the one for a sliding velocity of 32mm/s. Surface roughness R320.

Fig. V-23 and Fig. V-24 present the same comparisons, in the time and spectral domains, between the experimental and numerical results, carried on for the surface roughness R320.

As for the case with a surface roughness R800, also with R320 the numerical results, in term of time and spectral evolution of the acceleration, show a good agreement with the experimental measures, except for the out-of-plane modes.

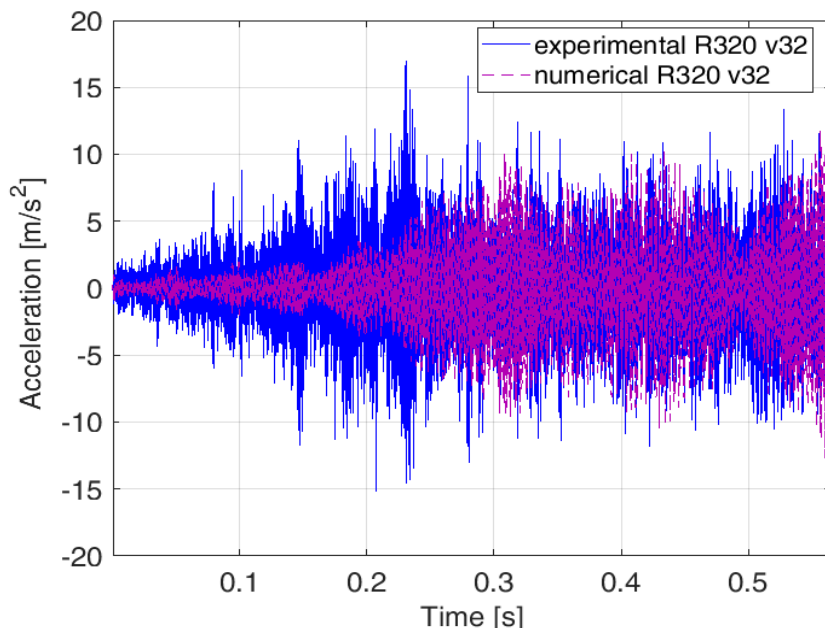


Fig. V-23: superposition of the numerical (violet) and experimental (blue) time evolution of the acceleration for 32 mm/s, with 8N of normal load and R320 roughness

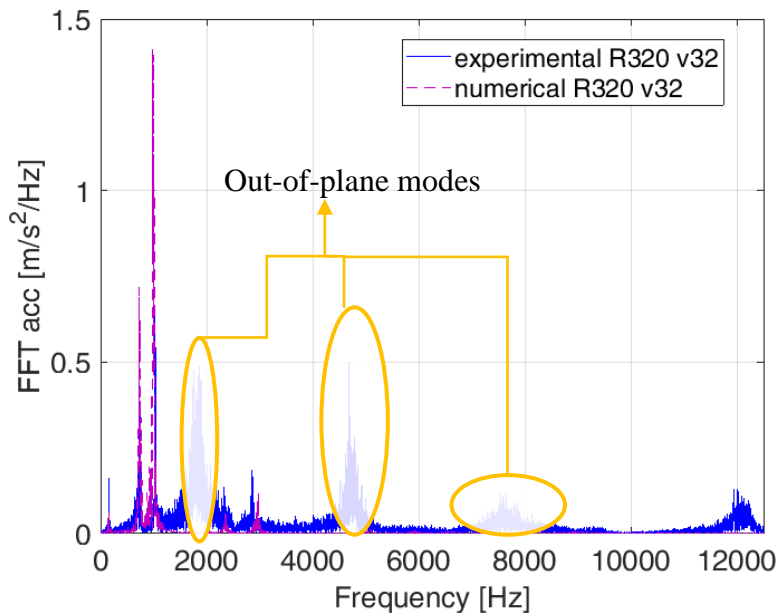


Fig. V-24: superposition of the experimental (blue) and numerical (violet) dynamic's response in term of FFT for 32 mm/s, with 8N of normal load and R320 roughness.

Therefore, the proposed law succeeds in taking into account the effect of the sliding velocity by the linear trend of the amplitude of the perturbative term,

without the need of identifying the spectral distribution of the contact excitation when considering different sliding velocities.

V-4. Effect of the boundary conditions and system dynamics

The friction law has been validated in the previous analysis, showing numerical results in agreement with the experimental measurements and highlighting that the introduced law can also consider a change in the surface roughness as well as in the sliding velocity.

In order to have a dynamic response as close as possible to the experimental one, allowing for a quantitative comparison with the measurements, softer layers of material have been added at the connections with the frame (see section IV-1.2) in the *updated model*.

In the following sections the friction law has been used into the same model, but without softer layers (named *stiffer model*). The aim is to investigate the effect of a difference in the dynamics of the numerical model and the one of the experimental system, where the broadband excitation has been determined by inverse method.

First the simulations have been performed on the stiffer model, directly introducing the perturbative term obtained experimentally by the inverse method. This means that the same (measured) excitation coming from the contact is introduced into a numerical model with a stiffer dynamics than the one of the experimental set-up.

Then, trying to account for the frequency shift due to the higher stiffness of the model, a stretch of the perturbative term in the frequency range has been performed too. The frequency vector S_{ff} (i.e. $R(x)$) is shifted of a factor k in frequency, in order to tune the excitation spectrum with the shift between numerical and experimental natural frequencies.

For both the cases the chosen signal for the perturbative term is the one retrieved from the experimental measurements.

V-4.1 Stiffer boundary conditions and frequency shifting of the perturbative term

In Chapter II, the difference between the stiffer model and the updated model has been presented in term of natural frequencies: Tab. II-4 and Tab. II-5 show the

natural frequencies for both the models. The frequencies of the *stiffer model* resulted higher than the ones of the experimental system and, then, of the *updated model*.

The following figures, from Fig. V-25 to Fig. V-29, allow to compare the results by both the *stiffer model* and the *stiffer model with a shift in the frequency vector* of the perturbative term, with the *updated model*.

Fig. V-25 presents the superposition of the time evolution of the acceleration obtained by the *stiffer model* (red curve) and the *updated model* (black curve). The numerical trend of the acceleration shows increasing and decreasing phases due to the passage of the contact point on the nodes and antinodes of vibration of the excited modes. Comparing the evolution from the stiffer model with the one relative to the updated one, it has to be remarked that the first increase of the acceleration occurs later in time (position of the contact point): in the *updated model* the acceleration increase and decreases between 1 and 1.5s; the same trend of the amplitude, for the *stiffer model*, occurs between 1.25s and 1.75s. Moreover, the amplitude obtained with the *stiffer model* is about the half of the one obtained with the *updated model*. These differences are due to the difference in stiffness of the two models, leading to lower vibration amplitude for the stiffer one, and to the shifting in the position of the nodes and antinodes of vibration.

Another overall difference between the models is visible in the spectral evolution of the acceleration, shown in Fig. V-26. The numerical peaks from the stiffer model (red curve) are positioned at higher frequencies than the those from the updated model (black curve), highlighting the high percentage error, shown in Tab. II-4, between the natural frequencies retrieved from the model with perfect clamped edges conditions and the experimental system.

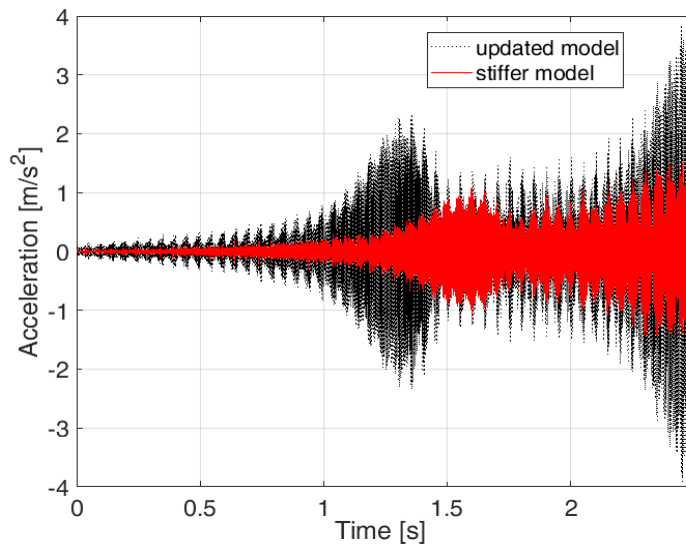


Fig. V-25: superposition of the time evolution of the acceleration for the updated (black dotted curve) and the stiffer model (red curve). Sliding velocity 8mm/s, surface roughness R320

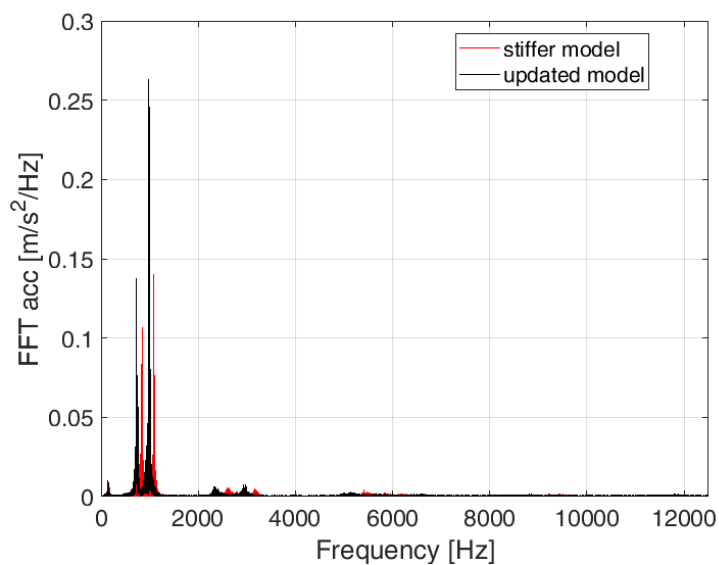


Fig. V-26: superposition of the spectral evolution of the acceleration obtained by the updated (black dotted curve) and the stiffer model (red curve). Sliding velocity 8mm/s, surface roughness R320

In order to account for the shift between the dynamics of the numerical model and the frequency distribution of the measured contact excitation, the same stiffer model has been excited with an equivalent perturbative term, which has been shifted in frequency too.

The shift has been obtained by modifying the frequency vector, f , employed to define the S_{ff} term. The original frequency vector is shifted by considering the gap between the experimental and the numerical natural frequencies. The shift has been operated to generate a new frequency vector $f_{shifted}$:

$$f_{shifted} = \frac{f}{k} \quad \text{Eq. 5.9}$$

where k is the shifting factor, which allows to rearrange the spectral distribution of the perturbative term, according to the frequency shift between the numerical and experimental natural frequencies.

Fig. V-27 shows the superposition between the two spectral evolutions of the perturbative term: in dotted green the original spectral distribution, in pink the spectral distribution which has been defined from the shifted frequency vector $f_{shifted}$. The k factor for the shifting has been chosen equal to 1.12, after evaluation of the difference between the experimental and the numerical natural frequencies.

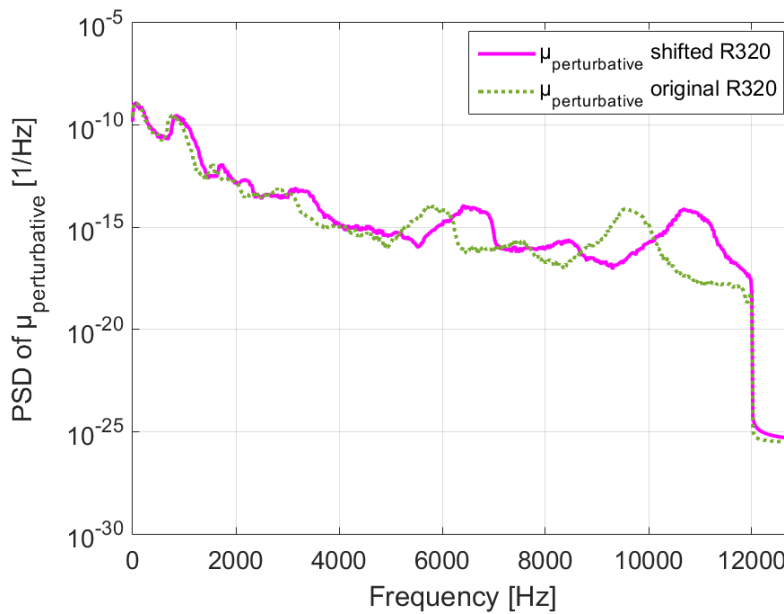


Fig. V-27: superposition of the original perturbative term for the surface roughness R320 (green dotted curve), and the perturbative term subjected to the shifting in the frequency vector (pink curve), for R320.

Maintaining constant the contact parameters (sliding velocity 8mm/s, surface roughness R320), the time evolutions (Fig. V-25 and Fig. V-28) show similar delay between the acceleration obtained by the *updated model* and those obtained by both the *stiffer model* and the *stiffer model with frequency shift*. The

acceleration recovered from the updated model has an increase and a following decrease between 1s and 1.5s, while the other simulations present the same trend delayed of 0.25s. This discrepancy reveals that, as expected, both the models present a different position of the nodes and antinodes of vibrations, with respect to the updated model. Nevertheless, the shifting of the perturbative term allows to obtain a vibration amplitude closer to the one from the updated model, whereas the stiffer model presented a vibration amplitude two times lower.

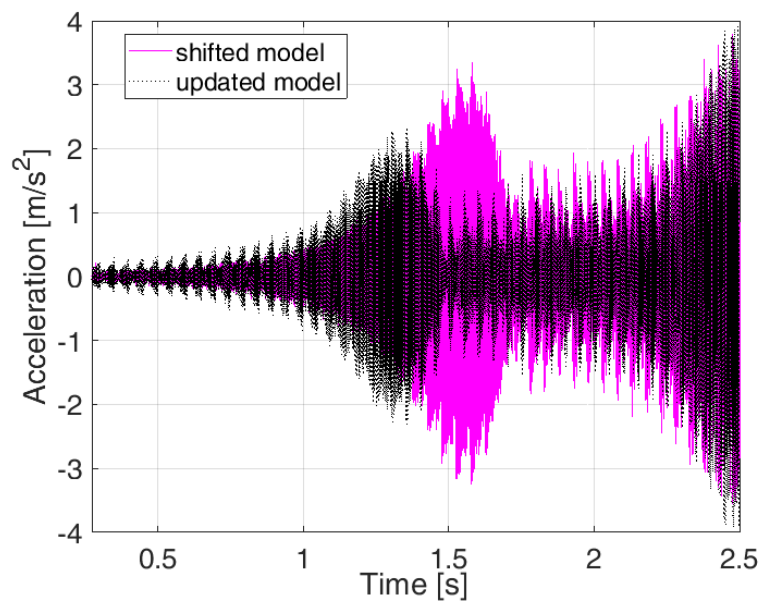


Fig. V-28: superposition of the time evolution of the acceleration for the updated (black dotted curve) and the shifted model (pink curve). Sliding velocity 8mm/s, surface roughness R320

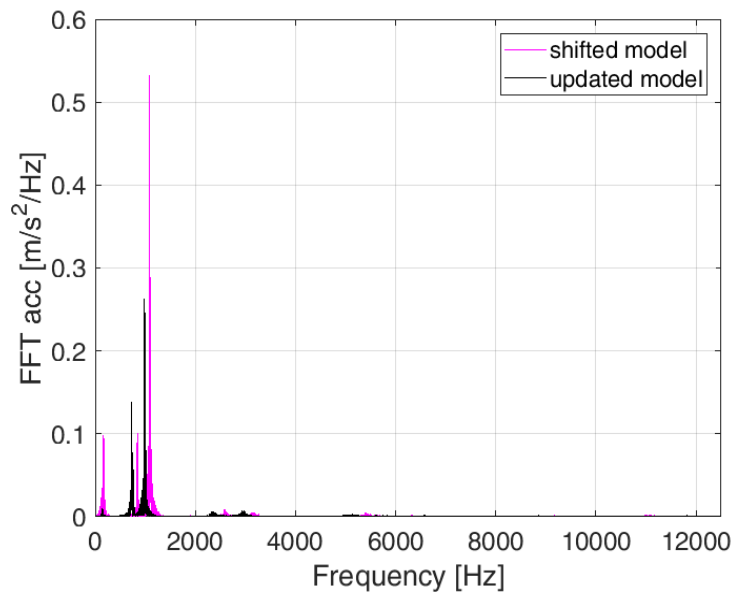


Fig. V-29: superposition of the spectral evolution of the acceleration for the updated (black curve) and the shifted model (pink curve). Sliding velocity 8mm/s, surface roughness R320

The same characteristic in the vibrational response is visible in the spectral evolutions (Fig. V-26 and Fig. V-29): both the simulations present natural frequencies higher than those by the update model, but the model with a frequency shift of the perturbative term presents a higher amplitude of the frequency peaks. From all the analysed numerical results, it is possible to affirm that the presence of a loss in stiffness, due for instance to an experimental clamping condition, can be simulated only by reproducing the loss in stiffness into the numerical model (updated model). The introduction of a shift in the frequency vector of the perturbative term, i.e. shifting the frequency content of the dynamic excitation in accordance with the shift of the numerical natural frequencies, determines a vibration amplitude more similar to the experimental one, but the same main discrepancies due to the differences in natural frequencies and deformed shapes. Then, the results from the updated model have the best accordance with the experimental measures, showing time and spectral evolutions in agreement with the experimental results, in term of both amplitude (time) evolution and spectral distribution.

V-5. Conclusions

In this work a newer approach has been proposed to take into account the presence of the broadband dynamic excitation coming from the contact interface.

The introduced friction law considers a friction coefficient composed by two terms: a constant term, which corresponds to the classical Coulomb law; and a perturbative term, which introduces the broadband excitation determined by the sliding at a frictional interface.

Three different signals have been employed to reproduce the perturbative term: a white noise, a white noise filtered by a Butterworth filter and a signal retrieved from the measures. The different effect of their spectral distribution on the simulated Friction-Induced Vibrations, by comparison with the experimental measurements, has been highlighted.

The results obtained with the spectral distribution recovered by inverse method, with respect to the ones obtained by a white noise and a filtered one, allowed to highlight the need to account for both a low frequency band contribution, which is directly related to the topography of the surface roughness, and a higher frequency band contribution, which is related to the impulsive excitation coming from the local contact phenomena, such as ruptures, asperity impacts, third body evolution, etc...

The comparison between numerical and experimental results validated the possibility to reproduce the Friction-Induced Vibrations, by the proposed friction law, without introducing a computationally expensive representation of the real contact interface (surface topographies, third body particles, ...). Only its dynamic effects, on the system excitation, is introduced.

The friction law has been tested for two different surface roughness, accounting for the change in the spectral distribution of the contact excitation. Furthermore, the influence of the sliding velocity has been analysed, introducing a linear bond between the amplitude of the perturbative term of the friction coefficient and the sliding velocity. Also in this case, the comparisons between the experimental and the numerical results showed a good agreement, validating the introduction of a linear velocity dependence into the friction law.

The effect of a shift in frequency between the dynamics of the numerical model and the experimental system has been then investigated. It has been shown that this shift in frequency can be accounted for only performing an updating of the numerical model; introducing a shifting in the perturbative term in frequency didn't allow, indeed, to recover the same vibrational response encountered in the

experimental campaign. Actually, the updated model presented the numerical results characterized by the best agreement with the experimental measures.

VI General conclusions

This thesis has been focused on the study of the Friction-Induced Vibrations thanks to a simple frictional system, composed by two beams in relative sliding contact. The investigation has been realized with a preliminary experimental campaign and following numerical analyses.

A 2D numerical model has been built, with the objective of reproducing the transient dynamic response encountered during the experimental frictional tests. In the framework of numerical models, nowadays employed to simulate complex systems with frictional contacts, the transient simulations are widely used; nevertheless, a main drawback is the lack in accounting for the broadband excitation generated at the contact interface. In this work, a friction law has been proposed to account for the dynamic phenomena at the contact scale, being able to consider the broadband dynamic excitation by a sliding frictional interface.

Comparing the numerical results with the experimental ones, the proposed approach has been validated, showing a good agreement with the measurements carried on during the experimental campaigns.

The main results achieved in this work are described in the following sections, divided in two parts: first the results from the experimental campaigns will be presented, followed by those from the numerical model with the implementation of the friction law.

VI-1. Original contributions

VI-1.1 Experimental analysis

The experimental campaign has been addressed to the study of the dynamic response of the system and to the analysis of the Friction-Induced Vibrations due to the system response under the contact excitation.

A parametrical campaign has been carried on to investigate the influence of three key contact parameters: the imposed normal load, the sliding velocity and the surface roughness.

The campaign has been realized on two test-benches called TriboTouch and TriboAir, characterized by the ability of reproducing a relative motion between the elements in contact, without introducing any parasitic noise into the measures. The two test-benches allowed indeed to measure only the vibrations induced by the frictional contact between the beams, assuring the absence of other sources of friction.

The parametrical experimental campaign allowed for characterizing the system dynamic response; in particular the Friction-Induced Vibrations in term of frequency spectrum and the RMS of the measured acceleration. Three characteristic evolutions have been recognized for the analyzed parameters:

- With an increase in the imposed normal load at the contact interface, the evolution of the amplitude of the resulting friction-induced vibrations showed four main zones:
 - A first zone of *weak contact* between the beams characterized by a high amplitude of vibrations. The beams are under almost uncoupled conditions at the contact, characterized by the emission of the so-called *roughness noise*;
 - A second zone characterized by the transition of the system from *weak to strong contact* conditions, with a large variability in the vibrational response amplitude with respect to small variations of the contact load;
 - A third zone of *strong contact* conditions, where the beams can be then considered as a fully coupled system; an increase in the normal load corresponds, in this zone, to an increasing of the vibration amplitude because of the increase in the contact power;
 - A fourth zone where, because of the excessive contact pressure, the plasticization of the surface roughness determines a decrease in the vibrational response; the asperities of the surface roughness are plasticized during the contact.
- An increase in the sliding velocity showed an increase in the amplitude of the friction-induced vibrations, due to the increase of the power exchanged at contact interface, causing a growth in the amplitude of the vibrational energy reinjected into the system and thus an increase of the system vibrational response.
- A change in the surface roughness resulted in a variation of the coupling conditions at the interface; an increase in the energy content of each local contact zone between asperities, leads to more energetic impacts and ruptures, and thus a higher amplitude of the induced vibrations.

From the experimental campaigns, the characteristics of the system dynamics and of the generated Friction-Induced Vibrations have been delineated; then, a

numerical model has been built to simulate the same phenomena and in particular the broadband excitation from the contact.

VI-1.2 Numerical analysis

The experimental campaign and the relative analysis on the Friction-Induced Vibrations has been conducted in parallel with numerical simulations, in order to reproduce the Friction-Induced Vibrations encountered in the tests. Consequently, the main objective has been that of correctly reproduce the broadband excitation from the contact, which is at the origin of the induced vibrations.

A 2D Finite Element Model has been developed to investigate the system dynamics and to perform transient contact simulations.

A preliminary prestressed complex eigenvalue analysis has been performed to choose the geometry dimensions of the beams in order to avoid the rising of mode coupling instabilities. Once the dimension chosen, and the experimental set-up(s) developed, a further complex eigenvalue analysis had the objective of updating the model by the introduction of compliant layers at the clamped edges of the beams, in order to realize numerical boundary conditions as much possible similar to the experimental ones.

Once the characteristics of the numerical model defined, a first parametrical analysis has been carried on without considering the presence of the dynamic excitation from the contact, employing the classical Coulomb friction law with a constant friction coefficient.

The comparison between the experimental and the numerical results highlighted the need of introducing the broadband excitation coming from the contact interface into the numerical model. If not, the numerical simulations are enable to reproduce correctly the vibrations induced during the relative sliding.

For this reason, a new friction law has been then used for the transient simulations. It introduces a friction coefficient composed by two terms: a constant term, as in the Coulomb law, and a perturbative term, which wishes to account for the broadband excitation generated by the frictional contact between the surfaces.

Three different spectral distributions of the perturbative term have been proposed and evaluated to reproduce the Friction-Induced Vibrations measured during the experimental campaign: a white noise, a white noise filtered by a Butterworth filter and a spectral distribution retrieved by the measurements, thanks to an

inverse method. The influence of each spectral distribution of the perturbative term on the system dynamic response has been investigated, comparing the numerical results with the experimental measures. After correlations, the signal that best reproduces the contact excitation is the one retrieved by the inverse method. Its spectral distribution underlined the need to account for two main contributions:

- a first contribution, directly related to the surface topography, which determines the high amplitude of the excitation at the low frequency band [0-2000 Hz]; this contribution could be attributed to the frequency of interactions between the surface asperities;
- the second one, related to the impulsive nature of the local excitation, generated by the local contact phenomena, such as ruptures and impacts between asperities, which bring energy to the higher frequency range of the contact excitation [0-8000 Hz].

The proposed friction law has been validated by comparing the acceleration simulated numerically with the one measured experimentally; the introduction of a perturbative term into the friction law allowed to obtain a numerical evolution of the Friction-Induced Vibrations in agreement with the trend observed experimentally.

The friction law has been then tested with two different surface roughness, considering a change in the spectrum of the contact excitation. Moreover, a change in the sliding velocity has been considered, introducing a linear bond between the amplitude of the perturbative term of the friction coefficient and the sliding velocity. Once again, the comparison of the numerical results with the experimental ones showed a good agreement, validating the proposed friction law also for a change in surface roughness and in the sliding velocity.

Eventually, the friction law has been introduced into a stiffer model, without updating of the boundary conditions, showing the discrepancy of the natural frequencies and the time evolution and amplitude of the induced vibrations. Instead of updating the model, a different strategy to approach the experimental response is the stretching in frequency of the spectrum of the perturbative term, to recover a frequency shift similar to the one of the dynamics of the numerical system.

In conclusion, the proposed friction law has been able to reproduce the Friction-Induced Vibrations without introducing a representation of the real surface topography and other local features (third body, local adhesion, ...), which usually need a large number of elements to describe the contact phenomena. The direct inclusion of the dynamic effects of the local contact phenomena into the perturbation term of the friction coefficient allows then to reproduce the Friction-Induced Vibrations without increasing the computational costs.

VI-2. Suggestions for future developments

Future works will focus on the implementation of the others contact parameters in the friction law, analyzing, for instance, the effects of a change in the normal load or in the material properties into the dynamic response of the numerical system. In fact, while a simple linear trend of the amplitude of the perturbative term, and the consequent induced vibrations, has been implemented in the friction law, the more complicated trend with the load, switching between weak and strong contact, should be implemented too.

In the short term, a further experimental campaign will be performed on a new couple of sliding beams, characterized by different geometrical dimensions, i.e. a different system dynamics. The aim is to demonstrate that the spectral evolution of the excitation coming from the sliding contact, associated in this work with the term S_{ff} , is independent from the dynamics of the system. The same perturbative term recovered on the analysed system will be used for the new system, to verify its efficiency in reproducing the contact excitation, independently from the dynamics of the system.

Focusing always on the experimental analysis, it could be interesting to evaluate the influence of a different surface roughness between the upper and the lower beam, choosing for instance a smoother roughness for the lower beam and a high roughness for the tip of the upper beam, investigating the effects in the contact conditions and in the transition from weak to strong contact.

The final aim is to define the perturbative term of the friction law, for each combination of the contact parameters, in order to correctly reproduce the contact excitation without performing the measurements, needed here to recover the spectral distribution of the perturbative term.

Finally, considering the whole frictional system, a study on the energy transfer within the frequency bands could be carried on, quantifying the energy transferred

from the contact to the system thanks to the broadband contact excitation, and defining the best contact conditions to transfer (or not) a greater amount of energy. This study, indeed, could involve interesting applications, such as contact dampers or the passive health monitoring [106].

Bibliography

- [1] V. Popov, *Contact Mechanics and Friction*, Springer, 2010.
- [2] G. Amontons, "De la résistance causée dans le machines", *Mem.Acad. R.Sci.*, 1699.
- [3] C. Coulomb, *Theorie de machines simples*, Paris: Bachelier, Libraire, Quai des Quagustins, 1821.
- [4] H. Hertz, *Ueber die Beruehrung elastischer Koerper (On Contact Between Elastic Bodies)*, Leipzig, Germany: *Gesammelte Werke (Collected Works)*, 1882.
- [5] F. P. Bowden and D. Tabor, *Friction and lubrication of solids Part I*, vol. I, Oxford: Clarendon Press, 1950.
- [6] F. Bowden and D. Tabor, *Friction and lubrication of solids Part II*, vol. II, Oxford: Clarendon Press, 1954.
- [7] F. P. Bowden and D. Tabor, *The area of contact between stationary and between moving surfaces*, P. o. t. R. S. o. London, Ed., Series A, *Mathematical and Physical Sciences*, 1939, pp. 391-413.
- [8] J. Archard, "Elastic Deformation and the Laws of Friction," *Proceedings of the Royal Society A: Mathematical, Physical and Engineering Sciences*, vol. 243, pp. 190-205, 1957.
- [9] J.Greenwood and J.Williamson, "Contact of nominally flat surfaces," *Proceedings of the Royal Society A: Mathematical, Physical and Engineering Sciences*, pp. 300-319, 1966.
- [10] A. Bush, R. Gibson and T. Thomas, "The elastic contact of a rough surface," *Wear*, vol. 35, pp. 87-111, 1975.
- [11] B. Persson, F. Bucher and B. Chiaia, "Elastic contact between randomly rough surfaces: Comparison of theory with numerical results," *Physical Reviews*, 2002.
- [12] G.Shang, *Friction-Induced Vibrations and Sound*, CRC Press, 2008.
- [13] J. Brunetti, "Mechanical energy balance of frictional contacts : From surface to solid energy dissipation in contact dynamic instabilities," PhD Thesis, Insa de Lyon, Univesità dell'Aquila, 2015.
- [14] M. Di Bartolomeo, F. Massi, L. Baillet, A. Culla, A. Fregolent and Y. Berthier, "Wave and rupture propagation at frictional bimaterial sliding

- interfaces: From local to global dynamics, from stick-slip to continuous sliding,” *Tribology International*, vol. 52, pp. 117-131, 2012.
- [15] R. Ibrahim, “Friction-induced vibration chatter squeal and chaos - Part_I: Mechanics of contact and Friction,” *Applied Mechanics Reviews*, 1994.
- [16] F. Bowden, A. Moore and D. Tabor, “The Ploughing and Adhesion of Sliding Metals,” *Journal of Applied Physics*, vol. 14, pp. 80-91, 1943.
- [17] B. Armstrong-Hélouvry, *Control of Machines with friction*, New-York: Springer, 1991.
- [18] J. Sampson, F. Morgan, D. W. Reed and M. Muskat, “Friction behavior during the slip portion of the stick-slip process,” *Journal of Applied Physics*, vol. 14, pp. 689-700, 1943.
- [19] M. Chowdhury, M. Khalil, D. Nuruzzaman and M. Rahaman, “The Effect of Sliding Speed and Normal Load on Friction and Wear Property of Aluminum,” *International Journal of Mechanical & Mechatronics Engineering*, vol. 11, no. 1, 2011.
- [20] E. Riedo, F. Lévy and H. Brune, “Kinetics of Capillary Condensation in Nanoscopic Sliding Friction,” *Phys. Rev. Lett.*, vol. 88, 2002.
- [21] K. ., Grosch, “The relation between the friction and visco-elastic properties of rubber,” *Proceedings of the Royal Society A*, 1963.
- [22] H. Ouyang, J. Mottershead, M. Cartmell and M. Friswell, “Friction-Induced Parametric Resonances in Discs: Effect of a negative friction-velocity relationship,” *Journal of Sound and Vibration*, pp. 251-264, 1998.
- [23] S. Dokos, “Sliding Friction under Extreme Pressure 1,” *ASME Journal of Applied mechanics*, vol. 86, pp. 148-156, 1946.
- [24] I. Kragel'skii, *Friction and Wear*, London: Butterworths, 1965.
- [25] A. D'Souza and A. Dweib, “Self excited vibrations induced by dry friction, Part 2: stability and limit-cycle analysis,” *Journal of Sound and Vibrations*, vol. 137, pp. 177-190, 1990.
- [26] G. Sheng, *Friction-Induced Vibrations and Sound*, New York: CRC Press, Taylor and Francis Group, 2008.
- [27] A. Akay, “Acoustics of friction,” *J Acoust Soc Am*, vol. 111, pp. 1525-1548, 2002.
- [28] R. Ibrahim, “Friction-induced vibration, chatter, squeal, and chaos. Part II: Dynamics and modeling,” *Appl. Mech. Rev.*, vol. 47, no. 7, 1994.

- [29] M. Bengisu and A. Akay, "Stability of friction-induced vibrations in multi-degree-of-freedom systems," *Journal of Sound and Vibrations*, vol. 171, pp. 557-570, 1994.
- [30] J. Martins, Raous and M., *Friction and Instabilities*, New York: Springer-Verlag, 2002.
- [31] G. Adams, "Self-Excited Oscillations of Two Elastic Half-Spaces Sliding with a Constant Coefficient of Friction," in *Transaction of the ASME*, 1995.
- [32] J. Dieterich, "Time-Dependent Friction and the Mechanics of Stick-Slip," *Pure Appl. Geophys.*, vol. 116, 1978.
- [33] Y. Ben-Zion and Y. Huang, "Dynamic rupture on an interface between a compliant fault zone layer and a stiffer surrounding solid," *Journal of Geophysical Research*, vol. 107, 2002.
- [34] M. D. Bartolomeo, F. Massi, L. Baillet, A. Culla, A. Fregolent and Y. Berthier, "Wave and rupture propagation at frictional bimaterial sliding interfaces: From local to global dynamics, from stick-slip to continuous sliding," *Tribology International*, vol. 52, pp. 117-131, 2012.
- [35] J. Wells, "Kinetic Boundary Friction," *The Engineer*, vol. 147, p. 454, 1929.
- [36] J. Den Hartog, "Force Vibrations with Combined Coulomb and Viscous Friction," *ASME APM-53*, pp. 107-115, 1931.
- [37] H. Blok, "Fundamental Aspects of Boundary Friction," *J. Society of Automotive Engineer*, vol. 46, p. 275, 1940.
- [38] B. Derjagin, V. Push and D. Tolstoi, "A Theory of Stick-Slip Sliding of Solids," *Proc. Conference on Lubrication and Wear, London*, 1957.
- [39] G.G. Adams, "Steady Sliding of Two Elastic half spaces with friction reduction due to interface stick-slip," *Journal of Applied Mechanics*, vol. 475, 1998.
- [40] R. Spurr, "'A theory of brake squeal'," vol. 1, no. 33-52.
- [41] H. Mills, *Brake Squeal*, Institution of Automobile Engineers, 1938.
- [42] M. North, "'Disc brake squeal - a theoretical mode'," 1972.
- [43] A. Akay, J. Wickert and Z. Xu, "Investigation of Mode lock-in and," Final Report, department of mechanical engineering, Carnegie Mellon University, Pittsburgh, 2000.

- [44] N. Kinkaid, O. O'Reilly and P. Papadopoulos, "Automotive brake squeal," *Journal of Sound and Vibration*, vol. 267, pp. 105-166, 2003.
- [45] A. Papinniemi, J. Lai, J. Zhao and L. Loader, "Brake squeal: a literature review," *Applied Acoustics*, vol. 63, pp. 391-400, 2002.
- [46] G. Ouenzerfi, F. Massi, E. Renault and Y. Berthier, "Squeaking friction phenomena in ceramic hip endoprosthesis: Modeling and experimental validation," *Mechanical Systems and Signal Processing*, Vols. 58-59, pp. 87-100, 2015.
- [47] C. Weiss, P. Gdaniec, N. Hoffmann, A. Hothan, G. Huber and M. Morlock, "Squeak in hip endoprosthesis systems: An experimental study and a numerical technique to analyze design variants," *Medical Engineering & Physics*, vol. 32, pp. 604-609, 2010.
- [48] N. Hoffman and L. Gaul, "Effects of damping on mode-coupling instability in friction induced oscillations," *ZAMM - Journal of Applied Mathematics and Mechanics / Zeitschrift für Angewandte Mathematik und Mechanik*, vol. 83, 2003.
- [49] J.-J. J. Sinou, "Mode coupling instability in friction-induced vibrations and its dependency on system parameters including damping," *European Journal of Mechanics - A/Solids*, vol. 26, 2007.
- [50] J. Sinou, "Transient non-linear dynamic analysis of automotive disc brake squeal – On the need to consider both stability and non-linear analysis," *Mechanics Research Communications*, vol. 37, pp. 96-105, 2010.
- [51] M. Dezi, P. Forte and F. Frendo, "Motorcycle brake squeal: experimental and numerical investigation on a case study," *Meccanica*, vol. 49, pp. 1011-1021, 2014.
- [52] L. Baillet, S. D'Errico and B. Laulagnet, "Understanding the occurrence of squealing noise using the temporal finite element method," *Journal of Sound and Vibration*, vol. 292, pp. 443-460, 2006.
- [53] F. Cantone and F. Massi, "A numerical investigation into the squeal instability: Effect of damping," *Mechanical Systems and Signal Processing*, vol. 25, no. 5, 2011.
- [54] F. Massi and O. Giannini, "Effect of damping on the propensity of squeal instability: an experimental investigation," *The Journal of Acoustic Society of America*, vol. 123, 2008.

- [55] J. Brunetti, F. Massi, A. Saulot, M. Renouf and W. D'Ambrogio, "System dynamic instabilities induced by sliding contact: A numerical analysis with experimental validation," *Mechanical Systems and Signal Processing*, Vols. 58-59, 2015.
- [56] J. Brunetti, F. Massi, W. D'Ambrogio and Y. Berthier, "A new instability index for unstable mode selection in squeal prediction by complex eigenvalue analysis," *Journal of Sound and Vibration*, vol. 377, pp. 106-122, 2016.
- [57] D. Tonazzi, F. Massi, A. Culla, A. L. Baillet and Y. Berthier, "Instability scenarios between elastic media under frictional contact," *Mechanical Systems and Signals Processing*, pp. 754-766, 2013.
- [58] D. Tonazzi, F. Massi, L. Baillet, A. Culla, M. Di Bartolomeo and Y. Berthier, "Experimental and numerical analysis of frictional contact scenarios: from macro stick-slip to continuous sliding," *Meccanica*, vol. 50, pp. 649-664, 2014.
- [59] H. Ben Abdelounis, A. Le Bot, J. Perret-Liaudet and H. Zahouani, "An experimental study on roughness noise of dry rough flat surfaces," *Wear*, vol. 268, no. 1, pp. 335-345, 2010 .
- [60] A. Le Bot and E. Bou Chakra, "Measurement of friction noise versus contact area of rough surfaces weakly loaded," *Tribology letters*, vol. 37, no. 2, pp. 273-281, 2010.
- [61] M. Othman, A. Elkholy and A. Seireg, "Experimental investigation of frictional noise and surface-roughness characteristics," *Experimental Mechanics*, vol. 30, no. 4, pp. 328-331, 1990 .
- [62] M. Renouf, F. Massi, N. Fillot and A. Saulot, "Numerical tribology of a dry contact," *Tribology International*, vol. 4, no. 7-8, pp. 834-844, 2011.
- [63] B. Bhushan, "Contact mechanics of rough surfaces in tribology: Single asperity contact," *Appl Mech Rev*, vol. 49, no. 5, 1996.
- [64] J. Archard, "Contact and Rubbing of Flat surfaces," *Journal of Applied Physics* , vol. 24, no. 981, 1953.
- [65] S. Timoshenko and J. Goodier, *Theory of elasticity*, New York: McGraw-Hill, 1951.
- [66] G. Adams and M. Nosonovsky, "Contact modeling-forces," *Tribology International* , vol. 33, p. 431-442, 2000.

- [67] D. Whitehouse and J. Archard, "The properties of random surfaces of significance in their contact.," *Proc Royal Soc London Ser A*, vol. 316, p. 97–121, 1970.
- [68] R. Onions and J. Archard, "The contact of surfaces having a random structure," *J Phys D Appl Phys*, vol. 6, p. 289–304, 1973.
- [69] R. Nayak, "Random process model of rough surfaces," *ASME J Lubrication Tech*, vol. 93, p. 398–407, 1971.
- [70] A. Majumdar and C. Tien, "Fractal characterization and simulation of rough surfaces," *Wear*, 1990.
- [71] B. Mandelbrot, *Fractals: form, chance and dimension*, San Francisco: Freeman, 1977.
- [72] M. Berry and Z. Lewis, "On the Weierstrass-Mandelbrot fractal function," *Proc. R.Soc.Lond.*, vol. 370, pp. 459–484, 1980.
- [73] M. Godet, "The third body approach: A mechanical view of wear," *Wear*, vol. 100, pp. 437–452, 1984.
- [74] D. Dowson, C. Taylor, T. Childs, G. Dalmaz, Y. Berthier, L. Flamand, J. Georges and A. Lubrecht, *The third body concept: interpretation of tribological phenomena*, Elsevier Science, 1996.
- [75] H. Ben Abdelounis, H. Zahouani, A. Le Bot, J. Perret-Liaudet and M. Tkaya, "Numerical simulation of friction noise," *Wear*, vol. 271, pp. 621–624, 2011.
- [76] M. Bengisu and A. Akay, "Stick-slip oscillations: Dynamics of friction and surface roughness," *The Journal of the Acoustical Society of America*, vol. 105, pp. 194–205, 1999.
- [77] J. Slavic, M. Bryant and M. Boltezar, "A new approach to roughness-induced vibrations on a slider," *Journal of Sound and Vibration*, vol. 306, pp. 732–750, 2007.
- [78] A. Yastrebov V., J. Durand, H. Proudhon and G. Cailletaud, "Rough surface contact analysis by means of the Finite Element Method and of a new reduced model," *C.R.Mecanique*, vol. 339, pp. 473–490, 2011.
- [79] V. Dang, J. Perret-Liaudet, J. Scheibert and A. Le Bot, "Direct numerical simulation of the dynamics of sliding rough surfaces," *Comput Mech*, vol. 52, pp. 1169–1183, 2013.
- [80] Y. Karpenko and A. Akay, "A numerical model of friction between rough surfaces," *Tribology International*, vol. 34, pp. 531–545, 2001.

- [81] E. Berger, “Friction modeling for dynamic system simulation,” *Applied Mechanics Reviews*, vol. 55, pp. 535-577, 2002.
- [82] K. Willner, “Surface models for contact laws,” International Conference on Computational Methods in Contact Mechanics, pp. 3-10, 2001.
- [83] O. Lundberg, S. Finnveden, S. Björklund, M. Pärssinen and I. Lopez Arteaga, “A nonlinear state-dependent model for vibrations excited by roughness in rolling contacts,” *Journal of Sound and Vibration*, vol. 345 , pp. 197-213, 2015.
- [84] U. Sellgren and U. Olofsson, “Application of a constitutive model for micro-slip in finite element analysis,” *Computer Methods in Applied Mechanics and Engineering*, vol. 170, no. 1-2, pp. 65-77, 1999 .
- [85] BS EN ISO, “Geometrical product specification (GPS). Surface texture. Profile method. Terms, definitions and surface texture parameters,” p. 4287:2000.
- [86] A. P. Cabboi and J. Woodhouse, “The frequency response of dynamic friction: Enhanced rate-and-state models,” *J. Mech. Phys. Solids*, vol. 92, p. 210–236, 2016.
- [87] S. Wang and J. Woodhouse, “The frequency response of dynamic friction: A new view of sliding interfaces,” *Journal of the Mechanics and Physics of Solids*, pp. 1020-1036, May 2011.
- [88] B. Bhushan, “Contact mechanics of rough surfaces in tribology: multiple asperity contact,” *Tribology letters*, vol. 4, pp. 1-35, 1998.
- [89] E. Rabinowicz, *Friction and wear of materials*, New York: Wiley, 1965.
- [90] R. Fagiani, F. Massi, E. Chatelet, Y. Berthier and A. Akay, “Tactile perception by friction induced vibrations,” *Tribology International*, vol. 44, no. 10, pp. 1100-1110, 2011.
- [91] R. Fagiani, F. Massi, E. Chatelet and Y. Berthier, “Design and validation of an experimental set-up for the analysis of friction induced vibrations at the finger contact surface,” *XX Congresso dell’Associazione Italiana di Meccanica Teorica e Applicata*, 2011.
- [92] N. Lobontiu, *Compliant mechanisms design of flexure hinges.*, CRC Press, 2002.
- [93] L. Baillet and T. Sassi, “Simulations numériques de différentes méthodes d’éléments finis pour les problèmes de contact avec frottement,” *Comptes Rendus - Mec.*, vol. 331, no. 11, p. 789–796, 2003.

- [94] L. Baillet and T. Sassi, "Finite element method with Lagrange multipliers for contact problems with friction," *Comptes Rendus Mathématique*, vol. 334, pp. 917-922, 2002.
- [95] Meziane, A., L. Baillet and B. Laulagnet, "Experimental and numerical investigation of friction-induced vibration of a beam-on-beam in contact with friction," *Applied Acoustics*, vol. 71, pp. 843-853, 2010.
- [96] Ansys, *Ansys Mechanical Structural Nonlinearities: Introduction to Contact*, Ansys Inc., Place Ansys Inc. , 2010.
- [97] P. Wriggers, *Computational Contact Mechanics*, New York: Springer Berlin Heidelberg , 2006.
- [98] N.J. Carpenter, "Lagrange constraints for transient finite element surface contact," *International Journal of Numerical Methods of Engineering*, *Place International*, pp. 103-128, 1991.
- [99] L. Baillet and T. Sassi, "Mixed finite element formulation in large deformation frictional contact problem," *Revue Européenne des Eléments Finis*, *Place Revue Européenne des Eléments*, vol. 2005, pp. 287-304.
- [100] M. D. Bartolomeo, G. Lacerra, L. Baillet, E. Chatelet and F. Massi, "Parametrical experimental and numerical analysis on friction-induced vibrations by a simple frictional system," *Tribology International*, pp. 47-57, 2017.
- [101] I. s. 6344, Coated abrasives -- Grain size analysis, 1998.
- [102] S. Milana, F. A. and C. A., "Observation DOF's Optimization for Structural Forces Identification," *Model Validation and Uncertainty Quantification*, vol. 3, pp. 27-34, 2015.
- [103] C. Pézerat and J.-L. Guyader, "Force analysis technique: reconstruction of force distribution on plates.," *Acta Acustica United Acustica* , vol. 86, no. 2, p. 322–332, 2000.
- [104] A. Fregolent and A. Sestieri, "Force identification from vibration measurements in the wavenumber domain," *Proc ISMA* , vol. 21, p. 517–526, 1996.
- [105] E. S. Ventsel, *Teoria delle probabilità (Teorija verojatnostej)*, Mosca: Edizioni Mir, 1983.
- [106] G. Lacerra, F. Massi, E. Chatelet and E. Moulin, "Acoustic Energy Transfer by Friction Induced Vibrations," in *X International Conference on Structural Dynamics, EUROLYN 2017*, Rome, 2017.



FOLIO ADMINISTRATIF
THESE DE L'UNIVERSITE DE LYON OPEREE AU SEIN DE L'INSA LYON

NOM : Lacerra **PRÉNOM** : Giovanna

DATE de SOUTENANCE : 18/12/2017

TITRE : Friction Induced Vibrations as a result of system response and contact dynamic: a newer friction law for broadband contact excitation

NATURE : Doctorat Numéro d'ordre : 2017LYSEI118

Ecole doctorale : MEGA

Spécialité: Génie Mécanique

ABSTRACT:

Friction-Induced Vibrations (FIV) are a complex phenomenon which arises each time two surfaces undergo relative sliding. During the last decades, a significant amount of experimental and numerical works dealt with Friction-Induced Vibrations, while the simulation of the dynamic excitation from frictional contacts has always been a real challenge to face in many industrial research areas. In this research framework, this work is addressed to the investigation of the Friction-Induced Vibrations, carrying on at the same time experimental and numerical analyses; a new numerical approach is proposed to reproduce the local dynamic excitation from the contact and its effect on the vibrational response of the system, without significant increase of the computational time costs.

The mechanical system, object of the investigation, is composed by two steel beams in frictional contact during relative motion; the simple dynamics of the system allows for distinguishing between the dynamics response of the system and the broadband excitation coming from the contact.

A parametrical experimental campaign has been conducted to analyse the effects of three main contact parameters (the relative sliding velocity, the normal load and the surface roughness) on the system vibrational response, e.i. on the induced vibrations. In parallel, a numerical model has been implemented to reproduce the local dynamic excitation from the contact and its effect on the vibrational response of the system. A new friction law has been introduced in the model, proposing the use of a perturbative term in the friction coefficient in order to simulate the effects of the contact excitation. The inclusions of the local dynamic excitation, due to the contact phenomena, by the perturbation term of the friction coefficient allows to correctly reproduce the Friction-Induced Vibrations without introducing a representation of the real surface topography, which usually needs a large number of elements, saving then computational time. Different signals for the perturbative term have been tested to simulate correctly the measured vibrations. The evolution of the perturbative term recovered by an inverse method allowed for highlighting the different spectral contributions of the local excitation coming from the contact.

The comparison between the measured Friction-Induced Vibrations and the ones simulated numerically showed good correlation, validating the proposed friction law. Finally, the effect in a change of the sliding velocity and surface roughness have been simulated numerically too and correlated with experimental results.

MOTS-CLÉS : Friction-Induced Vibrations, dry friction, friction law, contact dynamics

Laboratoire (s) de recherche : Laboratoire de Mécanique de Contact et des Structures (LaMCoS) UMR CNRS 5259-
INSA de Lyon

Dipartimento di Ingegneria Meccanica e Aerospaziale (DIMA)
La Sapienza-Università di Roma

Directeurs de thèse: Francesco MASSI, Professor, Università di Roma La Sapienza
Aurélien SAULOT, Maître de Conférence, HdR, Insa de Lyon

Co-directeur de thèse: Eric CHATELET, Maître de Conférences, Insa de Lyon
Président de jury : Annalisa FREGOLENT

Composition du jury :

Reviewer	N. HOFFMANN	Professor	Hamburg University of Technology
Reviewer	I.M. KOC	Professor	Istanbul Technical University
Examiner	A. FREGOLENT	Professor	Università di Roma "La Sapienza"
Examiner	L. BAILLET	Professor	Université Grenoble Alpes-IsTerre
Examiner	A. MEZIANE	Maître de Conférences	Université Bordeaux 1
Co-director	F. MASSI	Professor	Università di Roma "La Sapienza"
Co-director	E. CHATELET	Maître de Conférences	Insa de Lyon
Co-director	A. SAULOT	Maître de Conférences, HdR	Insa de Lyon